Dissertation

submitted to the
Combined Faculties of the Natural Sciences and Mathematics
of the Ruperto-Carola-University of Heidelberg, Germany
for the degree of
Doctor of Natural Sciences

presented by
Dipl.-Phys. Julia Stützel
born in Filderstadt
Oral examination: January 19$^{\text{th}}$, 2011

Fragmentation of Small Multi-Electron Molecular Ions in Cold Electron Collisions

Referees:

Prof. Dr. Andreas Wolf

Prof. Dr. Selim Jochim

Kurzfassung

Fragmentation kleiner Mehrelektronen-Molekülionen in kalten Elektronenstößen

Der Aufbruch der kleinen Mehrelektronen-Molekülionen HF^+, DF^+ und D_3O^+ in dissoziativen Rekombinations(DR)-Prozessen mit kalten Elektronen wurde untersucht. Am Ionen-Speicherring TSR, Heidelberg, wurden die jeweiligen Ionenstrahlen mit einem kalten Elektronenstrahl hoher Intensität überlagert und die relativen Impulse der Aufbruchsfragmente mithilfe zweier bildgebender Detektoren gemessen. Zum ersten mal konnte ein rotation-und feinstrukturaufgelöstes Spektrum der im DR Prozeß freigesetzten kinetischen Energie gemessen werden. Die besondere Struktur von HF^+ in Kombination mit der bestmöglichen Kontrolle der experimentellen Bedingungen ermöglichte die Bestimmung der Dissoziationsenergien von HF^+ und DF^+ mit einer Präzision, die ausreichend ist, um den Zusammenbruch der Born-Oppenheimer Näherung in den elektronischen Grundzuständen der zwei Isotope beoachten zu können. Aus der gemessenen Verteilung der in den unterschiedlichen Zerfallskanälen des D_3O^+ freigesetzten Energie konnten Hinweise über die Anregungszustände sowohl des Edukts als auch der Produkte gewonnen werden. Für die Ereignisse mit großer freigesetzer Energie wurde desweiteren im Dreikörperkanal $OD + D + D$ eine deutlich asymmetrische Energieverteilung zwischen den Deuteriumfragmenten beobachtet. Dies weist auf einen sequentiellen Zerfall über den Zwischenzustand eines angeregten Wassermoleküls hin. Mithilfe von ab-inito berechneten adiabatischen Potentialflächen konnte ein Mechanismus vorgestellt werden, welcher den Aufbruch in die beiden Kanäle beschreibt.

Abstract

Fragmentation of small multi-electron molecular ions in cold electron collisions

The fragmentation of the small multi-electron molecular ions HF^+, DF^+ and D_3O^+ was investigated in slow electron collisions leading to dissociative recombination. Momentum spectroscopy of the collision products from stored beams of each ion species merged with an intense cold electron beam has been performed at the ion-storage ring TSR, Heidelberg, utilizing two different imaging detectors. For the first time, a rotationally and fine-structure resolved kinetic energy release spectrum of the DR process was measured. The unique structure of HF^+ combined with an optimal control of the experimental parameters allowed to derive the dissociation energies of HF^+ and DF^+ with a precision sufficient to investigate the Born-Oppenheimer breakdown in the electronic ground states of the two isotopes. The measured kinetic energy release distribution for the different dissociation channels in the D_3O^+ DR yields information on the internal states of educt and products. In addition, a strongly asymmetric energy partitioning among the deuterium products of the three-body channel $OD + D + D$ is observed for high kinetic energy releases, indicating a sequential decay via an excited water molecule. Including ab-initio calculated adiabatic potential energy surfaces, a mechanism describing the interrelated dissociation into $D_2O + D$ and $OD + D + D$ is proposed.

Contents

Abbreviations and Symbols

α_e	angle between any pair of bonds at equilibrium
α_t	magnetic expansion
$\Delta\Phi$	difference in workfunction between the GaAs photocathode and the chamber walls
$\hat{\mu}_{fi}$	transition dipole moment from state i into state f
$\hat{a}, \hat{a}^+$	creation and annihilation operators
$\hat{J}$	angular momentum operator
Λ	effective component of the electronic angular momentum $\vec{L}$
$\mathcal{H}$	hamiltonian
μ	reduced mass
Ω_i	calibrated ratio of the intensities measured by the cameras C_2, C_1
Ω_s	Ω of single events
ω_{fi}	transition frequency from state i into state f
ρ_e	electron density
Σ	effective component of the total spin $\vec{S}$
$\sigma_{blurred}$	position center spread of spots on the phosphor screen
τ	phosphor screen decay constant
τ_i	lifetime of a state i
$\tilde{\Omega}$	non-calibrated Ω
φ, ψ, θ	Euler angles
$\vec{r}_i = \begin{pmatrix} x_i \\ y_i \end{pmatrix}$	coordinates of fragment i on the detector surface
$\vec{S}$	total spin
A	spin-orbit coupling constant
A_{fi}	Einstein coefficient for spontaneous emission from state i into state f

B_ν	rotational constant
B_x, B_y, B_z	rotational constants regarding rotations around symmetry axes' x, y, z
d	real (3D) distance between two fragments
D^0	dissociation energy
D_ν	rotational constant
$D_\perp$	projected distance
$D_\perp^2$	mass-weighted squared projected distance
D_e	classical bond dissociation energy
$d_{\perp,i}^2$	squared projected distance of fragment i from the center of mass
$E_{\mathrm{OD,D,D}}$	energy release in the channel OD + D + D
$E_{\mathrm{OD,D_2}}$	energy release in the channel $\mathrm{OD} + \mathrm{D_2}$
$E_\perp$	transversal kinetic energy
E_B	ion beam energy
E_d	detuning energy
E_E	excitation energy
E_I	ionization energy
$E_{\mathrm{D_2O,D}}$	energy release in the channel $\mathrm{D_2O} + \mathrm{D}$
E_{FS}	energy of fine-structure levels
E_{KER}	kinetic energy release
E_{KER}^0	kinetic energy release in case of ground state reactant and products
i	index of a dissociation fragment
I_1	intensity measured by camera $\mathrm{C_1}$
I_2	intensity measured by camera $\mathrm{C_2}$
I_x, I_y, I_z	moments of inertia regarding symmetry axes' x, y, z
I_{target}	electron current
J_z	z-component of angular momentum $\hat{J}$
L	distance between electron target center and detector
L_t	target length
M	total mass of the molecule
m_e	electron mass
m_i	mass of fragment i
n	principal quantum number
Q_k	normal modes

r_e	equilibrium internuclear distance
T	temperature
t_g	gating time
t_i	arrival time of particle i at the detector
$T_{e,\parallel}$	longitudinal electron temperature
$T_{e,\perp}$	transverse electron temperature
t_{frame}	time at which an event is detected within the camera frame
u_i	velocity of fragment i in the center-of-mass frame of the molecule
U_{target}	acceleration voltage at the target
v	vibrational level
$v^{(n)}$	normal mode, $n \in \#$ modes
v_B	beam velocity
v_d	detuning velocity
v_i	total velocity of fragment i in the laboratory frame
$v_{e,\parallel}$	longitudinal electron velocity
$v_{e,\perp}$	transverse electron velocity
v_{rel}	relative velocity
Y	A/B_ν
AI	autoionization
BAMBI	Beamline for Advanced Molecular Breakup Investigations
cm	center of mass
DE	dissociative excitation
DI	dissociative ionization
DR	dissociative recombination
EMU	Energy-sensitive MUlti-strip detector
HSI	Hoch-Strom Injektor
IPF	ion-pair formation
ISM	interstellar medium
IVR	intramolecular vibrational redistribution
k(x,y)	intensity calibration map
KER	kinetic energy release
MCP	micro channel plate
PES	potential energy surface
rf	radiofrequency

RIP	resonant ion-pair formation
TSR	Test Storage Ring
u	atomic mass units

Chapter 1

Introduction

A significant fraction of the matter in the universe exists as plasma [Boy03]. In fact, the Earth and its lower atmosphere are an exception, forming a plasma-free region in a plasma-dominated universe. On earth, plasmas play an important role only in artificial environments such as combustion engines and fusion reactors, where they are created at high temperatures. The upper layers of planetary atmospheres, in contrast, can be described as naturally occurring plasmas, since at high altitudes the gas is continuously exposed to ionizing stellar and cosmic radiation. Plasmas are also found in the interstellar medium [McC98], which is continuously enriched in new elements by supernovae and in which new stars can form by gravitational collapse. These dense, interstellar clouds have been found to have temperatures between 10 and 50 K and to contain a rich spectrum of molecular ions [Her05]. Here, in these cold and dilute environments, an important process driving chemical reactions in the medium is dissociative recombination (DR) [Lar08, Tho08, FM06]. This mechanism involves the collision of low energy electrons (ranging from a few meV to a few eV) with positively charged molecular ions, leading to the formation of neutral fragments. The reaction is very efficient at low collision energies. In fact, it is the dominant neutralization process in many types of plasmas. In addition, DR is a strongly exothermic reaction with typical energy releases of a few eV, leading to the production of radicals, which facilitate further chemical reactions in cold environments.

Laboratory studies of the dissociative recombination process provide input parameters for modeling such atmospherical and astrophysical environments. Reaction rate measurements allow the prediction of the interstellar medium chemical compo-

sition and the deduction of plasma parameters from spectroscopic data. Moreover, experimental investigation of the reaction dynamics provide benchmarks for theoretical models of molecular potential landscapes. In addition, it allows the deduction of fundamental properties of the ions themselves.

For the simplest diatomic ions like H_2^+ or HD^+, DR has been studied intensively in ion storage ring experiments over the last two decades [Ami98, Nov08b, Zaj03a], and meanwhile the respective theoretical calculations reproduce the experimental data fairly well. In species with many additional electrons and/or nuclei, however, accurate modeling of the recombination process becomes more difficult due to many-body effects.

This thesis aims at improving the understanding of the DR in more complex systems via precision measurements of the fragmentation dynamics of three multi-electron molecular ions: HF^+, DF^+ and D_3O^+. The unique structure of HF^+ combined with optimal control of the experimental parameters makes rotationally and fine-structure resolved momentum spectroscopy of the DR process possible for the first time. Here, the achieved energy resolution appears to even allow the observation of the Born-Oppenheimer breakdown in the electronic ground state of the isotopes HF^+ and DF^+. For D_3O^+, measuring the fragmentation dynamics provides insight into the dissociation mechanism. A particularly important fragment of this electron-induced reaction is the water molecule D_2O. The measurement also yields astrophysically relevant information on the internal-state populations of the molecular dissociation products.

The following chapter provides an overview of fragmentation processes induced by electron-ion collisions, with emphasis on the theoretical background of dissociative recombination. Chapter 3 introduces the experimental instrumentation, the heavy ion storage ring TSR, and the detectors for DR fragment imaging. The concept of a 3D imaging detector and current developments are discussed separately in chapter 4. Chapters 5 presents the details of the HF^+ and DF^+ DR experiments, along with the results obtained from high resolution momentum spectroscopy of the fragmentation processes. A discussion of the D_3O^+ DR measurements, performed with two complementary imaging detectors, follows in chapter 6, together with an interpretation of the data regarding dissociation mechanisms. Chapter 7 finally gives a summary of the results and concludes with an outlook on possible future measurements of systems that have been studied in this thesis.

Chapter 2

Molecular Fragmentation Processes

Molecular structures and dynamics are often considered in terms of potential energy surfaces (PES). The beginning of this chapter deals with an overview of this general concept, followed by a short introduction to electron-molecular cation collisions and the various fragmentation mechanisms of the compound states. Here, the focus is on the process of dissociative recombination (DR), which is the fragmentation process studied in this thesis.

All processes are illustrated for a simple diatomic model, introducing the basic concepts. At the end of the chapter, these ideas are generalized to polyatomic molecules, where usually cuts through the PES are displayed and used for illustration. A complete overview of the theoretical background and activities in dissociative recombination is presented in [Lar08].

2.1 The concept of potential energy surfaces

The structure of a molecular [Dem03] system is commonly described by the Schrödinger equation [Sch26]

$$\mathcal{H}\Psi = E\Psi, \tag{2.1}$$

where the Hamiltonian of the molecule, $\mathcal{H} = \mathcal{T}_N(\vec{R}) + \mathcal{T}_e(\vec{r}) + V_c(\vec{R},\vec{r})$, is a sum of a nuclear kinetic energy operator $\mathcal{T}_N$, the electronic kinetic energy operator $\mathcal{T}_e$ and the potential V_c due to all Coulomb interactions. The sum $\mathcal{T}_e + V_e$ is combined in the 'electronic' Hamiltonian $\mathcal{H}_{ee}(\vec{R},\vec{r}) = \mathcal{T}_e(\vec{r}) + V_c(\vec{R},\vec{r})$, which describes the potential energy of the molecule. Ψ is the total wave function of the molecule and E the total energy.

The considerable mass difference between the electrons and nuclei involved and the corresponding difference in typical velocities of electronic and nuclear motion led to the Born-Oppenheimer approximation in 1927 [Bor27], which proposed the solution of eq. (2.1) to be a product of a nuclear wave function $\chi(\vec{R})$ and an electronic wave function $\phi(\vec{R},\vec{r})$. Via this separation, the electrons are considered to instantaneously follow the relatively slow movement of the nuclei: the eigenfunctions $\phi_n(\vec{R},\vec{r})$ are determined for fixed nuclear arrangements $\vec{R}$ by

$$\mathcal{H}_{el}(\vec{R},\vec{r})\,\phi_n(\vec{R},\vec{r}) = U_n(\vec{R})\,\phi_n(\vec{R},\vec{r}). \tag{2.2}$$

In the Born-Oppenheimer approximation, the electronic eigenenergies $U_n(\vec{R})$ are viewed as potential energy functions governing the motion of the nuclei according to

$$\Big(\mathcal{T}_N(\vec{R}) + U_n(\vec{R})\Big)\,\chi_n(\vec{R}) = E\chi_n(\vec{R}). \tag{2.3}$$

This term describes the effect of the different binding energies of the system at various geometric configurations of the nuclei. Solving eq. (2.2) and eq. (2.3) for every nuclear configuration $\vec{R}$ yields the stationary states of the molecule within the Born-Oppenheimer context: $\Psi_n(\vec{R},\vec{r}) = \chi_n(\vec{R})\,\phi_n(\vec{R},\vec{r})$. The representation of the electronic energies $U_n(\vec{R})$ as functions of the nuclear geometrical arrangement are usually called *potential energy surface* (PES), or, in case of diatomic molecules, *potential energy curves*. In general, the number of atoms bound in the molecule defines the dimensions of the PES.

The PES plays an important role in the description of nuclear dynamics. Finding the minimum of a PES yields the geometrical equilibrium of the molecule. Its vibrational motion is described as oscillations around this minimum. Any reaction of the molecule can be illustrated by a pathway across the PES, along a so-called 'reaction coordinate', which is usually a geometric parameter that changes during the conversion, i.e. a bonding distance or a bonding angle. Last but not least, the fragmentation of a molecular system can also be described by a potential energy function. In this case, the PES is usually repulsive, revealing an energetic minimum at geometries that correspond to infinite separation of the fragments.

There are two steps in considering the terms of the full solution of the problem, which are ignored in the Born-Oppenheimer approximation when completely neglecting any nuclear motion and assuming their masses to be infinite. These terms

are represented by the full nuclear Schrödinger equation

$$\mathcal{T}_N(\vec{R})\chi_n + \sum_m c_{nm}\chi_m(\vec{R}) = (E - U_n(\vec{R}))\chi_n, \tag{2.4}$$

where the coefficients c_{nm}, including different electronic eigenstates n and m, are given in eq. (2.11) in [Dem03]. The *adiabatic approximation* is obtained by retaining only the diagonal contributions $n = m$ in the sum, which includes the small non-Born-Oppenheimer contributions to the binding potentials given by c_{nn}. The potential surfaces are given by slightly different potentials $U'_n(\vec{R})$ including the diagonal non-Born-Oppenheimer correction terms.

For the study of reactive processes, the adiabatic approximation is an appropriate approach only if the PES corresponding to the different electronic states are well separated from each other. If this is not the case, the system can no longer be characterized as proceeding on the potential curve of a single state n. In fact, a process can be considered as a superposition of different states n describing the system during the reaction. In the case of dissociative recombination, which is explained in the next paragraph, the initial system is composed of a molecular ion and a free electron, which can have *any* energy, whereas the final state consists of a set of neutral fragments. Here, it is an appropriate approach to describe the total wave function as a linear combination of Born-Oppenheimer products

$$\Psi(\vec{R}, \vec{r}) = \sum_n \chi_n(\vec{R})\phi_n(\vec{R}, \vec{r}). \tag{2.5}$$

The Schrödinger equation then transforms into a system of coupled equations:

$$\mathcal{T}_N(\vec{R})\chi_n + \sum_{m\neq n} c_{nm}\chi_m = \left(E - U'_n(\vec{R})\right)\chi_n \tag{2.6}$$

with $U'_n(\vec{R})$ being the adiabatic PES. Considering degenerate or near-degenerate energy eigenvalues of the electronic system, these couplings become important and cause shifts of the electronic energy levels and transitions between them as the nuclei move.

For the potentials $U'_n(\vec{R})$ of the adiabatic approximation, curves of the same conserved symmetry quantum numbers cannot cross (at least in the diatomic case) and therefore cannot represent autoionizing resonances, which are considered be-

low. However, different electronic eigenstates $\tilde{\phi}(\vec{R}_f, \vec{r})$ can be chosen, which are obtained at arbitrary fixed nuclear configurations $\vec{R}_f$, typically representing pure orbitals neglecting the configuration interaction. These *diabatic* curves illustrate reaction pathways as shown below.

The PES of polyatomic ions strongly depend on the symmetry of the molecular state, which is defined by the behavior of the electronic wave function under the application of symmetry operations like rotations or reflections that leave the nuclear arrangement unchanged. Considering a planar molecule, a reflection with respect to this plane does not affect the nuclear system. However, the electronic wave function can change or not change its sign due to the reflection and will get back to the original configuration by a second application of the same reflection. Molecules[1] exhibiting this simple reflection symmetry can be classified as symmetric (A') or antisymmetric (A'') with respect to the corresponding symmetry operation.

For states of the same symmetry, the shifts of the electronic energy levels in the adiabatic approximation become manifest in a repulsion between the states in certain regions of energies and internuclear distances. These regions are called *avoided crossings*. The appearance of additional symmetry properties of the nuclear system at certain configurations complicates the picture for polyatomic ions and even adiabatic potentials can cross, forming *conical intersections*. Near such intersections, two electronically degenerate states split up due to a coupling of vibrations and electronic motion, as this drives the system to a slightly different, less symmetric configuration. Such a process is called *Jahn-Teller coupling* [Ber01, Kok03].

2.2 Electron binding as a trigger of fragmentation

In electron–molecular-cation collisions, unstable neutral systems can be formed. Thus, an electron from the molecular ion can be excited. The resulting unstable state is called (electric) resonance and can be depicted by a potential curve in the diabatic representation only. If the potential surface of this resonant state is repulsive, the molecule can dissociate into neutral fragments. The process competes with *autoionization* (AI) where the electron is reemitted.

[1] In chap. 6 this symmetry becomes important for D_3O^+. Even though its ground state is of pyramidal shape (C_{3v} symmetry), only very few vibrational levels exist below the top of the inversion barrier, resulting in a planar (D_{3h}) symmetry that is relevant for the majority of the levels [Luo99].

In another process, the capture of the incident electron can occur through vibrational excitation of the ion into a higher lying, bound vibrational state. This unstable state can stabilize via different processes. Here, the electron can also be re-emitted by AI. This can occur in the exact reverse process of the capture, i.e. both collision partners recover their initial states. In this case, the collision is called *elastic*. *Inelastic* collisions are also possible, in which the electron is emitted with a smaller kinetic energy, leaving behind an ion with higher internal excitation. If the electron is re-emitted with a higher velocity and the vibrational motion of the molecular ion has been perturbed, the collision is called *superelastic*.

However, the electron can also survive autoionization. Then, the electron, which has been captured into an orbit located at a large distance from the nuclei, forming a so-called *Rydberg state*, will easily change the character of the system by mixing to a dissociative state. In the picture of PES, this process involves a transition into another, repulsive electronic state (different PES) of the neutral system. This process is called *predissociation* and can be observed in the energy dependence of the cross section.

Dissociative Pathways

The fragmentation after electron-molecular cation collisions is generally not unique. The dissociation can lead to the formation of charged fragments as well as to different sets of neutral fragments with different states of excitation. A short overview of the various dissociation mechanisms by means of a general diatomic cation AB^+ is described in the following section.

Dissociative excitation (DE). The kinetic energy of the incident electron is sufficient for the molecular ion AB^+ to reach its vibrational continuum, which permits the system to dissociate via dissociative excitation (DE), in which one of the fragments is ionic:

$$\begin{array}{ccc} AB^+ + e^- & \longrightarrow & \begin{cases} A^+ + B + e^- \\ A + B^+ + e^- \end{cases} \\ & \searrow \quad \nearrow & \\ & AB^* & \end{array} \quad . \tag{2.7}$$

DE can occur directly or via an intermediate state. The distribution of charge between the fragments depends on the internal configuration of AB^*.

Dissociative ionization (DI). In the case of even higher incident electron energies, double ionization of the target ion becomes possible. This leads to the formation of two positively charged fragments:

$$AB^+ + e^- \longrightarrow A^+ + B^+ + 2e^-. \tag{2.8}$$

Both, DE and DI, involve the formation of resonances and their subsequent autoionization, mentioned earlier in this section.

Ion-pair formation (IPF). For low interaction energies, some ionic channels with a total charge of zero, corresponding to a neutral intermediate state, exist, leading to pairs of positive and negative fragments:

$$AB^+ + e^- \longleftrightarrow AB^* \longrightarrow \begin{cases} A^+ + B^- \\ A^- + B^+ \end{cases}. \tag{2.9}$$

This process is also often referred to as *resonant ion-pair formation* (RIP), even though it does not necessarily need to be resonant.

Dissociative recombination (DR). The reaction which results in the formation of exclusively neutral products is called dissociative recombination (DR). It is an exothermic process, in which the excess internal energy is converted into kinetic energy for the nuclei, such that the compound state dissociates into neutral fragments. The process can proceed via different intermediate states, which are described in more detail in the upcoming section.

2.3 Dissociative recombination

In dissociative recombination, as introduced in the previous section, the electron is captured into a temporarily neutral state, which can be either a doubly electrically excited resonant state AB^{**} or a singly excited Rydberg state A^* with additional

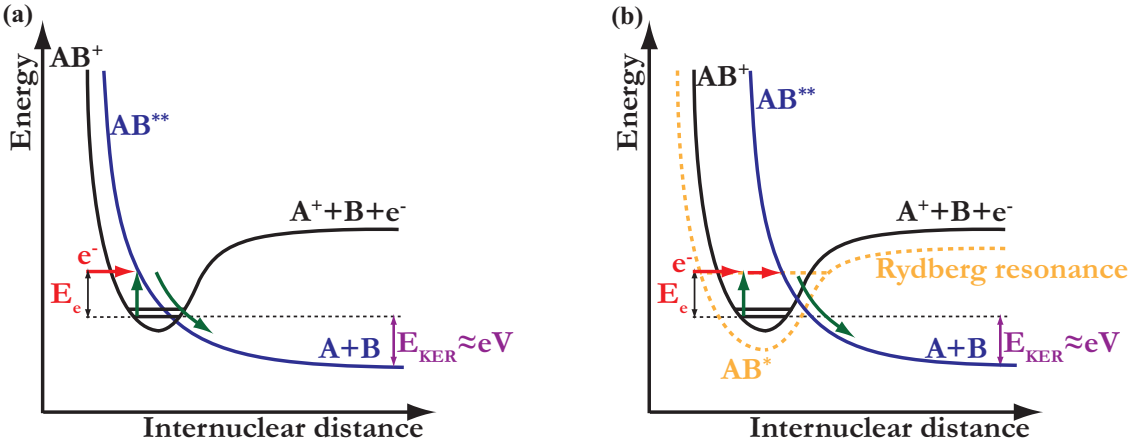

Figure 2.1 Sketch of potential curves for the (a) direct and (b) indirect mechanism of dissociative recombination. The potential curves are defined in the diabatic picture, where they are allowed to cross and resonant states above the ionic potential curve can be visualized.

vibrational excitation:

$$\begin{array}{ccccc} \mathrm{AB}^+ + e^- & \longrightarrow & \mathrm{AB}^{**} & \longrightarrow & \mathrm{A} + \mathrm{B} \\ \searrow & & \nearrow & & \\ & \mathrm{AB}^* & & & \end{array} \tag{2.10}$$

Depending on which of these two states is formed, the process is referred to as being *direct* or *indirect*.

Direct mechanism. First proposed in 1950 [Bat50], the direct mechanism depends on a favorable crossing of the ionic ground state by a neutral repulsive state at low energies. Such a state is shown schematically for the diatomic molecule AB^+ in fig. 2.1 (a). An electron with a kinetic energy E_e is captured by the ion into a valence state of the neutral, thereby exciting one of its valence electrons. The doubly excited neutral state AB^{**} is repulsive along the bonding coordinate, implying a bond stretch towards dissociation. Directly after the capture, the potential energy of the molecule is sufficient to autoionize. However, as the dissociation proceeds along the repulsive potential, it crosses the ion curve and becomes stable with respect to autoionization. The energy difference between the dissociative state and the initial ionic state plus any possible kinetic energy of the electron is released in

terms of kinetic energy of the fragments, which is usually in the range of a few eV. The direct mechanism has no resonant character, since it occurs as a vertical electronic transition at various electron collision energies in a range corresponding to the Franck-Condon region of the ionic vibrational level. Here, the reaction rate varies smoothly with the internuclear distance and the incident energy of the electron.

The existence of a repulsive potential crossing the ground state of the ion is an essential requirement for the direct DR process to occur. For different ions like e. g. H_3^+ this is not the case. Therefore, the DR rate coefficient, which is usually in the order of $\alpha_{rc} \sim 10^{-7}\,\mathrm{cm^3\,s^{-1}}$, was predicted to be much lower for electron energies $E_e \approx 0$. This, however is in disagreement with the experimental findings. Another mechanism was suggested in 1968 [Bar68] to be a competing process – the *indirect* process.

Indirect mechanism. In the indirect DR process, the simple picture of two PES is complicated by Rydberg states of the neutral molecule, converging to the ground state of the molecular ion. The collision is followed by a capture of the electron into a vibrationally excited Rydberg state AB^*, as it is illustrated in fig. 2.1 (b). In contrast to the direct mechanism, in which the incident electron only interacts with the bound electrons in the molecule, the electron here directly excites the molecular ion core vibrationally. Afterwards, the Rydberg state is *predissociated* by the doubly excited repulsive state AB^{**}, then proceeds in the same manner as the direct mechanism (eq. (2.10)). Again, this state can autoionize before it crosses the ionic curve, possibly yielding a molecular ion in a different vibrational state than its initial one. In this reaction, the energy of the incoming electron needs to match the energy necessary to be captured into the Rydberg state, as these are bound states with discrete energies. Therefore, the indirect process is always resonant, leading to resonances in the total cross section as both mechanisms interfere with each other.

It is worth noting that this picture is misleading for polyatomic ions, as they possess several bonding coordinates. Here, the process occurs on a multidimensional surface as it is highly likely for the PES corresponding to the different dissociation channels to cross the ionic potential at different coordinates. The DR process becomes much more complicated by these different dissociation channels since they lead to multiple combinations of molecular and atomic products, which can be internally excited by different degrees.

Overall, the DR process of a molecule M can be described by generalizing eq. (2.10) to

$$\begin{array}{ccccc} \mathrm{M}^+(n,v,J) + e^-(E_e) & \longrightarrow & \mathrm{M}^{**} & \longrightarrow \sum_i p_i^{(*)} + \sum_i E_{KER,i} \\ & \searrow & \nearrow & & \\ & & \mathrm{M}^* & & \end{array} \quad . \tag{2.11}$$

Here, a molecule M with internal energy (n, v, J) dissociates into particles p, which can be either atomic or molecular fragments with possible internal excitation. Experimental measurements of the kinetic energy partitioning between the individual fragments including their identification sheds light into the DR process. The branching ratios into different final fragment states and species can yield information on the fragmentation pathways, which will be shown in the case of D_3O^+ in chap. 6. In addition, the knowledge of the kinetic energy release (KER) in combination with some well known properties of the final products infers the internal excitation of the fragments, but can also yield information on the initial molecular ion state. Therefore, even fundamental quantities like the dissociation energy D^0 of the parent ion can be obtained, as will be demonstrated with HF^+ in chap. 5. Even though not treated in this thesis, another important parameter of interest is the DR rate coefficient, which is related to the reaction cross section.

Chapter 3

Fast Beam Fragment Imaging

Studies of the dynamics in molecular fragmentation processes require good control of both the reactants and the products. Electron-cooler ion-storage rings in combination with effective 4π neutral fragment detection provide the environment needed for the preparation of high quality molecular ion beams and enable high-resolution electron collision studies at low relative energy.

This chapter gives an introduction to the general concept of merged-beam storage ring experiments. Following an overview of how these ideas have been realized at the *Test Storage Ring (TSR)*, the detection systems for neutral imaging installed at the TSR are presented. Finally, the reconstruction of molecular fragmentation dynamics from fragment imaging data is explained.

3.1 Storage ring experiments

Originally developed for the needs in particle and nuclear physics, storage rings have later been established as a tool to study atomic physics with highly charged ions [Bra98, Mül98, Wol00]. The design criteria imposed by the difficulties in handling highly charged ions have also made ion-storage rings a useful tool in the research of molecular fragmentation processes [Lar97]. The characteristics of ion-storage rings are presented in this chapter.

3.1.1 The ion-storage ring technique

An ion-storage ring is a device in which a beam of ions, produced in an ion source and accelerated to typical energies ranging from a few keV up to several MeV per

nucleon, is stored by means of magnetic fields on a closed orbit. These high energies are of great advantage to the detection systems of molecular fragments. As the kinetic energy released in a dissociation is small compared to the ion beam energy, the flight paths of neutral fragments create a narrow cone in the forward direction. Thus, a small detector downstream of the interaction region is sufficient for effective $4\,\pi$ neutral fragment detection. Further, in combination with an intense, co-moving beam of electrons with a precisely defined velocity which is merged with the ion beam, the spatial and energetic spread of individual ion trajectories is reduced. Due to the kinematic transformation involved in describing the dynamics of such electron coolers, and thanks to the high velocities of both the ions and electrons, merged-beam setups allow for collision energies with meV precision.

The ability of storing the ions establishes further possibilities. Experiments with a low rate coefficient benefit from an increased reaction rate, enabled by 'recycling' the ions as they pass the interaction area typically more than a hundred thousand times per second. In addition, the ambient ultra high vacuum of the storage ring allows molecular beams to be stored for tens of seconds due to the reduced number of destructive residual gas collisions. The probability of such collisions is even further diminished by the high ion beam velocity as these reactions show a much smaller cross section at high collision energies. The resulting long storage lifetimes allow the molecules to internally relax. Standard ion sources usually produce vibrationally excited ions. In the case of infrared active molecules, the storage lifetimes exceed typical vibrational relaxation lifetimes by several orders of magnitude [Zaj03a], resulting in an ion beam thermalized to its surrounding equilibrium temperature of approximately 300 K.

In addition, the ions can be manipulated actively. As mentioned above, the ion beam is merged with a beam of continuously regenerated, velocity-matched electrons, i.e. $v_e = v_B$. Therefore, electron energy $E_e = \frac{m_e}{2} v_e^2$ and ion beam energy $E_B = \frac{m_B}{2} v_B^2$ need to fulfill the condition

$$E_e = \frac{m_e}{m_B} E_B. \tag{3.1}$$

The low velocity spread of the electrons produced in the electron cooler induces the process of phase-space cooling, in which the electrons interact by Coulomb forces with the ion beam, rapidly reducing its kinetic energy spread [Beu00]. Within frac-

tions of a second to a few seconds, depending on the ion species, this process results in a dense ion beam with a small diameter and divergence. Besides phase-space cooling and recombination reactions, in which the electron is captured by the ion, non-destructive inelastic electron scattering, so-called super-elastic collisions (SEC), can occur. By absorbing part of the internal energy of the molecular ions, the electrons can actively cool internal excitations. The stored molecules are subsequently in a state of lower vibrational and rotational energy.

In conclusion, the ion-storage ring technique fulfills the requirement of well controlled collision partners. Especially in the case of dissociative recombination, challenges such as neutral fragment imaging, the interest in near-zero collisions energies and low reaction rates or ion currents are well overcome.

3.1.2 The heavy ion storage ring TSR

All experiments presented in this work have been performed using the heavy-ion *Test Storage Ring TSR*, schematically shown in fig. 3.1. It is located at the *Max-Planck-Institut für Kernphysik* in Heidelberg, Germany.

First operated in 1988 [Hab89], the TSR has been used for many experiments studying atomic and molecular physics. Several combinations of ion sources and accelerators are available for producing a wide variety of ions. The Hoch-Strom Injektor (HSI) and a radio-frequency (rf) linear accelerator [Gri93] are limited to a minimum charge-to-mass ratio of 1:9, and are therefore mainly used for the delivery of high currents of light, singly charged molecular ions. Two Van-de-Graaff accelerators are well suited to yield beams of heavier molecular ions. The additional tandem accelerator is designed specifically for the production of highly charged atomic ion beams [Les08]. Both molecules studied in this thesis have been produced by electron impact ionization in a Penning ion source and accelerated using the single-stage Van-de-Graaff accelerator to approximately 2 MeV, before the beam was injected into the TSR using a multiturn injection scheme.

The TSR is a magnetic storage ring with a 55.4 m circumference and a beam pipe diameter of 10 cm. Confined by bending and focusing magnets, ions are stored on a closed orbit in a vacuum of approximately $3 \cdot 10^{-11}$ mbar in order to suppress destructive residual gas collisions. The octagonal shape of the storage ring is realized by four straight sections, that are connected by deflecting sections containing two

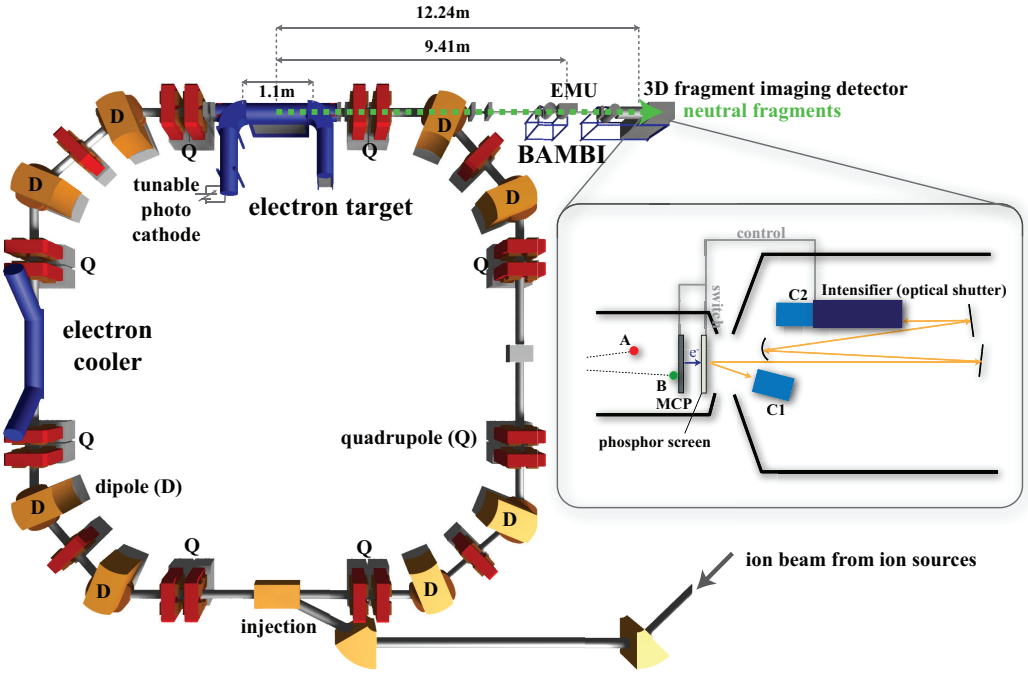

Figure 3.1 Illustration of the storage ring TSR and its experimental Beamline for Advanced Molecular Breakup Investigations, BAMBI. After injection, the ion beam is guided by dipole (D) and quadrupole (Q) magnets inside the ring. Both, the electron cooler and the electron target are merged-beam sections. They are used for phase-space cooling of the ion beam as well as targets in recombination experiments. Downstream of the electron target, neutral recombination products are recorded by two imaging detectors: the recently installed EMU and the multi-hit 3D imaging system.

dipole magnets to guide the ions around the corner. The maximum induction of the dipole magnets B_{max} in combination with the bending radius of the ion beam trajectory ρ define the maximum rigidity $\rho B_{max} \approx 1.5\,\mathrm{Tm}$, which again determines the maximum storage velocity v_{max} for a particular charge-to-mass ratio. Each straight section of the ring is dedicated to a different purpose. While one is reserved for the injection of the ion beam, another is equipped with beam diagnostic tools. The rf resonator installed in this section can, combined with a synchronous increase of the dipole induction, also be used for synchrotron acceleration of the ion beam in the ring.

A unique feature of the TSR, compared to other storage rings, is the installation of two electron beams in the other two straight sections that can be merged simultaneously with the circulating molecular ion beam. By velocity matching the continuously renewed single-pass electrons with the ion beam, the merged beam

sections work as electron coolers. The transversal and longitudinal electron temperatures in the co-moving frame of the beams determine the ions' velocity spread. The electron velocity distribution in the center-of-mass frame of the ions is described by an asymmetric Gaussian distribution [Dan94]

$$f(\vec{v}_e, v_d) = \frac{m_e}{2\pi k_B T_{e,\perp}} \left(\frac{m_e}{2\pi k_B T_{e,\parallel}} \right)^{\frac{1}{2}} e^{\left(-\frac{m_e v_{e,\perp}^2}{2kT_{e,\perp}} - \frac{m_e (v_{e,\parallel} - v_d)^2}{2kT_{e,\parallel}} \right)}, \tag{3.2}$$

with $v_d = v_e - v_B$ being the detuning velocity, i.e. the average velocity of the electrons in the co-moving frame of the ion beam ($\vec{v}_e = (v_{e,\perp}, v_{e,\parallel})$ is the electron velocity, v_B the ion beam velocity, m_e the electron mass and k_B the Boltzmann constant). The kinetic energy defined by the v_d is called detuning energy $E_d = \frac{m_e}{2} v_d^2$.

In addition, the electrons can be used for electron-ion collision experiments, if $v_d \neq 0$. The *electron target* [Spr03], which was named after the fact that its design was optimized for collision experiments with slow ion beams, produces electrons by laser illumination of a liquid nitrogen-cooled GaAs-photocathode [Orl04, Orl09]. The initial temperature $T_{cath.} \approx 150\,\mathrm{K}$ of the electrons is reduced in the forward direction by slowly accelerating the electrons to the ion beam velocity ($k_B T_{e,\parallel} \sim 0.05\,\mathrm{meV}$ [Kra09]). Adiabatic expansion [Pas96] of the electron beam in a decreasing magnetic field along the flight direction reduces the transversal energy spread to $k_B T_{e,\perp} \sim 1.0\,\mathrm{meV}$ [Kra09]. Depending on the expansion factor α_t, the emitted electron density is in the range of $1...4 \times 10^6\,\mathrm{cm}^{-3}$. In contrast, the *electron cooler* [Ste90] is equipped with a thermionic cathode of $T_{cath.} \approx 1200\,\mathrm{K}$, producing electron beams with energy spreads of $kT_{e,\perp} \approx 10\,\mathrm{meV}$ and $kT_{e,\parallel} \approx 0.15\,\mathrm{meV}$.

The presence of two independent merged-beam devices allows the continuous cooling of the ion beam with the electron cooler, while performing measurements at variable collision velocities with the target section. The accuracy is mainly limited by the electron thermal velocity spread. The present experiments, however, have been performed without operating the electron cooler. The temperature of the cooler's thermionic cathode is too high to provide an efficient cooling within the lifetime of the heavy molecular ions used here [Kra09]. In addition, as the main experiments were performed at near-zero collision energy, the target, operated at $U_{target} = 100...140\,\mathrm{V}$ acceleration voltage and $I_{target} = 300...400\,\mu\mathrm{A}$ electron current, was sufficient to cool the ions and provide well defined collision partners at the same

time.

Several detectors have been installed downstream of the electron target, awaiting the different fragment species originating from the ion-electron collisions. Due to the different charge-to-mass ratios of the charged fragments compared to the parent ions, positive and negative products follow distinct trajectories in the magnetic fields. Detectors for these fragments are located in the first dipole chamber behind the electron target. Positively charged ions are mainly studied in dielectronic recombination measurements of atomic ions [Spr04], while negative ions predominantly emerge from ion-pair formation (IPF). Neutral particles, however, originating mainly from DR processes, are not affected by the magnetic field of the dipole magnets and travel straight along the *Beamline for Advanced Molecular Breakup Investigations* (BAMBI) [Buh06], at the end of which currently four interchangeble detectors can be used for the investigation of the DR process. The beam line can be blocked by a shutter in order to protect the detectors against high particle rates e.g. during injection or synchrotron acceleration. Two energy sensitive surface barrier detectors of different sizes at a distance of approximately 12 m from the electron target center are used for event-by-event counting experiments in DR rate measurements [Buh06]. Two imaging detection systems, yielding mostly complementary information are installed at approximately 9.4 m and at the very end of the beam line. Both neutral imaging detectors are described in more detail in the upcoming section.

3.2 Detectors for neutral fragment imaging

In order to investigate the complete kinematics in molecular fragmentation processes the relative momenta of the reaction products need to be determined. While reaction microscopes are a well established technique in ion-atom collisions resulting in charged products, enabling fully momentum resolved measurements of ionization and charge transfer processes [Ull97, Fis09], information on the momenta of the neutral fragments originating from DR reactions needs to be acquired using a different technique.

As mentioned in section 3.1.2, the BAMBI downstream the reaction region is equipped with a 3D fragment imaging detector. This detector provides access to information on the internal states of both fragments and parent ions as well as on the DR breakup geometries by measuring the relative fragment velocities. These

are determined through the transversal impact distances together with the impact times on the detector with sub-ns-resolution. Lately, a second imaging detector, the ***E**nergy-sensitive **MU**lti-strip detector system* (EMU), was developed and installed at the BAMBI. Its detection principle is based on electron-hole excitation in a depleted semiconductor. The timing information contained in the pulses is not precise enough to measure relative arrival times for individual fragments from a DR event at MeV ion beam energies, but the pulse heights are proportional to the fragment kinetic energies. However, the EMU provides complementary information by identifying the different fragments due to its mass sensitivity and therefore constitutes a powerful tool for distinguishing between chemically different decay channels in case of small polyatomic ions. Further, the high maximum acquisition rate of approximately 2 kHz exhibits an advantage in comparison to the CCD based 3D fragment imaging detector. The following two subsections will give an introduction to both detection systems. The latest developments of the 3D imaging detector are presented in chapter 4.

3.2.1 The 2D multi strip surface barrier detector

The ***E**nergy-sensitive **MU**lti-strip detector system* (EMU) was developed by a collaboration of the the *Max-Planck-Institut für Kernphysik* and the *Weizmann Institute of Science*, Rehovot, Israel, and manufactured by *Micron Semiconductors Ltd.* [Mic] while the electronics was delivered by *Mesytec GmbH* [Mes]. It was installed in May 2008, 9.41 m downstream the electron target center (fig. 3.1). In the following, a short overview of the properties and operational principles of EMU is given. A detailed description can be found in [Buh10a, Men10].

This position-sensitive, double-sided silicon-strip detector covers an area of $10 \times 10\,\mathrm{cm}^2$ (fig. 3.2). It is biased by approximately 70 V. With 128 vertical and 128 horizontal strips on the front and back side of the detector, respectively, individual readout of the pulse height at each strip in principle allows for a measurement of the energy E_i and position (x_i, y_i) of particles hitting the detector. From the measured energy the mass number m_i of the fragment i can be extracted via the approximation

$$m_i = \frac{E_i}{E_B} M, \tag{3.3}$$

where $M = \sum_i m_i$ is the mass of the molecular ion and E_B the ion beam energy.

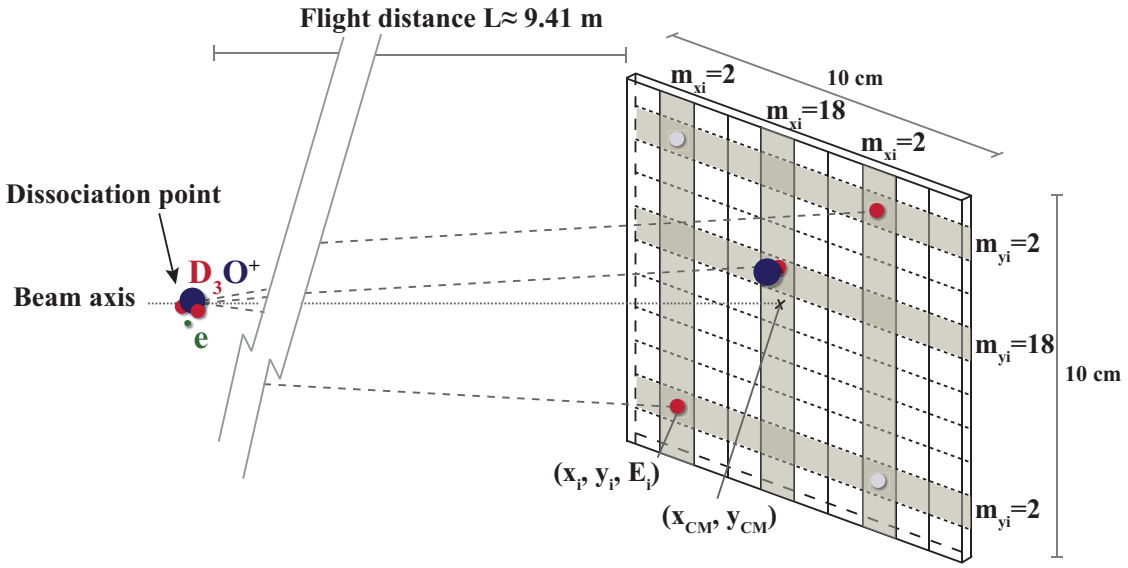

Figure 3.2 Concept of the EMU detector. After recombining with an electron, the neutral molecules dissociate while they continue traveling towards the detector which is installed 9.41 m downstream the center interaction point. As they reach the detector the fragments have acquired macroscopic distances due to the kinetic energy released in the dissociation. The hit pattern is indicated by the shaded strips. Herewith, position (x_i, y_i) and energy E_i of each fragment i is recorded. However, the position of the D atoms (red) is not unique but indistinguishable from the positions indicated by the fragments drawn in light gray. Depending on the hit pattern different ambiguities need to be taken into account during the analysis.

In addition, as the relative arrival time of the fragments is small compared to the gating time of the detector, multiple fragments from a single DR event can be detected within one gate. Since the gating time is much shorter than the typical time between randomly occurring events, single DR events can be recorded separately.

The strips, consisting of a 100 nm thick p^+-doped Si layer covered with a 100 nm thick aluminum coating, are realized by electronically subdividing the front side of the 300 μm thick, fully depleted Si detector basis, into 730 μm wide strips which are separated by gaps of 30 μm. These extremely thin layers, forming the entrance window of 200 nm, reduce the energy loss and its spreading in the dead layer to a minimum. With 700 μm/60 μm the ratio of strip and gap width is slightly different for the back side. The energy of the impinging particles is determined by the read out of each individual strip preserving the pulse height. While strong efforts were made to minimize the thickness of the (Al + Si) entrance window, 50 μm wide edges of each strip are made of thicker layers in order to ensure a clear separation between stripes.

These lead to significantly greater energy losses, displacing the corresponding entries in the pulse height spectrum to lower values, where they appear as 'satellite peaks'. Since these edges cover approximately 14 % of the active area, the effects on mass assignments, especially of heavier masses, where the energy loss can be more than 1/3 of the total energy, is not negligible. A detailed simulation of the system used in the analysis takes this effect into account [Men10].

For data acquisition, *mileDAQ*, a control and data acquisition system developed for TSR experiments, is used [Les07]. The trigger pulse, a threshold defining the minimum pulse height for at least one fragment, starts the data acquisition. Once enabled, the readout of each individual strip is followed by a verification that each pulse height exceeds another threshold value separating real events from background noise. Events passing these conditions are recorded in a raw file, including the timing information relative to the beam injection, as well as voltage and current settings at electron cooler and target.

Data analysis, in general, involves a certain number of steps and is outlined briefly at this point. Mass windows in the pulse height spectrum need to be defined in order to make a mass assignment m_{x_i}, m_{y_i} to each strip of a certain event possible. The sum over all assigned masses needs to match the mass M of the dissociating molecule, separately for front and back side strips. If so, an algorithm going through all combinations yields possible assignments of the measured mass number m_{x_i}, m_{y_i} and the corresponding strip coordinates x_i, y_i. These coordinates, often referred to as the *hit pattern* $\vec{r}_i = \begin{pmatrix} x_i \\ y_i \end{pmatrix}$ of the DR event, provide the coordinates of the center-of-mass (cm) in the detector plane

$$\vec{r}_{cm} = \begin{pmatrix} x_{cm} \\ y_{cm} \end{pmatrix} = \frac{1}{M} \begin{pmatrix} \sum\limits_i m_{x_i} x_i \\ \sum\limits_i m_{y_i} y_i \end{pmatrix}. \tag{3.4}$$

From eq.(3.4), the squared projected *mass-weighted* distances $D_\perp^2$ can be determined from the squared projected fragment distances

$$d_{\perp,i}^2 = (\vec{r}_i - \vec{r}_{cm})^2 \tag{3.5}$$

as

$$D_{\perp}^2 = \sum_i \frac{m_{x_i}}{M} d_{\perp,i}^2 \tag{3.6}$$

which is proportional to the transversal kinetic energy release

$$E_{\perp} = E_B \cdot \frac{D_{\perp}^2}{L^2} \tag{3.7}$$

of the dissociation, where L indicates the flight distance and E_B the ion beam energy.

As indicated in fig. (3.2) – depending on the number and species of atoms forming the molecule – the breakup geometry determined from the hit pattern might not be unique. While the example illustrated in fig. (3.2) only leads to an ambiguity concerning the geometry, in case of multiple fragments hitting the same strip even the identification of the fragmentation channel can be affected. Techniques how to approach these complications are presented in [Men10]. It should be pointed out that both quantities, cm as well as $E_{\perp}$, are not influenced by this ambiguity.

In order to investigate the influence of the slightly different fragment detection efficiencies due to an event geometry, the energy resolution and the finite strip width, which occasionally might lead to a misassignment of a three-body event as a two-body dissociation, a Monte Carlo simulation, similar to the one presented in section 4.4, has been developed. This simulation further allows for a detailed comparison with theoretical predictions for the DR process. Its output is then analyzed with the same tools as the measured data.

3.2.2 The 2D and 3D multi hit fragment imaging detector

At the end of the BAMBI, 12.24 m downstream the electron target center, the *3D fragment imaging detector* is installed (fig. 3.1). It consists of a 78 mm diameter micro channel plate (MCP, Chevron Type, Hamamatsu, Hamamatsu City, Japan) and an adjacent phosphor screen (P 47, blue, (Y_2SiO_5:Ce, Hamamatsu, Hamamatsu City, Japan)). Fragments, impinging on the grounded MCP front plate, create an electron cloud at its backside ($V_{MCP} = 1.9\,\text{kV}...2.0\,\text{kV}$) which is further accelerated to the phosphor screen ($V_{phosphor} = 3.5\,\text{kV}...5.0\,\text{kV}$) where it releases fluorescence light emission. These fast decaying light spots ($\frac{1}{e}$-decay constant $\tau \approx 50\,\text{ns}$), in turn, are recorded by two Charge Coupled Device (CCD) cameras, C_1 and C_2 (640

x 480 pixels each), which face the phosphor screen through a CF100 viewport at the end of the beamline (see fig. 3.1). Both cameras are synchronized via a PC [LaV03] with a sample rate of approximately 30 Hz (10 ms exposure time followed by 20 ms read out time).

Camera C_1 faces the phosphor screen directly and integrates the fragment hit over the entire exponential decay of the fluorescence light. From the relative positions of the particles' light spots, 2D information on the relative fragment distances, i.e. the transverse fragment distances, is obtained. Typically, a good spatial resolution down to the sub-mm range can be achieved. The exact resolution is dependent on the distance of C_1 from the phosphor screen. The minimum distance between particles is predominately limited by the spot size on the camera frame, which is influenced by the C_1 distance from the detector as well as by the potential applied on the phosphor screen. In the experiments presented in this thesis the measured minimum distance between fragments varied between 0.5 mm and 4.0 mm with a resolution of $<100\,\mu$m.

In order to gain 3D information, also the arrival time of the fragments must be measured, which is enabled by the second camera C_2. The principle of the time measurement is illustrated in fig. 3.3. In contrast to C_1, C_2 is equipped with a light intensifier, acting as a fast optical shutter (for which reason camera C_2 will also be referred to as the *gated camera*). The impact of a particle on the detector MCP disables the light intensifier within $t_c = 20$ ns. This closing time t_c is limited by the electronic processing. The light integration of a fragment spot in C_2 is thereby stopped already during the exponential decay of the phosphor, i.e. $t_c < \tau$. Having multiple fragments from one dissociation event arriving at the detector within typically a few ns, the closing of C_2 will be triggered by the first fragment. As a consequence, this results in less integration time for the later fragments and therefore in light spots of lower intensity. By measuring the intensities $I_{2,i}$ (i = fragment index) of all fragment spots in C_2 the difference in arrival time between each two fragments i and j can be obtained via:

$$\Delta t = t_i - t_j = \tau \ln \frac{1 - \Omega_i}{1 - \Omega_j}, \tag{3.8}$$

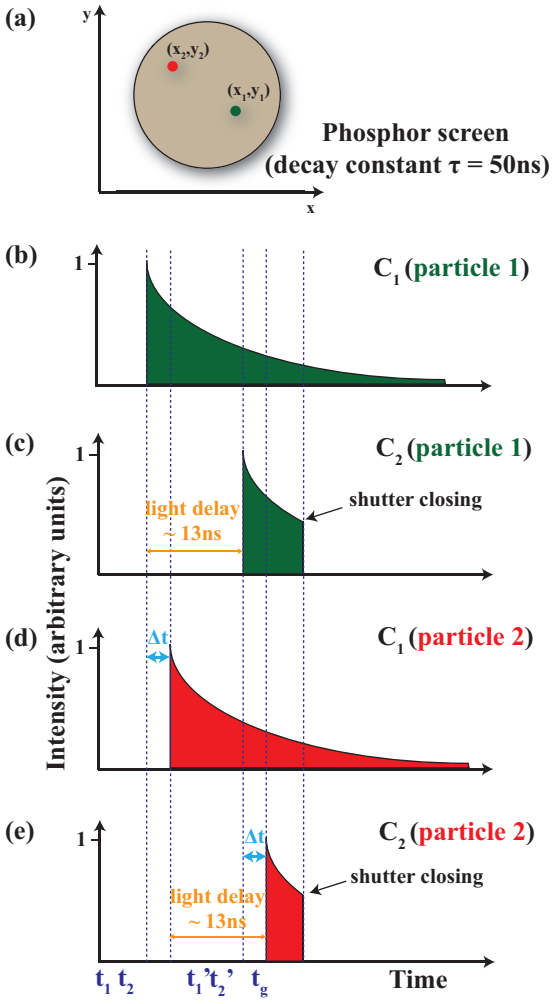

Figure 3.3 3D imaging detector, time measurement principle. (a) Two fragments impinge on the phosphor screen at times t_1 and t_2. (b) Light intensity from the 1st particle integrated over by C_1, $I_{1,1}$. (c) Light intensity from the 1st particle integrated over by C_2, $I_{2,1}$. The optical pathway causes an integration start delayed by 13 ns. Integration is stopped again by the closing of the intensifier at t_c =20 ns after the 1st fragment has hit the phosphor screen. (d) Light intensity from the 2nd particle, arriving later by Δt, integrated over by C_1, $I_{1,2}$. (e) Light intensity from the 2nd fragment integrated over by C_2, $I_{2,2}$. Again, the integration time is shortened by the delayed arrival of the photons as well as by the rapid switch off. The calibrated ratios of the intensities, defined in eq. (3.9), are measured by C_1 and C_2 for each particle $i = 1, 2$ and provide the information about the difference in arrival time between the 1^{st} and 2^{nd} fragment.

where (considering the *gating time* $t_g = t_c$)

$$\Omega_i = \frac{1}{k(x,y)} \frac{I_{2,i}}{I_{1,i}} = \frac{\tilde{\Omega}_i}{k(x,y)} = 1 - e^{-(t_g - t_i)/\tau}. \tag{3.9}$$

$I_{2,i}$ has to be normalized to the corresponding, fully integrated light intensity $I_{1,i}$ recorded in C_1 in order to account for variations in amplification by the MCP. Furthermore, the relative intensity needs to be calibrated by the function $k(x, y)$, where (x, y) defines the spot position within the C_1 frame. This function $k(x, y)$ corrects for the position dependence of the signal (sec. 4.3.2). For a detailed derivation of eq. (3.8), see [Nov05, Men07, Str00].

The indispensable fast shut-off is realized by the image intensifier, which consists of a photo cathode, an MCP and a phosphor screen (P43, 0.9 relative efficiency, green, (Gd_2O_2D:Tb, $\tau_i \approx 0.5$ ms)) arranged sequentially, see [LaV03]. During the

intensifier gating time, a potential of $-180\,\mathrm{V}$ is applied to the photo cathode, accelerating the photo electrons ejected from the impinging photons towards the MCP. The voltage applied between its front and back side is typically 560 eV. The fast shutting of the intensifier is realized by blocking the photo cathode when switching the applied voltage to $+50\,\mathrm{V}$, so that no electrons can escape from the cathode. For reasons of the voltage switching electronics, the duty cycle of the intensifier is limited to a maximum of 50%, depending on the operation mode, with a maximum exposure time of 1 ms. While the switch-on is triggered externally by the PC, the shut-off is either controlled internally, after a maximum exposure time of 1 ms, or triggered externally by the impact of a fragment on the MCP. Within one camera frame this results in $5 \times 1\,\mathrm{ms}$ open shutter periods, separated by $5 \times 1\,\mathrm{ms}$ intervals during which the cathode is blocked – unless an impinging fragment causes an earlier intensifier switch-off. Since the start signal from the PC enables the intensifier regardless of any event occurring it has to be guaranteed that no more than one event will be recorded in the same camera frame. This is ensured by switching off the main phosphor screen, i.e. lowering the voltage to the potential of the MCP, which usually takes 1-2 μs from the moment the first fragment impinges on the MCP. Typical detector rates of a few kHz yield a usual time difference of several 100 μs between two events.

As can be seen from eqs. (3.8) and (3.9), the time difference Δt is logarithmically dependent on the measured intensity ratio Ω_i. Ω_i itself depends on the gating time t_g, which thereby affects the resolution. Thus, any reduction of t_g decreases Ω_i, yielding a better resolution. As metioned above, the gating time t_g cannot be reduced by diminishing the closing time t_c of the intensifier, which is limited to 20 ns by the electronic processing. Instead, the light path of the particle hit is increased for C_2, allowing longer reaction times. This is realized by the following: in contrast to C_1, camera C_2 does not face the phosphor screen directly but records the emitted light only after it has traveled through an optical extension path, causing a time delay of $\Delta t_{delay} \approx 13\,\mathrm{ns}$ [Men07], see fig. 3.1. The heart of the approximately 4 m long pathway is a parabolic mirror (diameter = 203 mm, focal length = 1016 mm), optimizing the image of the phosphor screen on a collective lens in front of the gated camera's objective. In order to account for spatial constraints two flat mirrors make the light path fit into a $180\,\mathrm{cm} \times 80\,\mathrm{cm}$ light-proof box. By this time delay Δt_{delay} the effective closing time t_c is reduced to a gating time, i.e. the effective integration

period of C_2, of $t_g \approx 8\,\text{ns}$ (fig. 3.3, fig. 4.7). Although the reduction of t_g implies an increase in shot noise of C_2, which unlike read out- and dark current noise depends on the number of photons, the time resolution is improved by a factor of 2 from $\delta(\Delta t) \approx 1\,\text{ns}$ at $t_g \approx 20\,\text{ns}$ to $\delta(\Delta t) \approx 0.5\,\text{ns}$ at $t_g \approx 8\,\text{ns}$ (standard deviation, see [Men07]). Further details on the detector principle and setup can be found in [Nov05, Men07].

3.3 Representations of Imaging Data

The neutral fragment imaging detectors presented in the previous section allow for the determination of the relative fragment positions after dissociation. In combination with the ion storage ring technique yielding good control over the reactants, these findings can be used to reconstruct the molecular fragmentation kinematics after dissociative recombination through the determination of the relative momenta of the reaction products [Zaj03b]. So, it provides access to the break-up geometry and to information on the internal excitation of both, fragments and parent ions. The following section illustrates the deduction of the relative fragment velocities for diatomic molecules. Later, the procedure is extended to three-body break-ups.

3.3.1 Imaging of Diatomic Molecules

The principle of the imaging technique in dissociative recombination is outlined in fig. 3.4, using the example of HF^+ recombining with an electron. After electron capture, the molecule, traveling at the beam velocity $\vec{v}_B$, dissociates into the neutral fragments H and F, which are released with kinetic energies of $E_{KER,\text{H}} = \frac{1}{2} m_\text{H} u_\text{H}^2$ and $E_{KER,\text{F}} = \frac{1}{2} m_\text{F} u_\text{F}^2$, respectively. In the co-moving frame of the molecule, the products dissociate back-to-back with velocities $\vec{u}_\text{H}$ and $\vec{u}_\text{F}$, defined by momentum conservation $\sum_{i=\text{H,F}} m_i \vec{u}_i = \vec{0}$. The orientation of the molecular axis before electron capture in combination with the dynamics of the fragmentation process determine the directions of $\vec{u}_i$, which are described by an angle θ relative to the beam axis. Then, the total kinetic energy release can be expressed in terms of the relative velocity $\vec{v}_{rel} = \vec{u}_\text{H} - \vec{u}_\text{F}$ by

$$E_{KER} = E_{KER,\text{H}} + E_{KER,\text{F}} = \frac{1}{2} \mu \, v_{rel}^2, \tag{3.10}$$

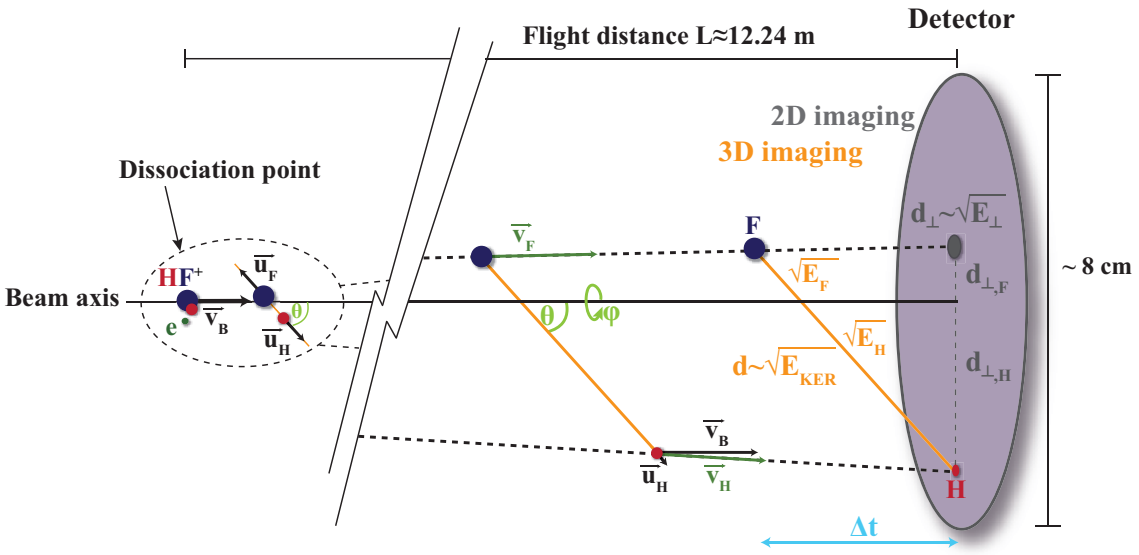

Figure 3.4 Schematic overview of the trajectories of the neutral fragments H and F after dissociative recombination of HF^+ at the distance L from the detector.

with $\mu = \frac{m_H m_F}{m_H + m_F}$ being the reduced mass of the fragment masses m_i.

Thus, in the laboratory frame, the fragments move at total velocities $\vec{v}_i = \vec{v}_B + \vec{u}_i$, with $i \in \{H, F\}$, until they reach the detector at a distance L. At the impact time of the first particle, the time t has passed and the distance d between the fragments has grown to a macroscopic value

$$d = v_{rel} t \approx \frac{v_{rel}}{v_B} L \quad (\text{with } v_i \approx v_B). \tag{3.11}$$

As $E_{KER} \sim v_{rel}^2$, conclusions on the kinetic energy can be drawn by measuring this quantity. This, in turn, is realized by decomposing d into a transverse component $d_\perp$, obtained from the impact positions on the detector, and a component parallel to the beam axis, which is determined by measuring the arrival time difference Δt between the fragments. Considering $L \gg d$, orthogonal projections onto d yield the relations

$$d_\perp = d \sin\theta \tag{3.12}$$

$$\Delta t = d \cos\theta / v_B. \tag{3.13}$$

Typical values are projected distances of some millimeters to a few centimeters and

impact time differences of a few nanoseconds. Then, the kinetic energy release can be determined by

$$E_{KER} = \frac{1}{2}\frac{m_{\mathrm{H}} m_{\mathrm{F}}}{m_{\mathrm{H}} + m_{\mathrm{F}}} \left(\frac{dv_B}{L}\right)^2 = \frac{1}{2}\frac{m_{\mathrm{H}} m_{\mathrm{F}}}{m_{\mathrm{H}} + m_{\mathrm{F}}} \left(\delta \cdot v_B\right)^2, \tag{3.14}$$

with $\delta = d/L = v_{rel}/v_{beam}$ being the maximum fragment emission angle in the laboratory frame [Ami96]. It should be noted, that if particles of different masses are produced in a two-body decay, momentum conservation causes the heavy particles to occur at small distances from the center-of-mass, while the light fragments are detected at large distances with respect to the center-of-mass (in case of HF the distance ratio is determined by $m_{\mathrm{F}}/m_{\mathrm{H}}$).

Transverse distance information

The kinetic energy release can only be calculated from eq. (3.14) if the measurement provides information on the arrival time difference between the fragments. If the measurement yields only information on the transversal impact positions, the kinetic energy release cannot be reconstructed from a single event, as the information on the angle under which the two fragments are ejected in the center-of-mass frame is lost. In fact, by comparing an accumulated distribution of distances $d_\perp$ to a transverse distance probability distribution $P(d_\perp)$ expected for specific fragmentation kinematics, this information can be extracted [Ami96].

However, $P(d_\perp)$ is based on some assumptions. The flight distance L is not exactly known, as the dissociation can take place anywhere within the target. Except for the toroidal region, in which ions and electrons collide at different energies due to the constantly varying collision angles, the probability for a DR event to occur is assumed to be constant over the a reaction zone of length L_t, called the 'effective target length', and zero outside these limits. Further, the angular distribution of the emitted fragments in the co-moving frame of the ions is presumed to be isotropic. Even though anisotropies have been observed at near-zero collision energies [Nov08a], these effects are small, variations in the shape of the distribution-function remaining within a few percent. This makes the assumption of an isotropic breakup reasonable for zero average collision energy, where the incident electron directions are statistically distributed according to the beam temperature.

For a single kinetic energy release $E_{KER} = E_j$, the normalized distribution of the projected distances can be derived analytically [Ami96]

$$P_0(d_\perp, j) = \begin{cases} \frac{1}{\delta_j L_t}\left(\arccos\frac{d_\perp}{\delta_j L_2} - \arccos\frac{d_\perp}{\delta_j L_1}\right) & \text{for } 0 \le d_\perp \le \delta_j L_1 \\ \frac{1}{\delta_j L_t}\arccos\frac{d_\perp}{\delta_j L_2} & \text{for } \delta_j L_1 \le d_\perp \le \delta_j L_2 \\ 0 & \text{otherwise} \end{cases}, \quad (3.15)$$

where L_1 and L_2 are the minimum and maximum flight distances and L_t stands for the effective length of the interaction section. $P_0(d_\perp, j)$ has a well defined shape which is determined by the orientation angles on the low distance side and by the interaction region length L_t and the electron temperature for large distances.

In case of various initial and final states and therefore numerous kinetic energy releases, the expected projected distance distribution is given by the sum of the distributions $P_0(d_\perp, j)$,

$$P_0(d_\perp) = \sum_j b_j P_0(d_\perp, j), \quad (3.16)$$

with b_j being the branching ratio of the j-th dissociation channel. The branching ratios can then be obtained by fitting the sum $P_0(d_\perp)$ to the measured transversal distance distribution. A detailed derivation of eq. (3.15) and an extension towards anisotropic distributions is given in [Ami96, Nov08a].

3.3.2 Imaging of Three-Body Fragmentation

The extension of the above considerations to studies of polyatomic ions is not straightforward. Complications arise from the appearance of additional reaction channels, that need to be identified. Even the mass m_i often cannot be easily assigned to the individual fragments. In addition, the geometric information encoded in the recorded impact positions is multi-dimensional in case of more than two fragments, which complicates the interpretation of these data. In the following, a short overview of how three-body fragmentation data are handled and represented is given. A detailed description can be found in [Lam04].

As in the diatomic case, the total kinetic energy released during a break-up into more than two fragments is given by the sum of the kinetic energies of a each fragment, E_i, i.e. $E_{KER} = \sum_i E_i$ with $E_i = m_i u_i^2/2$. At the detector, according to eq. (3.11), the fragments have reached a distance of $d_i = \frac{u_i}{v_B} L$ with respect to the

center-of-mass, from which the kinetic energy of particle i can be derived via

$$E_{KER,i} = \frac{1}{2} m_i \left(\frac{d_i}{L} v_B \right)^2 . \tag{3.17}$$

Thus, the total KER is given by

$$E_{KER} = \sum_i E_{KER,i} \tag{3.18}$$

Naturally, this is only possible if the detector provides information on the arrival time of the individual fragments. In case of a pure 2D imaging detector, the total transversal kinetic energy release $E_\perp$ is calculated via eq. (3.7) from the squared projected weighted distances $D_\perp^2$ defined in eq. (3.6), provided the masses m_i can be assigned to the fragment hits. The use of the EMU detector or a well defined cm position and subsequent kinematical cuts allow this mass assignment to be performed (sec. 4.2.1).

In the next step, similar to the case of diatomic molecules, an expected distribution like $P_0(d_\perp)$ in eq. (3.16) is needed for comparison to the experiment. Since there is no analytical expression describing the multi-dimensional case, such a distribution is obtained by a Monte-Carlo simulation of the break-up process, as will be described in sec. 4.4. Also here, assumptions need to be made. In particular, the break-ups at $E_d = 0\,\mathrm{eV}$ are expected to be isotropically distributed with no preferred dissociation directions.

Besides the total kinetic energy released, also the break-up geometry of the fragments is of interest. In the following, the method chosen in this thesis to represent dissociation geometries, is outlined.

Dalitz plots

The orientation of the dissociation plane defined by the three fragments is specified by the three Euler angles θ, φ, ψ, which are illustrated in fig. 3.5. In contrast, the geometry of the triangle, spanned by the three velocity vectors u_i of the fragments, can be described by the so-called *Dalitz coordinates*. First introduced in 1953 by R. H. Dalitz [Dal53] in order to analyze the correlations of fragment energies in the three-body decay of K-mesons into π-mesons, the concept has been modified and

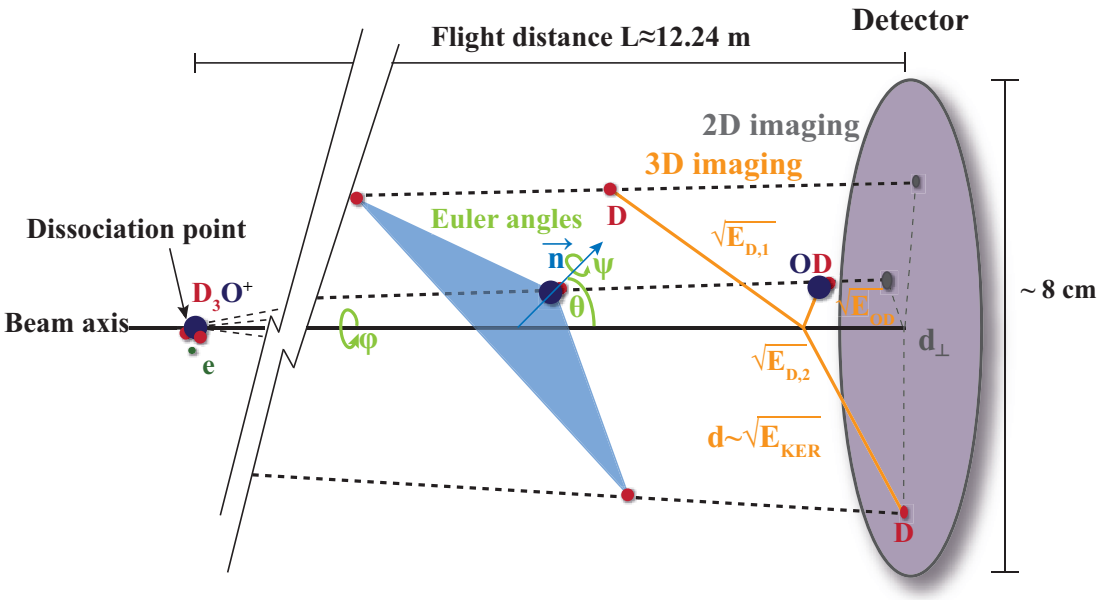

Figure 3.5 Schematic overview of the three-body fragmentation in case of the DR of D_3O^+. The orientation of the dissociation plane defined by the three fragments OD + D + D is described by the three Euler angles θ, φ, ψ.

adapted to the case of non-equal fragment masses in the present experiment.

For a single kinetic energy release E_{KER}, the energy sharing considered relative to the total kinetic energy release E_{KER}, may be represented uniquely by a point P within an equilateral triangle of side length $4/3$ (fig. 3.6 (a)), such that the distances ρ_i of P to each side are proportional to the relative kinetic energy of fragment i, E_i/E_{KER}. Momentum conservation further restricts the allowed region to the inner part of a circle with radius $1/3$ centered at the origin 0 of the coordinate system. An important property of this representation, a so-called *Dalitz plot*, is that isotropically distributed uncorrelated three-body events yield a uniform density of events in the kinematically allowed region. In contrast, any structure on such a representation can be attributed to preferred or avoided fragmentation geometries during the break-up, which often are connected to the shape of the potential energy surface driving the dissociation. In addition, these structures can originate from resonant processes, in which the decay occurs sequentially, i.e. from a two-body break-up with one of its decay products subsequently decaying into two additional fragmentation products. The angular correlation of these fragments becomes visible in the Dalitz plot and therefore makes it an excellent tool for studying the dynamics of three-body decays.

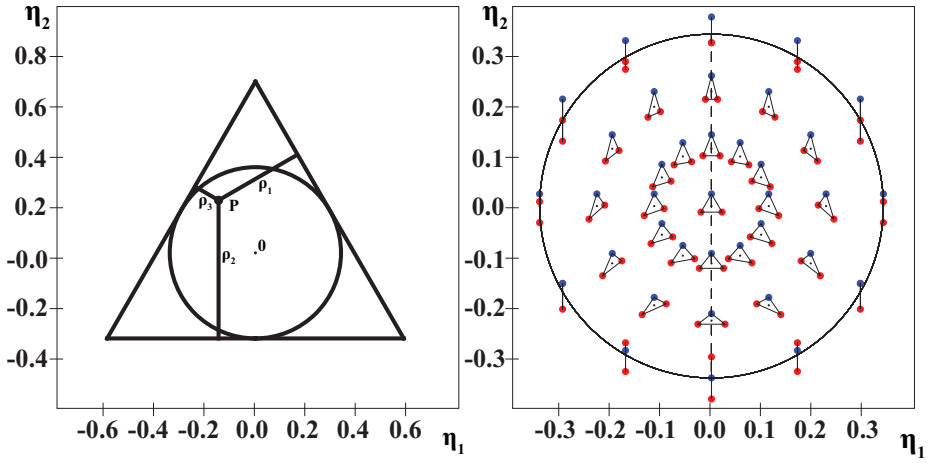

Figure 3.6 Dalitz plot for a fragmentation into three particles with $m_1 = m_2 \neq m_3$. (a) Kinematically allowed region and energetic interpretation. (b) Interpretation in terms of fragmentation geometries. The red spots indicate the fragments with equal mass, the blue spots represents the particle with mass m_3. The plot shows a two-fold symmetry regarding reflection at the $\eta_2 = 0$ axis due to the indistinguishability of the two fragments.

The Dalitz coordinates η_1, η_2 describing a three-body break-up with two equal masses as in the case of $D_3O^+ + e^- \rightarrow OD + D + D$, which is investigated later in this thesis, are defined as

$$\begin{aligned} \eta_1 &= \sqrt{\frac{M}{3\,m_{\mathrm{OD}}}}\,\frac{E_{\mathrm{D}_2} - E_{\mathrm{D}_1}}{\sqrt{3}\,E_{KER}} \\ \eta_2 &= \frac{M}{3\,m_{\mathrm{D}}}\,\frac{E_{\mathrm{OD}}}{E_{KER}} - \frac{1}{3}. \end{aligned} \tag{3.19}$$

As they are normalized to the total kinetic energy release E_{KER}, the geometry of any event can be represented by the same plot, independent of the total energy. The geometric meaning of a certain point in the Dalitz plot depends on the mass ratio of the involved fragments. Figure 3.6 (b) illustrates the arrangements of fragment velocities, measured by an ideal detector, for various points within the Dalitz plot of the fragmentation $D_3O^+ + e^- \rightarrow OD + D + D$. Due to the indistinguishability of the two deuterium atoms, the plot shows a two-fold symmetry with the η_2 axis being the reflection axis. A more detailed description of the fragmentation pattern is given in sec. 6.3.2, whereas the structures arising from a sequential decay in such Dalitz plots will be further considered in sec. 6.4.3.

Chapter 4

Multi-hit Optical Gating Detector for Polyatomic Breakups

The multi-hit optical gating detector providing full momentum information of the DR fragments has been introduced in sec. 3.2.2. This chapter presents details on the signal processing and calibration procedures, emphasizing the latest developments of this detector.

4.1 Data acquisition and signal processing

The data acquisition during a DR fragment imaging experiment is managed independently of the procedures at the TSR such as the injection of the ion beam, the synchrotron ramping, the settings of the electron cooler and target and the shutter control (see e.g. [Les07]). The operation of the 3D imaging detector is carried out by a PC running the commercial software DaVis (**D**ata **a**cquisition by La**Vis**ion), which has been developed by the camera manufacturer LaVision and controls the switch of the intensifier as well as the synchronization and readout of the two cameras. A C-based command language allows modifications by the user to adapt the software to specific needs.

A fast peak finding routine is implemented in DaVis identifying the light spots in each camera frame. In case the intensity of any pixel exceeds a user-set threshold it is compared to that of the surrounding pixels. The position of the maximum intensity, determined by the location of the corresponding pixel, defines the rough fragment position. The averaged intensity of all pixels within a rectangular box

around that maximum defines the intensity of the light spot. The dimensions of this rectangular box are specified by the experimenter. Too small boxes distort the average intensity of the light spot which is the basis for the impact time difference calculation (sec. 3.2.2). However, too large values affect the spatial resolution as neigbouring fragments cannot be distinguished as different spots in C_1. The precise fragment position is then determined by the center-of-weight of the intensity distribution within the box. In order to save storage space on the PC, the raw data acquired by each camera are analyzed online immediately after exposure, saving only position, peak intensity and average intensity of each identified light spot as well as possible additional frame information, such as the arrival time of the event within the 10 ms exposure time (t_{frame}), the storage time in the TSR, information on the electron energy setting of the electron target, the CCD chip temperature etc. in separate data files (IMX-files) as a function of the camera frame number. At times it happens that DaVis misses reading out one of the camera images for a certain frame number, resulting in an mismatch of the two images acquired by C_1 and C_2. By a regular query of whether the number and positions of detected peaks in both frames match within a certain range, an immediate reset of the fast peak finding routine can be prompted, avoiding the storage of mismatching images. The following offline analysis of the IMX-files is then performed using a data analysis software written in C++ using the ROOT framework [CER]. It will be outlined in the next paragraph - for further details see [Nov08a].

4.2 Transverse imaging

The first step in the data analysis is the separation of real DR events from background. In order to obtain fragment positions in transverse direction relative to each other, the camera data need to be converted to physical standard units, i.e. a transformation mapping the pixel array of the CCD to the physical dimensions of the MCP is required.

4.2.1 Background elimination

Background contributions can originate from physical processes other than DR, primarily collisions of the ions with residual gas molecules creating, among others,

neutral fragments. Specifically, these processes are mainly *collision induced dissociation* (CID), where the dissociation of the ion AB^+ is triggered by the collision with a residual gas particle M ($AB^+ + M \rightarrow A + B^+ + M$) and *dissociative charge transfer* (DCT), in which during the collision an electron is captured by the ion from a residual gas particle, leaving the latter ionized ($AB^+ + M \rightarrow AB^* + M^+ \rightarrow A + B + M^+$). At higher collision energies, similar products originate also from *dissociative excitation* (DE), an electron-ion collision process which sets the electron free again after the breakup ($AB^+ + e^- \rightarrow AB^* \rightarrow A^+ + B + e^-$). Setup geometries and detector acceptance account for a different background source. Fragments from DR events with a large kinetic energy release can miss the detector due to the large opening angle of the dissociation cone. In addition, due to the limited MCP efficiency of 60%-80% [Dec96] DR events are lost or – even more critical, in case of polyatomic ions – misassigned. E.g. when observing the 2-body DR channel $D_3O^+ + e^- \rightarrow D_2O + D$, missing out one fragment in the dominant ($\approx 71\%$) 3-body channel $D_3O^+ + e^- \rightarrow OD + D + D$ will suggest a false 2-body event. Vice-versa, a misassignment can also occur due to dark counts of in the MCP being interpreted as an additional fragment.

In fact, many background events can be sorted out based simply on the number of fragments recorded in each camera frame. Only events for which the required number of particles was detected in each camera at the same position (sec. 4.3.1) pass the filter for being analyzed. The fast optical shutter even improves this possibility by only allowing an exposure time of 8 ns for C_2 after the MCP is triggered. However, there are 'real looking' events caused by coincidences of the different effects mentioned above that cannot be identified as false events using only the restrictions on the fragment number. E.g. when missing one fragment signature due to the limited MCP efficiency coincides with an additional single fragment from a residual gas collision or when two dissociations happen within a few nanoseconds but appear to be a single event due to missing out some fragments, the frames will be identified as events of the required number of dissociation fragments.

Further, strong improvements on the background elimination can be achieved by restricting the transversal center-of-mass (cm) of the observed fragments. This is possible due to the high-quality ion beam preparation in the TSR. Phase-space cooling for a few seconds usually results in a projected ion beam diameter of about 1 mm or less on the neutral detectors (see fig. 4.1). The cm is given by the mass-weighted average of the fragment impact positions $\vec{r}_{cm} = \frac{\sum m_i \vec{r}_i}{\sum m_i}$ (with i being the

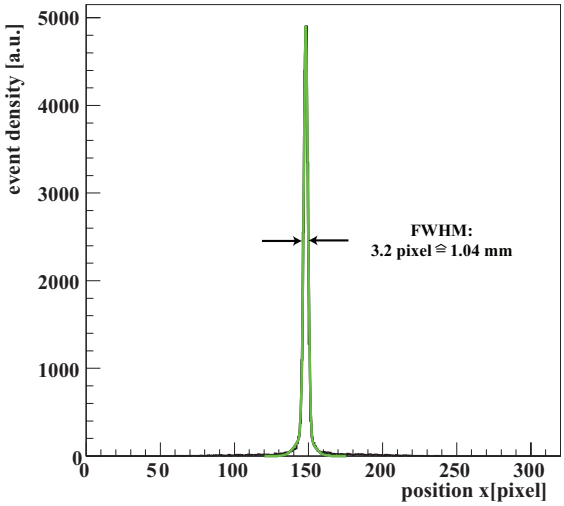

Figure 4.1 Measured vertical cm distribution (during the D_3O^+ 2008 beamtime, black). It is well described by a double Gaussian distribution (green).

fragment index). This requires, however, that the masses can be assigned. Since cm calculation and mass assignment are mutually dependent this is done iteratively. From all possible mass permutations for each event in a data set, the one providing the cm closest to the beam is center chosen. The resulting cm distribution is then fitted by a single Gaussian whose maximum defines the new beam center. The latter is used to redetermine the optimum mass permutation. Several iterations might be necessary until the mean of the cm distribution between two iteration steps changes by less than a certain stability condition set by the user.

by this, the fragment masses are assigned event by event. In addition, the transversal cm distribution is obtained. It is fitted by a double Gaussian distribution – one narrow Gaussian fitting the data and a broad Gaussian representing the background events (fig. 4.1). The latter originates from coincident, but uncorrelated background events so their cm distribution is scattered across the entire detector surface. By restricting the allowed distance between the cm of an individual event and the global cm_g through limiting the transverse deviation

$$|\Delta_{DEV}| = \sqrt{\left(\frac{r_{cm,x} - r_{cm_g,x}}{fwhm_x}\right)^2 + \left(\frac{r_{cm,y} - r_{cm_g,y}}{fwhm_y}\right)^2} \tag{4.1}$$

to a certain value, an effective method to eliminate background has been established. Since the deviations from the global cm_g in both directions are normalized to a value of the full-width-half-maximum ($fwhm$), that is automatically measured and frequently re-defined during a run, any restriction on Δ_{DEV} is independent of any

temporal variations of the ion beam's spatial extension that might occur during long time measurements.

4.2.2 Position calibration

The purpose of the *pixel-to-meter calibration* is to transform the fragment impact positions in the camera image (given in *pixels*) to the positions on the phophor screen (given in *meters*). Facing the phosphor screen directly, the non-gated camera C_1 provides higher resolution for the pixel-to-meter calibration which is therefore applied to the images of C_1. The transformation rule is obtained in a way similar to the mapping between the two cameras, which is described in detail in the next section. Reference points of known relative distances on the phosphor screen are mapped on the pixel positions in the camera frame. These reference points are obtained from an independent measurement in which a metal plate is aligned parallel to and a few millimeter in front of the MCP consisting of a rectangular grid of several holes of 2 mm diameter. These holes are arranged at 10 mm distance apart from each other in both horizontal and vertical direction. The grid allows the impact of neutral fragments only at well defined positions on the screen. By superimposing a large number of events, each hole is mapped onto the MCP and, as a consequence, onto the camera fame. From the observed hole positions in the camera frame and the well-known distances on the phosphor screen a transformation can be derived in the same way as will be described in eq. (4.4), also taking into account higher order effects due to the tilted angle and image distortion of C_1. By applying the obtained transformation on the measured hole positions and comparing the result to the real values, the quality of the transformation can be estimated. A usual setup yields an uncertainty of $\sigma \approx 25\,\mu$m for a single position. At typical spot sizes of 5 x 5 pixels the peak position of a light spot is determined from its intensity distribution with a resolution of 0.5 pixels (see [LaV04]).

The setup has, however, been slightly modified during the HF^+ beamtime. Here, the position of C_1 was closer to the phosphor screen, using a lens with a smaller focal length in order to increase the transversal spatial resolution. The pixel-to-meter calibration with this lens revealed an additional barrel distortion in the picture

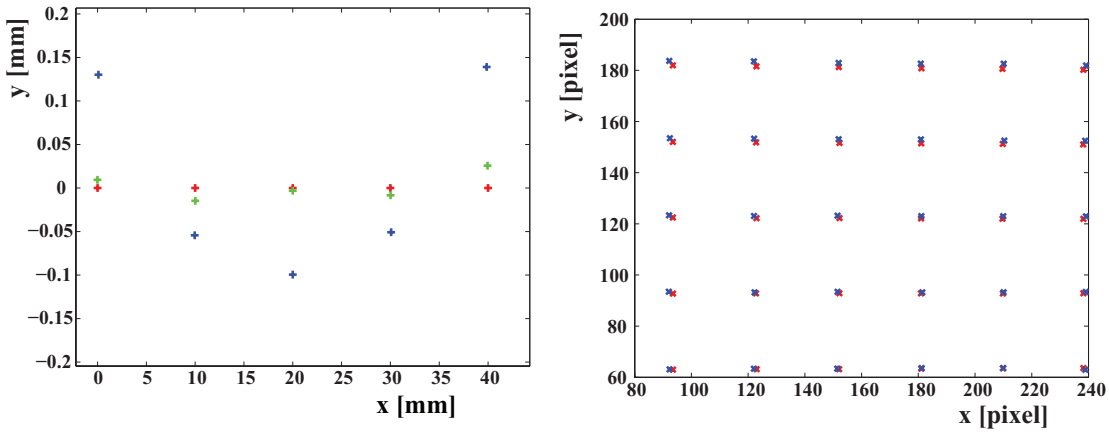

Figure 4.2 Pixel-to-meter calibration. (a) Bottom part of the pixel-to-meter transformation map of the HF^+ 2009 measurement, (red) real grid points from the mask, (blue) pixel-to-meter transformed measured grid points, (green) with additional barrel distortion correction. (b) Comparison of the grid points measured with the α-source (blue) and with neutrals from a non-cooled, widely spread ion beam (red). In order to obtain a pixel-to-meter calibration for beam measurements from the grid measured with the α-source each distance d_α between two grid points needs to be transformed by $d_{beam} = 1.015 \cdot d_\alpha$.

(fig. 4.2 (a) blue), which was compensated for by a secondary correction

$$\begin{aligned} x_f &= x_{corr} + (x_{corr} - x_c) \cdot k_x \sqrt{(x_{corr} - x_c)^2 + (y_{corr} - y_c)^2} \\ y_f &= y_{corr} + (y_{corr} - y_c) \cdot k_y \sqrt{(x_{corr} - x_c)^2 + (y_{corr} - y_c)^2}, \end{aligned} \tag{4.2}$$

where (x_f, y_f) (fig. 4.2 (a) green) are the final corrected coordinates, calculated from the coordinates obtained from the usual pixel-to-meter correction (x_{corr}, y_{corr}) (fig. 4.2 (a) blue), knowing the center of distortion (x_c, y_c). The radial distortion coefficients k_x, k_y are first calculated by eq. (4.2), replacing (x_f, y_f) by (x_u, y_u) (fig. 4.2 (a) red), the undistorted image point expected from the mask. With this additional correction a transformation of the same quality as in measurements performed with the long focal lens could be accomplished.

Instead of using neutral particles originating from ion beam collisions, an α-source mounted in the beam line approximately one meter in front of the MCP detector is sometimes used for calibration measurements. Due to the different angle under which the α-particles hit the detector compared to recombination products, a proportionality factor is necessary to transform each distance d_α between two grid points obtained from α-source measurements (fig. 4.2 (b) blue) by $d_{beam} = 1.015 \cdot d_\alpha$

in order to get the correct points (fig. 4.2 (b) red) for calculating a pixel-to-meter transformation map for ion beam measurements.

4.3 Timing measurement by optical gating

As described in sec. 3.2.2, the relative impact times of the fragments on the MCP are deduced from the measured intensity ratios between the two cameras. These intensities are distorted by various systematical effects and need to be corrected for by different calibration procedures that are presented in the upcoming section.

4.3.1 Mapping of camera frames

The time measurement is based on the intensity ratio of a fragment's light spot recorded by the two cameras C_1 and C_2 and requires a correct mapping of the spots in the images of both cameras. In practice, it is not possible to adjust both cameras with the required accuracy to assure imaging of the same part of the phosphor screen which would automatically yield the correct assignment. The mapping is even further complicated by the fact that, as can be seen in fig. 3.1, camera C_1 cannot be axially centered on the phosphor screen but views it under a certain angle. Therefore, a transformation is needed, mapping the coordinates of C_1 to the ones of C_2. Horizontal or vertical shifts and magnifications between the two cameras are reflected by offsets and linear scalings, respectively, while image distortions due to different angles cause higher order terms in the mapping functions

$$\begin{aligned} x_n &= a_0 + a_1 \cdot x_g + a_2 \cdot y_g + a_3 \cdot x_g^2 + a_4 \cdot y_g^2 + a_5 \cdot x_g y_g \ldots \\ y_n &= b_0 + b_1 \cdot x_g + b_2 \cdot y_g + b_3 \cdot x_g^2 + b_4 \cdot y_g^2 + b_5 \cdot x_g y_g \ldots \end{aligned} \tag{4.3}$$

describing the transformation of a single point in an image of C_2 (x_g, y_g) to the corresponding position in an image of C_1 (x_n, y_n) by a set of linear parameters $(\vec{a}, \vec{b})$. Experience has shown that using six parameters, i.e. up to the quadratic order as shown, yields a transformation of sufficient accuracy. So, an ensemble of points $(\vec{x}_g, \vec{y}_g)$ on C_2 is transformed to $(\vec{x}_n, \vec{y}_n)$ on C_1 by two independent overdetermined

sets of linear equations

$$\begin{aligned} \vec{x}_n &= A_g \cdot \vec{a} \\ \vec{y}_n &= A_g \cdot \vec{b} \end{aligned} \tag{4.4}$$

where the positions in C_2 are supplied in the matrix

$$A_g = \left[\vec{1},\ \vec{x}_g,\ \vec{y}_g,\ \vec{x}_g \cdot \vec{x}_g,\ \vec{y}_g \cdot \vec{y}_g,\ \vec{x}_g \cdot \vec{y}_g\right]. \tag{4.5}$$

The transformation parameters $(\vec{a}, \vec{b})$ are determined by solving eq. (4.4) numerically [Pre92]. For this, single events are used, i.e. frames taken during DR measurement runs containing only one impact. These single events are mainly caused by the finite efficiency of the MCP and by fragments from breakup reactions of the ions with the TSR residual gas. The obtained mapping function is then applied to the measured 3D data. During the analysis it is possible to limit the accepted deviation between the mapped and the measured position in C_1. Events that do not satisfy this condition are considered as coincidence background and discarded.

4.3.2 Intensity calibration

For the calculation of the arrival time difference between two particles, an accurate knowledge of the decay constant τ of the fluorescence emission as well as the correct determination of the position dependent normalization constant $k(x, y)$ is essential, as can also be seen from eqs. (3.8) and (3.9). The decay constant τ is characteristic for the MCP-phosphor screen assembly and is obtained from an independent measurement, using α-particles from a ^{210}Po source (185 MBq; $E_\alpha = 5.3$ MeV). These particles trigger the closing of the optical shutter with variable delay. By this, the intensity is recorded as a function of the gating time from which the decay constant $\tau = (50 \pm 0.5)$ ns can be derived. See [Nov05] for details.

The procedure of calibrating the intensity ratio consists of multiple steps, taking into account and correcting various effects:

- dark image subtraction
- matching the light sensitivity of each camera to one another
- correcting intensity variations caused by the fact that events occur at different

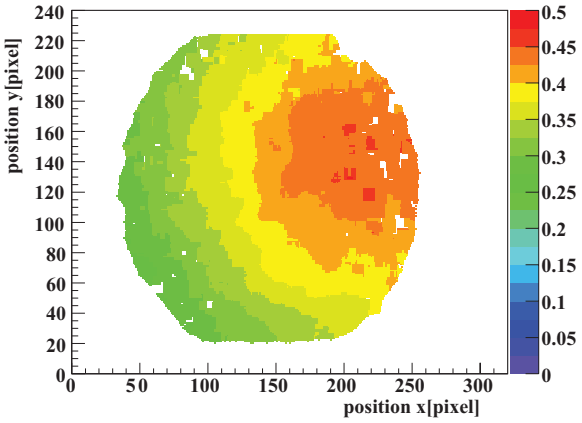

Figure 4.3 Position dependent correction factor $k(x, y)$ of the 2008 D_3O^+ beamtime. It is necessary in order to account for the light sensitivity variations between the cameras.

times t_{frame} within the camera exposure time

- correcting for a position dependence of the shutter closing time.

Directly after camera readout, the raw data are corrected for the pixel dependent *thermal dark current*. This is done by subtracting a dark image, which is acquired before the measurement by averaging over several (usually 50) exposures during which no light is meant to reach the CCD chips, i.e. at a dark phosphor screen but the same exposure time (10 ms). Additionally, time dependent thermal changes that influence the dark current are accounted for by subtracting an averaged intensity value, sampled in the dark upper left corner of each image, from each pixel. This also compensates an offset that was artificially added to the raw image intensity in order to avoid negative values.

The *flat field correction*, which is part of the standard calibration procedure (see [Nov05]), is not applied in the current analysis. In the present setup a homogeneous illumination is only possible for each camera separately, not allowing for matching the light sensitivities between the cameras on a pixel-wise scale. Instead, the *varying light sensitivity* and the possible disturbance of the light path through impurities in the lens are taken care of by a calibration in which the intensities of single light spots emitted from the phosphor screen and observed by each camera are compared. Ideally, aiming for a homogeneously illuminated detector, this is best realized by a measurement during which the electron beam in the target is switched off, resulting in residual gas collisions being the main neutral particle production process and widely spreading the fragments over the detector area. Furthermore, the optical shutter remains open to integrate over the complete light emission in both cameras. Then, any deviation of the intensity ratio from unity is a measure

of the relative camera sensitivity, yielding the position dependent correction factor $k(x, y)$ introduced in eq. (3.9):

$$k(x, y) = \frac{I_2(t_g \to \infty)}{I_1}. \tag{4.6}$$

The intensity ratio of each particle impact at a specific position (x, y) is divided by the corresponding $k(x, y)$, matching the sensitivities between both cameras. Figure 4.3 shows the $k(x, y)$ distribution, properly smoothed in order to avoid statistical artifacts.

4.3.3 Camera frame time correction

All calibration procedures presented previously compensate for position dependent effects of the intensities in both cameras. However, also a time dependence of the measured Ω-value has been observed. Figure 4.4 (a) illustrates the calibrated intensity ratio Ω (eq. (3.9)) of single events – measured with an open optical shutter – observed at different times t_{frame} within the camera frame. While the calibration procedure seems to work properly for events that occur within the first 6 ms, yielding an average Ω-value of 1, a clear decrease of the measured intensity ratio is observed for later fragments. It is caused by the relatively long decay time of the intensifier phosphor screen, which significantly delays the light recorded by the camera C_2. Thus, the light of fragments impinging on the detector shortly before the camera switch-off will still be fully recorded by C_1 while C_2 detects only part of it, resulting in a lower Ω-value. By fitting the measured gradient the decay constant of the second phosphor screen could be determined ($\tau_i = 0.53$ ms). In order to avoid any artifacts in the calibration map (fig. 4.3) only single events that arrived within the first 0.5 ms of the camera exposure time were used. In principle, the measured data then could be corrected for this effect by multiplying any measured Ω with the reciprocal value of the fitted curve. However, as illustrated in fig. 4.4 (c), not only the overall decrease towards the end of the camera frame but also additional small declines within one intensifier opening period can be observed. These effects are assumed to be caused by the various times constants in the power amplifier of the HV switch in the light intensifier (which is AC coupled); these time constants are of the order of a millisecond and might yield some variation and droop of the gating voltage. The calibration procedure applied to compensate for these two effects, the

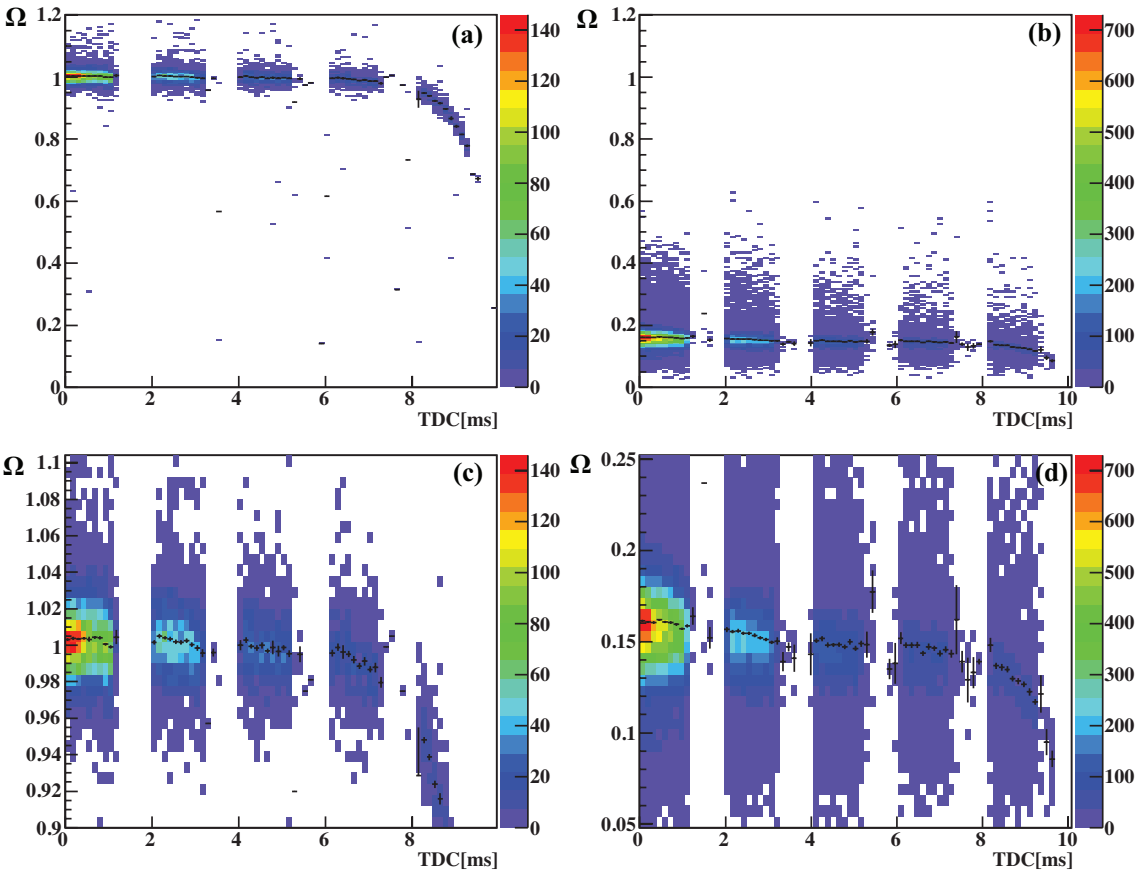

Figure 4.4 Dependence of the calibrated intensity ratio on the event time within the camera exposure time from the 2008D_3O^+ beamtime. (a) Ω vs. t_{frame} from single events of a calibration measurement, i.e. the optical shutter remains open. (b) Ω vs. t_{frame} from single events during the measurement, i.e. the optical shutter is switched. (c) zoom-in of (a), (d) zoom-in of (b). The black, dotted lines indicate the average Ω detected at a certain time t_{frame}.

t_{frame} *correction*, is similar to the position dependent correction. From the single events recorded during the measurement, i.e. the optical shutter is switched during data acquisition (fig 4.4 (b), (d)), the deviation from unity of the intensity ratio as a function of the t_{frame} is determined, yielding the calibration factor $f(t_{frame})$:

$$f(t_{frame}) = \frac{1}{k(x,y)} \cdot \frac{I_2(x,y,t_{frame})}{I_1(x,y,t_{frame})} = \frac{1}{k(x,y)} \cdot \tilde{\Omega}(x,y,t_{frame}). \tag{4.7}$$

The intensity ratio in eq. (3.9) is then additionally divided by $f(t_{frame})$ when calculating Ω_i.

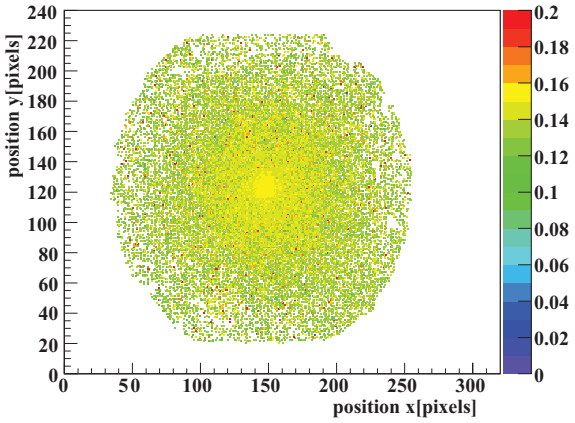

Figure 4.5 Calibrated intensity ratio Ω_s of single particle frames stemming from background events during D_3O^+ DR measurements. Although expected to be a flat distribution it shows a clear position dependence coinciding with the increased local particle impact rate which also implies a high density of the heavy OD particles.

4.3.4 Intensity and timing correction

Despite the application of the previously described calibration procedures a position dependence of the intensity ratio appears during DR measurements. In particular, measurements of heteronuclear molecules are affected where, due to momentum conservation, the impact positions of the heavier fragments are limited to a small area close to the cm, resulting in a locally increased particle impact rate, while the light fragments are distributed over a much larger area. This can be observed in the calibrated intensity ratio already for single particle events (fig. 4.5) and will result in a distorted impact time measurement and consequently a systematical error in the reconstruction of breakup geometries. The origin of this effect is intricate and currently only partly understood. Below, the latest investigations regarding the observed effect are presented, followed by the correction methods applied.

DR measurements on heteronuclear molecules, as opposed to the described calibration procedures, are characterized by strongly asymmetric energy partitioning among fragments of different mass and, consequently, a non-homogenous impact rate distribution on the detector. This helps to identify a dependence of the spot intensity on the fragment mass, which is unexpected for an MCP, but significant, although not sufficient for event-by-event mass identification. The effect is illustrated in fig. 4.6 by means of the DR three-body channel $D_3O^+ + e^- \rightarrow D + D + OD$, with events for which mass identification has been performed by the center-of-mass analysis as described in sec. 4.2.1. The measured intensities of deuterium atoms (c) can be compared with the intensities of OD molecules detected in the same inner area around the center-of-mass (d). Here, a clear difference in the pulse heights is seen. The signal strength of the D atoms impinging on the outer area of the detector does

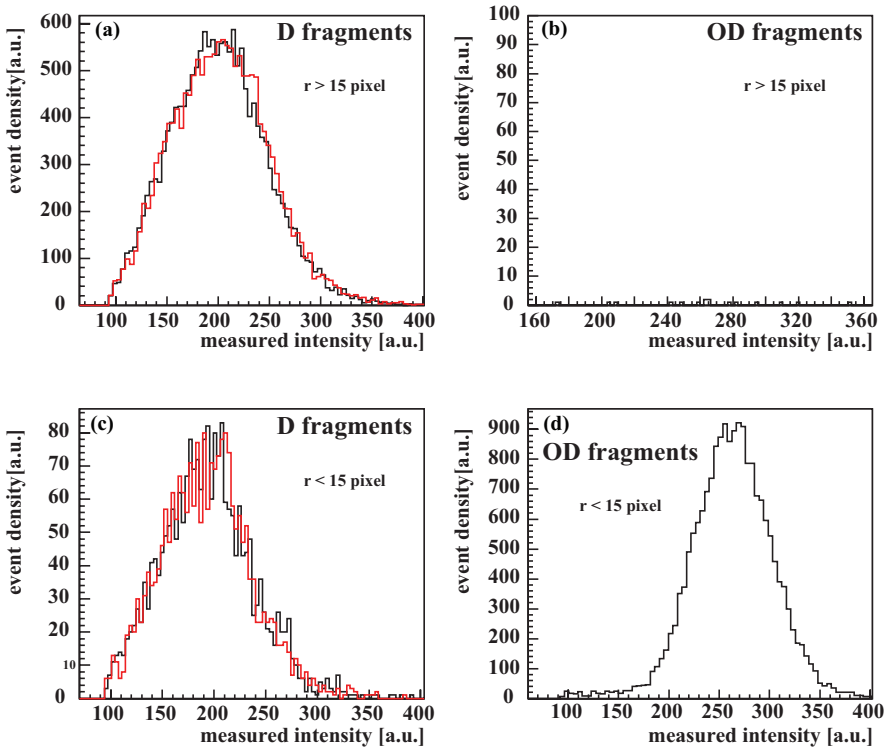

Figure 4.6 Measured intensities by C_1 for the various D_3O^+ DR fragment masses. (a) Intensity of D atoms detected outside a region of at least 15 pixels around the cm. (b) Intensity of OD fragments detected outside a region of at least 15 pixels around the cm. (c) Intensity of D atoms detected by in a region of 15 pixels at most around the cm. (d) Intensity of OD fragments detected in a region of 15 pixels at most around the cm. Black and red represent the intensities for the two D atoms stemming from one event.

not show any significant difference from that of D atoms in the central region of the MCP (fig. 4.6 (a)).

This reveals an additional effect on the light spot intensity and raises doubts about the so called *rate effect*, that has been proposed in an earlier work in order to explain the residual position dependence of Ω across the detector [Nov08a]. This rate effect suggests a detector property, most likely a second, much longer phosphor screen decay constant τ_2 of approximately 5-10 ms, that influences the measured intensities by the locally increased particle impact rate.

Another possible systematic effect in the timing measurement was proposed in [Nev07],

$$t_g(x, y) = -\tau \cdot \ln(1 - \Omega), \tag{4.8}$$

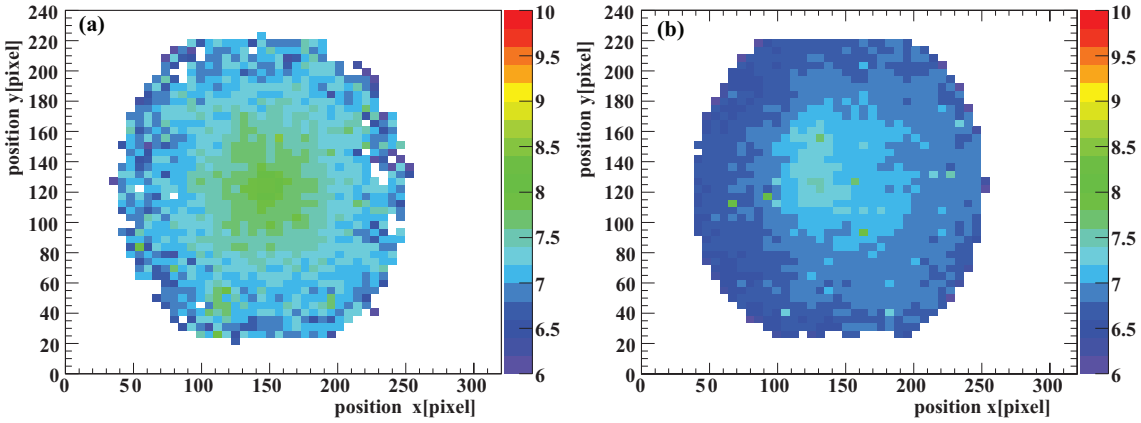

Figure 4.7 Effective gating times $t_g(x, y)$ in ns (a) derived from single events of the D_3O^+ 2008 beamtime, (b) derived from α-particles.

reconstructed from the intensity ratio of single particle hits from a DR measurement of CH_2^+ ions. Here, a similar effect is found when applying eq. 4.8 on events with a single observed fragments from a D_3O^+ beam (fig. 4.7 (a)). When comparing the central area, which is mainly hit by the heavy OD fragments, to the outer region hit by the light D atoms, the gating time t_g reveals a position dependence of 1.5 ns. This effect diminishes to approximately 0.5 ns when recording the gating time t_g of α-particles, shown in fig. 4.7 (b), where any mass or rate depending effect can be excluded due to the monoenergetic, uncollimated α-beam. It was stated that only a position dependence of the true closing time of the shutter (*gating time effect*) and again the decay time of the phosphor screen causing this effect and the corresponding corrections, see eq. (4.10), would result in reasonable distributions of the physical observables. However, variations of the actual closing time of the shutter with position were found independently to be less than 30 ps [LaV04] and therefore too small to explain the observed effects. Thus, the position dependence of t_g may again be related to a position dependence in the evaluation of Ω.

It seems as if none of the proposed reasons can exclusively explain the appearance of the increased intensity ratio or timing shift in the center of the phosphor screen. In addition, further investigations are difficult since the optical intensifier, most probably causing part of the effect, is provided as an built-in component that does not easily allow any detailed analysis of its components. Nevertheless, different correction methods have been developed to compensate for the observed effect symptomatically:

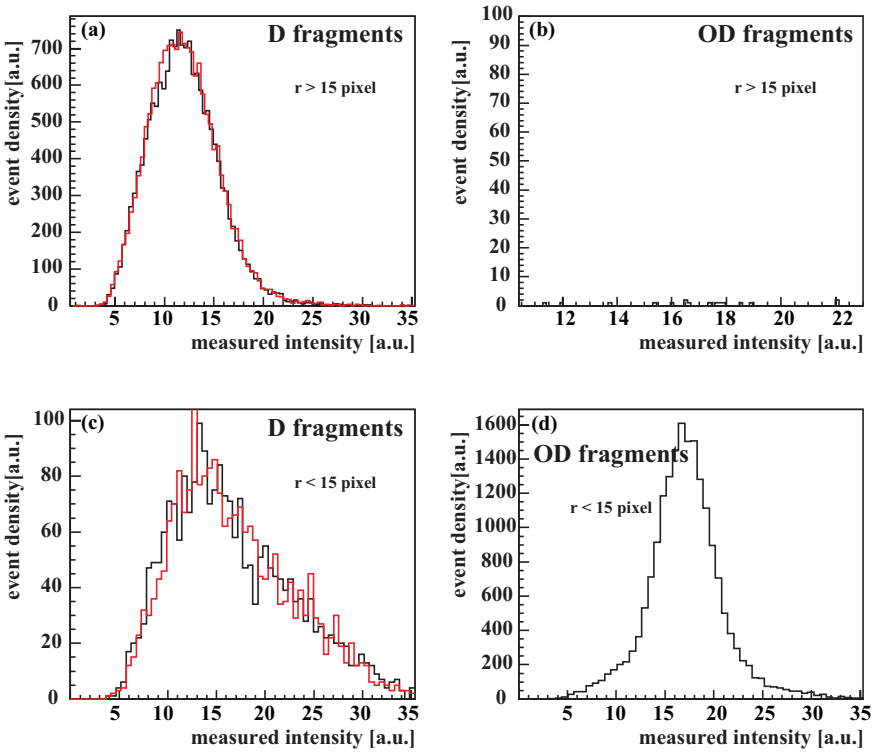

Figure 4.8 Measured intensities by C_2 for the various D_3O^+ DR fragment masses. (a) Intensity of D atoms detected at a distance of at least 15 pixels around the cm. (b) Intensity of OD fragments detected outside a region of radius 15 pixels around the cm. (c) Intensity of D atoms detected in a region of radius 15 pixels at most around the cm. (d) Intensity of OD fragments detected at a distance of less than 15 pixels around the cm. Black and red represent the intensities for the two D atoms stemming from one event.

Multiplicative intensity correction. All methods rely on the measured calibrated intensity ratio of single particle frames, assuming that these events exhibit the same effects on the intensity ratio as actual DR events. In the case of the *multiplicative intensity correction* an additional position dependent correction factor $\Omega_s(x,y)/\langle\Omega_s\rangle$ is applied, which is obtained from these calibrated single particle frames, normalized to its mean value $\langle\Omega_s\rangle$, and properly smoothed in order to avoid statistical artifacts. Applied on the calibrated intensity ratios $\Omega(x_i,y_i)$ of the individual fragments originating from DR breakup events, the correction reads

$$\Omega_{calibrated}(x_i,y_i) = \frac{\Omega(x_i,y_i)}{\Omega_s(x,y)} \cdot \langle\Omega_s\rangle. \tag{4.9}$$

At this, it is crucial to choose the correct particles for calculating $\langle\Omega_s\rangle$. Depending on the detector area from which the Ω_s are used, different average values $\langle\Omega_s\rangle$ are obtained. Due to the non-linear, logarithmical relation between intensity ratio and deduced time (eq. (3.8)) this method leads to varying time differences between the fragments and therefore to various, most probably non-physical, geometries. The systematic uncertainty on the impact time differences induced by the choice of $\langle\Omega_s\rangle$ used in the correction factor has been determined to be less than 0.4 ns in case of the D_3O^+ DR experiment discussed later.

Additive gating time correction. A different correction method was proposed in [Nev07] when trying to compensate for the observed gating time effect, mentioned earlier in this section. Assuming a position dependence of the actual closing time of the shutter for particle i, $t_g(x_i, y_i) = t_{g,const} + \Delta t_g(x_i, y_i)$, this leads to an overall time difference between particles i and j of

$$\Delta t = t_i - t_j = \tau \ln \left(\frac{1 - \frac{\tilde{\Omega}_i}{f(t_{frame})\cdot k(x_i,y_i)}}{\frac{\tilde{\Omega}_j}{f(t_{frame})\cdot k(x_j,y_j)}} \right) + t_g(x_i, y_i) - t_g(x_j, y_j), \tag{4.10}$$

i.e. the time difference calculated from the calibrated intensity ratios is corrected by adding the difference of the locally varying gating times at the impact positions of both fragments obtained from single particle frames, see fig. 4.7 (a). Also this calibration map t_g is properly smoothed before being applied.

Additive intensity correction. A combination of the two correction methods mentioned above was proposed when assuming an additional, position dependent light intensity contribution. Hypothesizing that the 'correct' intensity is measured in the peripheral area of the detector where the lighter fragments impact with a lower local rate, these events are used to calculate the calibrated average intensity ratio $\langle\Omega_s\rangle$ from single particle frames. The center part is assumed to contain a light intensity offset of unknown origin, which needs be corrected for by subtracting the difference between the calibrated intensity ratio Ω_s at position (x, y) obtained from single particle frames (fig. 4.5) and the 'correct' average intensity $\langle\Omega_s\rangle$:

$$\Omega_{calibrated}(x_i, y_i) = \Omega(x_i, y_i) - \Omega_s(x, y) + \langle\Omega_s\rangle. \tag{4.11}$$

4.4 Monte Carlo Simulation

After data acquisition and calibration important questions remain unanswered – the influence of the detector properties as well as the effects of approximations and cuts on the obtained results need to be studied in order to draw reliable conclusions on the physics deduced from the data.

Therefore, a Monte Carlo simulation has been developed and implemented in ROOT [CER]. In this simulation DR events are created at random positions in the target overlap region between the molecular ion beam and the electron beam. The instantaneously dissociated fragments then propagate towards the detectors where the impact position of each particle is determined. Below, a detailed listing of the parameters and settings involved in the simulation, used in the analysis of the D_3O^+ DR, is given:

Dissociation. Any dissociation into a three body event with a defined kinetic energy release (KER) can be described by two internal Dalitz coordinates and three external Euler coordinates (chap. 3.3.2). A dissociation isotropic in phase space is simulated by randomly defining the Dalitz coordinates $\eta_1\,[\text{-}\frac{1}{3},\,\frac{1}{3}]$, $\eta_2\,[\text{-}\frac{1}{3},\,\frac{1}{3}]$ and Euler angles $\psi\,[0,\,2\pi]$, $\theta\,[0,\,\pi]$ and $\phi\,[0,\,2\pi]$. Particular dissociation geometries or spatial anisotropies can be enforced by limiting these parameters to specific values.

Internal excitation of the ion. In most cases it is well-founded to assume that, after phase space cooling, the ions occupy the vibrational ground state (see appendix A.2). Regarding rotational excitation however, in contradiction to former assumptions the ions were recently found to be non-thermalized. The quantification of the rotational temperature is not straightforward. Especially in cases where dissociation products can carry away some internal excitation (i.e. the OD fragment in the DR three-body channel of D_3O^+) only minimum excitation limits of the parent ion can be derived. However, in the simulation it can be accounted for by choosing the proper KER.

Kinetic energy release (KER). For a quantitative comparison of simulation and measurement, the distribution of kinetic energies released in the experiment is needed as an input for the simulation. In the present work, this is obtained from a 2D

measurement with the EMU detector, where the Monte Carlo simulation described here is employed for different kinetic energy release values E_{KER}, followed by using the resulting distributions $P(D_\perp^2, E_k)$ to fit the measured $D_\perp^2$ distribution by a sum of such components, similar to eq. (3.16).

In more detail, 3-body break-ups are simulated, assuming an isotropic distribution of dissociation directions (i. e. randomly distributed Euler angles) as well as fragmentation geometries equally distributed in phase space (i. e. randomly distributed Dalitz coordinates). Randomly chosen dissociation points within the interaction region are included in the simulation, as well as limited detection efficiencies caused by the detector geometry. This is done for different kinetic energy releases E_{KER}. The energy range covered by the different E_{KER} values is divided into j intervals $(E_{KER})_j$ and the expected distributions $P(D_\perp^2, E_{KER})$ for given kinetic energy release E_{KER} are integrated over the respective energy bin range and normalized over $D_\perp^2$. Then, the resulting distributions $\tilde{P}(D_\perp^2, (E_{KER})_j)$ are used to fit the measured $D_\perp^2$ distribution by a sum $\sum_j \alpha_j \tilde{P}(D_\perp^2, (E_{KER})_j)$, varying the relative weighting factor α_j. The E_{KER} values of each bin in combination with the corresponding weightings α_j represent the derived KER histrograms [Buh10b], used as an input for the simulation.

Center-of-mass distribution. Also the cm distribution is simulated by adjusting it to the measurement. As shown in fig. 4.1 the beam profile is well described by a Gaussian distribution. The horizontal and vertical standard deviations σ_x and σ_y obtained from a fit of the measured data are used as input parameters.

Pixel-to-meter calibration. The position on the detector is simulated in *millimeter*. However, in order to allow the simulation output to be treated by the same analysis tools as the measured data, the position on the detector needs to be transferred to *pixels*. The conversion factor is obtained from the *pixel-to-meter* calibration of the measurement.

Transverse resolution and minimum distance of observed spots. The peak positions of the measured data are determined with a resolution of 0.5 pixels [LaV04]. This is simulated by smoothing the 'real' center-of-intensity. The probability function defining the displacement of the 'measured' spot center from the 'real' spot

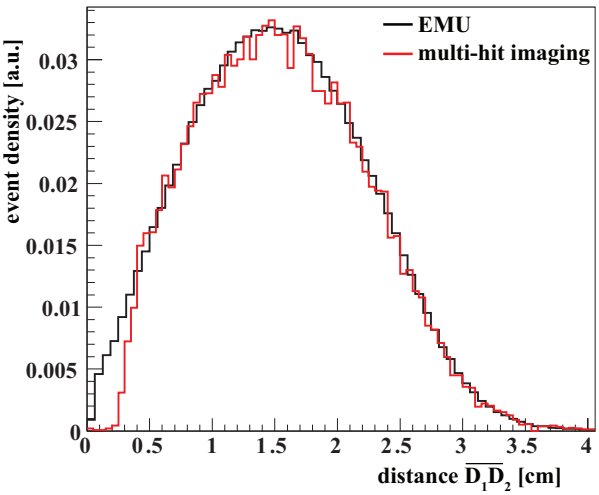

Figure 4.9 2D distances between the two D atoms of the D_3O^+ three body breakup $D_3O^+ + e^- \rightarrow D_1 + D_2 + OD$ acquired with EMU (black) and the multi hit imaging detector (red). Comparing the distributions for small distances reveals minimum detectable distances of approximately 4 mm for the multi hit imaging detector. The minimum distance resolved by the EMU becomes apparent at less than 1 mm.

center is chosen to be a Gaussian distribution.

The minimum distance at which neighboring particles can still be identified is mainly defined by the chosen box size. In the case of D_3O^+ the effect of the peak finding routine could be quantified by comparing the projected distances between between both D atoms to that measured with the EMU detector (fig.4.9) since the latter accepts a considerably smaller minimum fragment distance of approximately 750 μm (sec. 3.2.1). The differing distances of the two detectors from the target center have been accounted for by scaling the distribution measured by EMU with a factor 12.24 m/9.41 m.

3D detector resolution. Since the information on the arrival time difference between the particular fragments of the simulated data is well known, it is utilized to calculate the corresponding Ω. In this step, the simulation does not, apart from the decay constant τ, take into account any specific properties of the phosphor screen, the optical pathway or the intensifier. A Gaussian distributed random term $\Delta\Omega$ is then added to Ω. In contrast to [Str00], where the time resolution is assumed to depend linearly on the gating time itself, i.e. $\frac{\Delta\Omega}{\Omega} = \text{const.}$, it was found later [Men07] that the width of the intensity ratio distribution depends also on the intensity ratio itself. Although a precise comparison reveals some discrepancies between the proposed model $\frac{\Delta\Omega}{\Omega} = \sqrt{\frac{a}{\Omega^2} + \frac{b}{\Omega} + c}$ and the measurement, this model is used in the simulation to obtain the standard deviation of the intensity ratio. An additional scaling factor d was introduced that could be varied in order to reveal the influence of the timing resolution on the different measured quantities, $\frac{\Delta\Omega}{\Omega} = d\sqrt{\frac{a}{\Omega^2} + \frac{b}{\Omega} + c}$.

From $\frac{\Delta\Omega}{\Omega}$ the simulated time resolution σ_t can be derived.

4.5 Time measurement performance

Different calibration procedures to correct for the observed position dependence of the intensity ratios in the timing measurements have been presented in sec. 4.3.4. As mentioned, the discussion about the reason for systematic timing shifts is intricate. Since their origin is not known, all methods will be considered during the data analysis, even though a pure *rate* or *gating time effect*, for which to compensate the corrections were actually developed for, seems to be unlikely (sec. 4.3.4). In the following a comparison of the qualities of the different correction methods regarding time measurement performance will be given.

For this purpose, observables that shed light on the timing performance are required. The main quantities affected by the relative arrival time measurements are the $\cos\theta$ distribution (in a three-body breakup defined as the angle between the normal vector of the dissociation plane and the beam axis (fig. 3.5)) and the kinetic energy release. In the following, data from the D_3O^+ DR measurement of the three-body channel $D_3O^+ + e^- \rightarrow D+D+OD$ at zero detuning energy will be used to illustrate the timing measurement performance.

Figure 4.10 pictures the measured and simulated arrival time differences between pairs of D and OD fragments (fig. 4.10 (a)) and two D atoms (fig. 4.10 (b)). While the simulation yields symmetric functions around zero for an isotropic breakup, the measured distributions are found to be slightly shifted. In the arrival time differences between an OD fragment and any D atom (denoted as D′) that impacts in the center of the detector, a small shift towards negative time differences can be observed, implying a higher count rate of events in which the D′ seems to arrive before the OD fragment. In contrast, the arrival time difference distribution between an OD fragment and any D atom (denoted as D″) that is recorded in the peripheral area is shifted in the opposite direction. Here, the OD fragments are, on average, characterized by a higher Ω value and therefore seem to arrive earlier at the MCP compared to the D″. Even the $\Delta t_{D',D''}$-distribution, which illustrates the distance for each pair of center and peripheral D atoms, the corresponding arrival time difference, is not symmetric – more D′ seem to arrive before the D″ than vice versa.

These observations might be explained when analyzing the average raw intensity

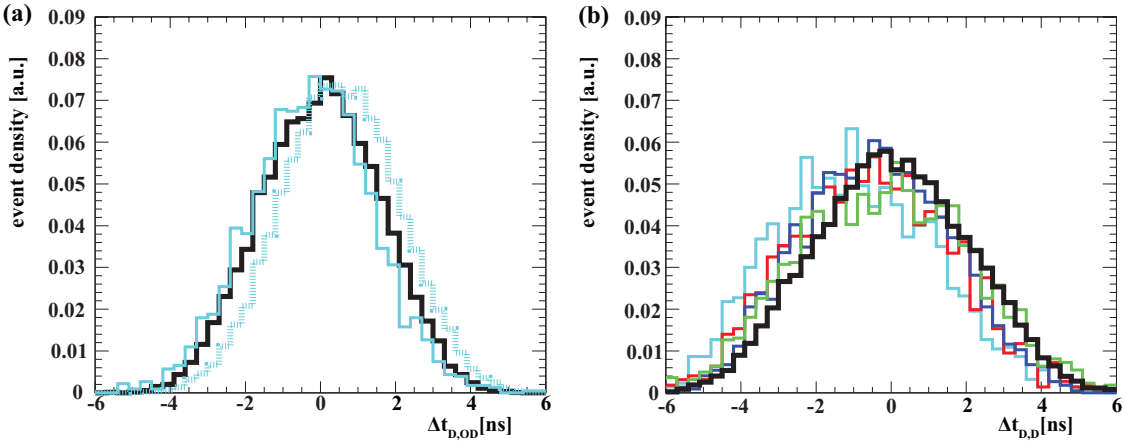

Figure 4.10 Measured and simulated time distributions between each two particles of the DR D_3O^+ three-body channel OD + D + D. (a) Arrival time distances $\Delta t_{D,OD} = t_D - t_{OD}$. The black curves represent the results from a Monte-Carlo simulation with a time resolution of $\sigma_t = 1.1\,\text{ns}$ while the turquoise curves picture measured, standard intensity calibrated data. The slide line illustrates fragments pairs in which the $D = D'$ is detected in the center area (definition see fig. 4.6). The complementary data ($D = D''$ detected in periphery) is represented by the dashed line. (b) Arrival time distances $\Delta t_{D',D''} = t_{D'} - t_{D''}$ of the simulation (black) and measured data with (turquoise) standard intensity calibration, (blue) additional multiplicative intensity correction, (red) additional gating time correction and (green) advanced gating time correction.

values recorded by the two cameras C_1 (fig. 4.6) and C_2 (fig. 4.8). The mean intensity i_D that is measured by C_1 is the same for all D atoms, independent on the impact position (fig. 4.6) (a), (c). A perfect detector then would quantify an Ω_D of:

$$\Omega_D = \frac{1}{k}\frac{I_{2,D}}{I_{1,D}} = \frac{\int_{t_D}^{t_g} i_D\,\tau\,e^{-(t-t_D)/\tau}dt}{\int_{t_D}^{\infty} k\,i_D\,\tau e^{-(t-t_D)/\tau}dt} = \frac{i_D\,\tau\left(1-e^{-(t_g-t_D)/\tau}\right)}{k\,i_D\,\tau}, \tag{4.12}$$

where i_D is the initial intensity of the light spot. However, the mean intensity detected by C_2 is higher for D' than for D''. As mentioned, the impact rate during a DR measurement is not constant but increases towards the center of the phosphor screen. Even though additional long decay constants of the P 43 phosphor screen inside the intensifier are not documented in literature, it is presumed that through the accumulated effect of many particles, intensity adds up in the inner region of the detector with a higher particle count rate. A long-term luminescence of this type

then exposes the CCD chip not only during the gating time of approximately 8 ns, but during the entire exposure time of C_2, started by the PC at t_0 and stopped by an incoming particle on the front MCP at t_g usually within $t_{frame} < 1$ ms (see fig. 4.4). The produced intensity offset b accounts for higher Ω values of any D′ (outer area) yielding the rate effect:

$$\begin{aligned}\Omega_{\mathrm{D}'} = \frac{1}{k}\frac{I_{2,\mathrm{D}'}}{I_{1,\mathrm{D}'}} &= \frac{\int_{t_{\mathrm{D}'}}^{t_g} i_{\mathrm{D}}\,\tau\, e^{-(t-t_{\mathrm{D}'})/\tau} dt + \int_{t_0}^{t_g} b\, dt}{\int_{t_{\mathrm{D}'}}^{\infty} k\, i_{\mathrm{D}}\,\tau e^{-(t-t_{\mathrm{D}'})/\tau} dt} \\ &= \frac{i_{\mathrm{D}}\,\tau\left(1 - e^{-(t_g - t_{\mathrm{D}'})/\tau}\right) + k\, b(t_g - t_0)}{k\, i_{\mathrm{D}}\,\tau}.\end{aligned} \tag{4.13}$$

On average, heavier fragments produce more intense electron cascades in the MCP although the effect is not directly proportional to the mass (see fig. 4.6 (d)). For now, the intensity of a spot produced by an OD fragment in C_1 is assumed to be higher compared to that of a D atom by a factor a: $a\, i_{\mathrm{D}} = i_{\mathrm{OD}}$. Given that, due to momentum conservation, the impact of OD fragments is limited to the detector center, this *mass effect* is convoluted with the *rate effect* described above, predicting an intensity ratio Ω_{OD} slightly smaller than $\Omega_{\mathrm{D}'}$:

$$\begin{aligned}\Omega_{\mathrm{OD}} = \frac{1}{k}\frac{I_{2,\mathrm{OD}}}{I_{1,\mathrm{OD}}} &= \frac{\int_{t_{\mathrm{OD}}}^{t_g} a\, i_{\mathrm{D}}\,\tau\, e^{-(t-t_{\mathrm{OD}})/\tau} dt + \int_{t_0}^{t_g} b\, dt}{\int_{t_{\mathrm{OD}}}^{\infty} k\, a\, i_{\mathrm{D}}\,\tau e^{-(t-t_{\mathrm{OD}})/\tau} dt} \\ &= \frac{a\, i_{\mathrm{D}}\,\tau\left(1 - e^{-(t_g - t_{\mathrm{OD}})/\tau}\right) + b(t_g - t_0)}{k\, a\, i_{\mathrm{D}}\,\tau}.\end{aligned} \tag{4.14}$$

Comparing eqs. (4.13) and (4.14), the diminishing effect of the factor a in the denominator becomes apparent. These above assumptions agree well with the experimental findings $\langle\tilde{\Omega}_{\mathrm{D}'}\rangle = 0.066$, $\langle\tilde{\Omega}_{\mathrm{D}''}\rangle = 0.052$, $\langle\tilde{\Omega}_{\mathrm{OD}}\rangle = 0.062$, and produce the characteristics of the arrival time difference distributions in fig. 4.10. Particles generating systematically higher values of Ω have a higher probability of being (false-) identified as the first arriving fragement. Therefore the arrival time difference distributions are shifted towards positive $\Delta t_{\mathrm{D,OD}}$ and negative $\Delta t_{\mathrm{D}'',\mathrm{D}'}$.

Since the single particle frames are acquired during a DR measurement there is

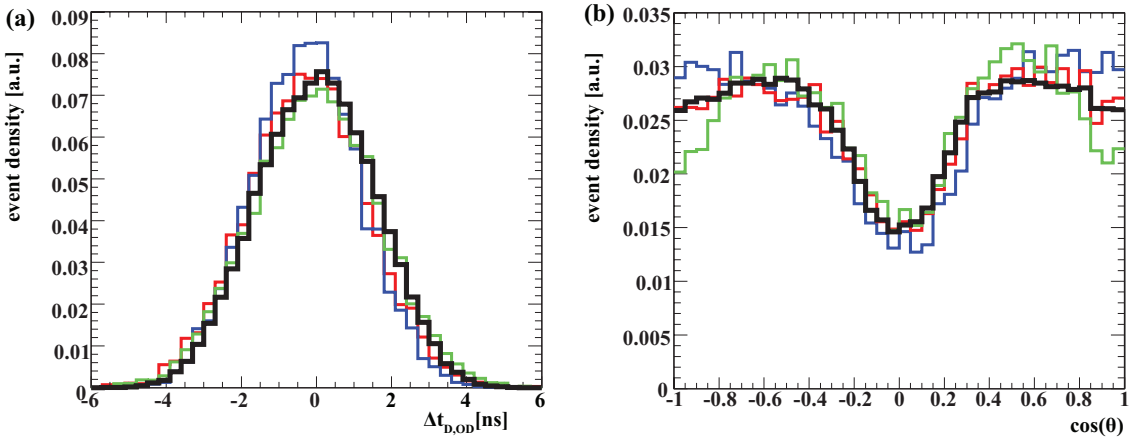

Figure 4.11 Characteristic quantities regarding the timing performance in a comparison between simulation and measured data. (a) Arrival time distances $\Delta t_{\mathrm{D,OD}} = t_{\mathrm{D}} - t_{\mathrm{OD}}$ of the simulation assuming a time resolution of $\sigma_t = 1.1\,\mathrm{ns}$ (black), and measured data with (blue) additional multiplicative intensity correction, (red) additional gating time correction and (green) advanced gating time correction with $c_D = 3.8$ and $c_{OD} = 3.6$ (green). (b) $\cos\theta$ distributions, where θ is defined as the angle between the normal vector of the dissociation plane and the beam axis. Color coding as in (a).

reason to believe that the *rate effect* emerges also in these images, making them good candidates for being used in the correction procedure. Different correction methods (eqs. (4.9), (4.11)) have been described in sec. 4.3.4, from which the *gating time correction* turned out to yield the best results when comparing the corrected data to the simulation, assuming an isotropic breakup. Both *intensity correction* methods cause almost identical results and seem to overcompensate the effect. Therefore, they will not be shown separately in the following. Figures 4.10 (b), 4.11 (a), (b) and 4.12 demonstrate the performance of the *gating time correction* (red) and the *multiplicative intensity correction* (blue).

As can be seen in these pictures, the corrected distributions reduce the average time shifts to well below 1 ns, but still do not match the simulation perfectly. One drawback of creating the correction map from single particles frames is the absence of any information on the fragments. Thus, the *mass effect* remains completely disregarded. In an attempt to account for the latter two additional factors where

introduced yielding the *advanced gating time correction* (compare to eq. (4.10)):

$$\Delta t = t_{\mathrm{D}} - t_{\mathrm{OD}} = \tau \ln \left(\frac{1 - \frac{\tilde{\Omega}_{\mathrm{D}}}{f(t_{frame}) \cdot k(x_{\mathrm{D}}, y_{\mathrm{D}})}}{\frac{\tilde{\Omega}_{\mathrm{OD}}}{f(t_{frame}) \cdot k(x_{\mathrm{OD}}, y_{\mathrm{OD}})}} \right) + c_{\mathrm{D}} \, \Delta t_g(x_{\mathrm{D}}, y_{\mathrm{D}}) - c_{\mathrm{OD}} \, \Delta t_g(x_{\mathrm{OD}}, y_{\mathrm{OD}}), \tag{4.15}$$

with $\Delta t_g(x_{\mathrm{D}}, y_{\mathrm{D}}) = t_g(x_{\mathrm{D}}, y_{\mathrm{D}}) - \langle t_g \rangle_{min}$ and $\Delta t_g(x_{\mathrm{OD}}, y_{\mathrm{OD}}) = t_g(x_{\mathrm{OD}}, y_{\mathrm{OD}}) - \langle t_g \rangle_{min}$. Here, $\langle t_g \rangle_{min}$ is an average value obtained from the edge of the smoothed t_g correction map (fig. 4.7) at which the *rate effect* is assumed to be minimum. Further, c_{D} and c_{OD} are factors that allow to weight the corrections in terms of mass. The green histograms in fig. 4.10 (b) and 4.11 (a) demonstrate the arrival time distributions calculated by eq. 4.15. With the underlying assumption that the dissociation is isotropic, the factors c_{D} and c_{OD} have been determined by optimizing the distributions $\Delta t_{\mathrm{D}',\mathrm{D}''}$, $\Delta t_{\mathrm{D,OD}}$ regarding their axial symmetry around the origin. Further, the number of first arrived particles of each mass has served as a criterion.

In summary, an improvement regarding the understanding of what causes uncertainties in the arrival time measurement and the corresponding calibration and correction methods could be achieved. However, it is still not fully understood. Even though having corrected most measured quantities, such as $\Delta t_{\mathrm{D,D}}$ and $\Delta t_{\mathrm{D,OD}}$, for the suspected effects, the *advanced gating time correction* causes a decline in time resolution, visible in the $\cos\theta$ distribution at $|\cos\theta| > 0.7$ (fig. 4.11 (b)) and shifts the three-body kinetic energy release distribution to slightly higher energy values (fig. 4.12). For an isotropic dissociation and perfect time resolution, the $\cos\theta$ distribution is homogenous for small θ. Why the *advanced gating time correction* worsens the time resolution so strongly compared to the *gating time correction* is unclear. Apparently, correcting the gating times only in terms of mass is a simplification. The idea of subtracting $\langle t_g \rangle_{min}$ is to correct fragments detected in the peripheral area only little while a stronger correction value is applied for particles in the center in order to compensate the *rate effect*. However, this method turns out to be relatively sensitive to the chosen value of $\langle t_g \rangle_{min}$. Fig. 4.10 (b) and 4.11 (a) present the best results that have been obtained so far, but the existence of better scaling factors combined with a different $\langle t_g \rangle_{min}$ cannot be excluded. Moreover, there is no explanation why the scaling factors are so large (fig. 4.12) – the early assumption that single events on average arrive earlier during the camera frame than three body events, i.e. $(t_{g,s} - t_0) < (t_{g,3-body} - t_0)$, cannot be confirmed. In addition, the shape of

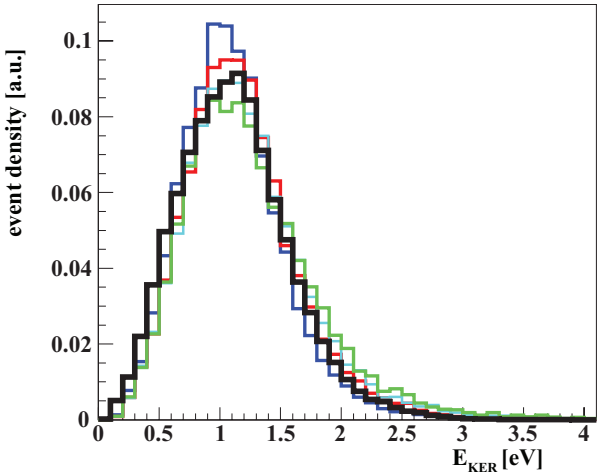

Figure 4.12 Kinetic energy release of the DR three-body channel $D_3O^+ + e^- \rightarrow OD+D+D$. Data obtained by a Monte-Carlo simulation (black), measured data corrected by additional multiplicative intensity correction (blue), additional gating time corrected data (red), advanced gating time corrected data with $c_D = 3.8$ and $c_{OD} = 3.6$ (green).

the raw intensity distribution from light particles was found to be not fully Gaussian. The impact of the light D atoms can produce intensities so low that they happen to be misinterpreted as background (< 95 in C_1, fig. 4.6). Further, as can be seen in fig. 4.8, the intensity distribution detected by C_2 completely loses its Gaussian shape towards higher values. This is most probably caused by an electronic signal too weak to trigger the intensifier. The trigger then is given by a later fragment. The longer exposure time would, under ideal conditions, cancel out in the analysis of the time differences. However, for the same reason that the absolute intensity of higher masses plays a role in the presence of an intensity offset, the extended gating times can be expected to become relevant.

For presenting the data on D_3O^+ in chap. 6, the use of the gating time correction is chosen. Applying this correction, the measured distribution of $\cos\theta$ fits the one simulated for an isotropic decay almost perfectly. While the dip at $|\cos\theta| < 0.4$ is caused by the minimum distance two light spots need to be apart from each other on the phosphor screen in order to be identified as separate spots, the decreased number of events found at $|\cos\theta| < 0.7$ is induced by the finite time resolution. The time resolution is determined by finding the value of σ_t for which the simulated distributions in fig. 4.10 (b) and fig. 4.11 fit the gating time corrected data, yielding $\sigma_t = 1.1\,\text{ns}$. This value is larger than the one obtained in measurements on molecules producing fragments of more similar mass than OD and D in the present case; for CF^+, $\sigma_t = 0.35\,\text{ns}$ was obtained [Nov10]. Hence, the different fragment masses and the different sizes of their impact cones have a large effect on the timing resolution. Still, for D_3O^+ the time uncertainty is significantly smaller than the kinematical

times shifts between the fragments, yielding meaningful data on the 3D kinetic energy release and the Dalitz plots as described in chap. 6.

Chapter 5

Rotationally and Fine-Structure Resolved Dissociative Recombination of HF^+ and DF^+

Hydrogen halides are of fundamental interest. These molecules are ideal systems for studying molecular electronic structure and contribute to the theoretical understanding of the electronic structure of more complicated systems. Hydrogen fluoride (HF) is the simplest of all hydrogen halides. Therefore, HF as well as its ion, HF^+, serve as benchmarks for theoretical studies [Pah98, Bro00]. In addition, the interactions of hydrogen fluoride with electrons and photons are of importance in many fields, ranging from its abundance in interstellar clouds [Neu05] to its applications in industry [Hos99].

In this work, HF^+ recombination experiments with cold electrons have been performed. For the first time, the detection of the neutral particles yields a rotationally and fine-structure resolved dissociative recombination (DR) spectrum. This is possible due to the unique physical characteristics of HF^+, which result in an extremely low kinetic energy release during dissociation. In this chapter, the structure of HF^+ is discussed (as far as necessary) to interpret the presented measurement results. Modeling the data provides highly precise values of the HF^+ and DF^+ dissociation energies.

5.1 On the diatomic ion HF^+

The diatomic molecular ion HF^+ was first observed in the laboratory by photoelectron spectroscopy of the hydrogen halide, HF [Fro67]. Since then, it has been the

subject of both experimental as well as theoretical studies. A short summary on the properties of HF and HF^+ and its general relevance is given in the next section.

5.1.1 Properties and interactions of HF^+

In the early stages, the experiments performed with HF and HF^+ were mainly of spectroscopic nature, as they provide deep insight in the structure and dynamics of the molecules. From the photoelectronic spectra, the outer valence electron configuration of hydrogen halides, a lone-pair π orbital and a bonding σ orbital ($\sigma^2\pi^4$), was obtained for the neutrals [Lem68a, Lem68b]. Shortly after, these measurements were improved, yielding values for ionization and dissociation energies of HF and DF. In addition, a lower limit for the dissociation energy of the ion was reported, $D^0_{HF^+} > 3.41(5)\,\mathrm{eV}$ [Bru70]. In the course of time, resolution was enhanced continuously, leading to improved values of the molecular constants. By detecting the threshold electrons, the spin-orbit splitting in the $X^2\Pi$ ionic ground state could be resolved [Guy76]. In 1975, the emission spectrum associated with the weak $A^2\Sigma^+ - X^2\Pi$ electronic transition was recorded at rotational resolution [Gew75]. These measurements allowed the determination of many important spectroscopic constants of HF^+. Different techniques facilitated further improvement. At the same time, the abundant occurrence of HF in nature and in industry aroused interest not only in its molecular properties but also in its interaction mechanisms with electrons and photons. Research was performed analyzing the behavior of HF and HF^+ in etching plasmas [Hos99], which play an important role in the semiconductor industry. In 1997, HF was observed towards the giant molecular cloud Sagittarius B2, which indicated an abundance of 3×10^{-10} relative to H_2 [Neu97]. Recently, the fine-structure transitions of HF^+ in the $v = 0$ level of the $X^2\Pi$ ground state were revealed by laser magnetic resonance spectroscopy at far-infrared wavelengths [All04]. The molecular parameters of HF^+ could be determined from this measurement with a considerable improvement in precision. A collection of values relevant in this context is listed in tab. 5.1.

The key process in the physics of plasmas, where molecular ions are present, is dissociative recombination. Together with ion-pair formation (IPF) (previously referred to as resonant ion-pair formation (RIP)), this process governs the charge and energy balance in plasmas. Ion storage ring experiments reported the first measure-

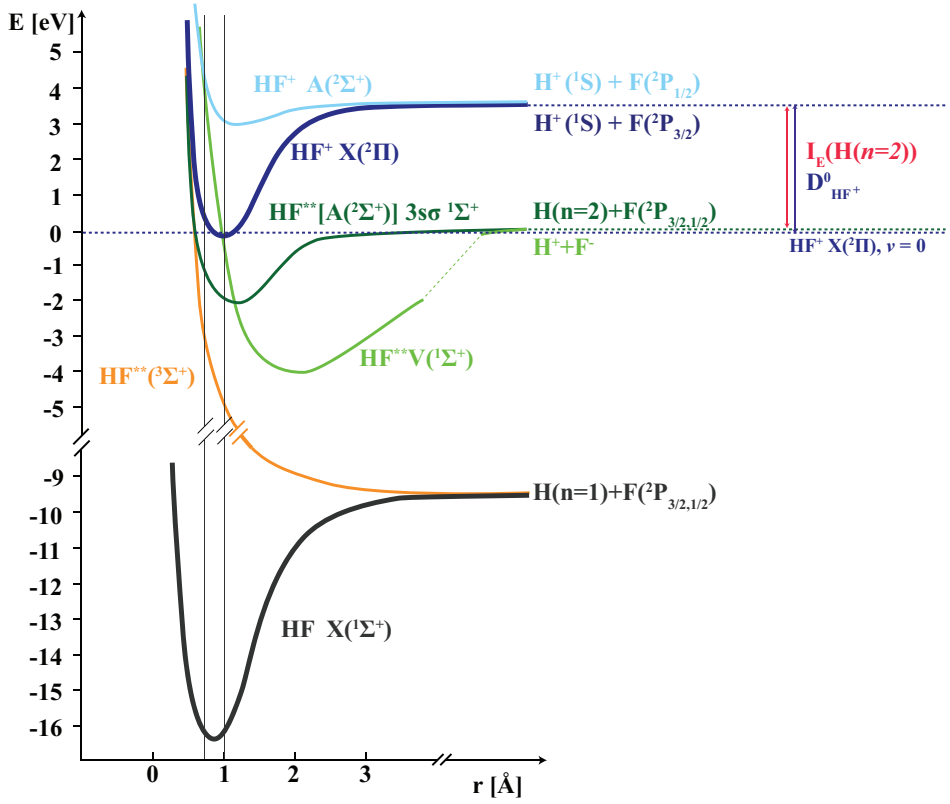

Figure 5.1 Sketch of the potential energy curves relevant for the DR and IPF of HF^+. Curve shapes of the neutral ground state $X(^1\Sigma^+)$, the ion ground state $X(^2\Pi)$ and the first excited ionic state $A(^2\Sigma^+)$ are taken from [Yen95]. Information on the energies of the core excited $3s\sigma$ Rydberg state is obtained from [Yen99]. Theoretical calculations presented in [Roo08] yield the shape of the $^3\Sigma^+$ resonant repulsive state that converges to the atomic states $H(n = 1) + F(^2P)$. Literature reveals discrepancies regarding the potential curve of the lowest stable excited singlet state $V(^1\Sigma^+)$ [Yen95, Ber71]. Here, the latter is illustrated. The vertical lines indicate the Frank-Condon region for excitation from the ground state of HF [Yen95]. In DR, the HF^+ ground state dissociates due to a crossing of the excited $V(^1\Sigma^+)$ state, which correlates with the $H^+ + F^-$ channel, between the classical turning points of the $\nu = 0$ vibrational level. As a second crossing of this state with the excited $3s\sigma$ state occurs at slightly larger internuclear distances, a dissociation into the neutral atomic states $H(n = 2) + F(^2P)$ becomes possible.

ments of rate coefficients and cross sections for this member of the hydrogen halide family [Zon99, Dju01]. Recently, theoretical calculations have also been carried out, calculating the cross section for DR [Roo08] and IPF [Roo09] at different collision energies.

Besides, the interest in studying DR and IPF for HF^+ is also based on some unique physics characteristics of this molecule. Figure 5.1 illustrates the potential curves

Table 5.1 Molecular constants for HF^+, determined from laser magnetic resonance spectrum measurements of the ion. Data taken from [All04]. These constants are used to determine the rotational fine-structure levels of the $HF^+ X^2\Pi$ ground state.

Parameter	Symbol	Value
rotational constant	B_ν	2.122 meV
rotational constant	D_ν	$2.8 \cdot 10^{-4}$ meV
spin-orbit coupling constant	A	-36.130 meV
A/B_ν	Y	-17.023
equilibrium internuclear distance	r_e	1.0016 Å

involved in the DR and IPF of HF^+. The dissociation energy of HF^+, $D^0_{HF^+}$, and the ionization energy of the H(n=2) atom, E_I(H(n=2)), match within the HF^+ rotational energy spacing. The nearly iso-energetic situation between the ground-state of HF^+ and the asymptotic limit $H(n=2) + F(^2P_{3/2})$ leads to kinetic energy releases (KER) in the meV range during the DR of HF^+ at near-zero collision energies. Consequently, a sensitive imaging setup as realized in the present work could possibly resolve single rotational and even fine-structure levels in the transverse distance distribution, which has not been possible with any other collision system before. In addition, the asymptotic limit of the IPF process, $H^+ + F^-$, is also found in the same energy range. This is important as the DR cross section σ_{DR} is influenced by this competing process.

How the dissociative recombination of HF^+ exactly occurs is not fully understood yet. Results from the rate coefficient measurements [Dju01] led to the hypothesis that direct capture and stabilization through the $V^1\Sigma^+$ state accounts for most of the recombinations. This assumption is supported by the general E^{-1} trend of the DR cross section and the finding that the $V^1\Sigma^+$ state crosses the $X^2\Pi$ ion ground state between the classical turning points of the $v = 0$ vibrational level [Dju01]. However, theoretical calculations [Roo08] which only include the direct process of DR are not able to reproduce the cross section below 40 meV. The results from theory overestimate the total cross section, which is found to be significantly smaller than the one for other diatomic molecular ions. In addition, the calculations do not reproduce the structures observed in the measured cross section. These findings led to the conjecture that the so far unconsidered interference effects induced by couplings between the electronic states via bound Rydberg states might explain

the observed structures [Roo08]. In addition, indirect capture into Rydberg states, which then predissociate via the ion-pair state, might play a role in the DR of HF^+.

5.1.2 HF^+: energy level calculation

As pointed out above, the low kinetic energy release in the DR of HF^+ at near-zero collision energy

$$HF^+(^2\Pi_{3/2,1/2}) + e^- \rightarrow H(n=2) + F(^2P_{3/2,1/2}) + E_{KER} \tag{5.1}$$

allows for a transversal distance distribution resolving rotational- and fine-structure of the ion. In order to model the data, the rotational energy levels for both fine-structure series need to be known. Already in 1928, rotational term values of the components of doublet states have been calculated theoretically [Hil28]:

$$\begin{aligned} E_J^{theo}(X^{\,2}\,\Pi_{3/2}) &= B_\nu\Big[(J+\frac{1}{2})^2 - \Lambda^2 - \frac{1}{2}\sqrt{4(J+\frac{1}{2})^2 + Y(Y-4)\Lambda^2}\,\Big] - D_\nu J^4, \\ E_J^{theo}(X^{\,2}\,\Pi_{1/2}) &= B_\nu\Big[(J+\frac{1}{2})^2 - \Lambda^2 + \frac{1}{2}\sqrt{4(J+\frac{1}{2})^2 + Y(Y-4)\Lambda^2}\,\Big] - D_\nu (J+1)^4. \end{aligned} \tag{5.2}$$

Equasions (5.2) describe the energy levels assuming that the diatomic molecule is in an intermediate state between Hund's cases (a) and (b), (appendix A.1). The strength of the coupling between the total electronic spin $\vec{S}$ and the total electronic orbital momentum projection $\Lambda\vec{e}_z$ onto the internuclear distance is given by the spin-orbit coupling constant A. Any coupling between $\vec{K}$ and $\vec{S}$, however, is neglected. Y is defined by the ratio A/B_ν.

In the context of the first rotationally-resolved measurement of the $A^2\Sigma^+ - X^2\Pi$ transition spectrum [Gew75], eqs. (5.2) were applied to the HF^+ diatomic ion for the first time. Fitting the spectrum yielded the molecular constants appearing as parameters in the formulae. As mentioned above, the precision of these constants has been improved considerably by far-infrared laser magnetic resonance spectroscopy [All04]. These values (tab. 5.1) are used for calculating the rotational fine-structure level energies of the $HF^+(^2\Pi)$ ground state by means of eqs. (5.2). The results are given in tab. 5.2. The uncertainty is estimated by comparing the calculated energy levels E_J^{theo} to the experimentally obtained values E_J^{exp} extracted

Table 5.2 Rotational energy levels of the HF^+ and DF^+ fine-structure sets $X\,^2\Pi_{3/2}$ and $X\,^2\Pi_{1/2}$. E_J^{theo} are calculated by means of eq. (5.2) [Hil28]. The spectroscopic constants of HF^+ are taken from tab. 5.1, while the constants of DF^+ are derived from those of HF^+ by correcting for the change in reduced mass (sec. 5.2 and tab. 5.4). From the spectroscopically measured transitions between the spin-rotational levels of HF^+ [All04], the values E_J^{exp} are obtained. All energies are given in meV relative to the $HF^+(X^2\Pi_{3/2}, J = 3/2)$ and $DF^+(X^2\Pi_{3/2}, J = 3/2)$ ground states, respectively.

	HF^+				DF^+	
	E_J^{theo}		E_J^{exp}		E_J^{theo}	
J	$X^2\Pi_{3/2}$	$X^2\Pi_{1/2}$	$X^2\Pi_{3/2}$	$X^2\Pi_{1/2}$	$X^2\Pi_{3/2}$	$X^2\Pi_{1/2}$
1/2	–	34.340	–	34.348	–	35.236
3/2	0	41.030	0	41.046	0	38.673
5/2	10.061	52.153	10.048	52.183	5.408	44.396
7/2	24.151	67.674	24.121	67.724	12.978	52.398
9/2	42.271	87.548	42.217		22.706	62.669
11/2	64.412	111.721			34.586	75.199
13/2	90.563	140.134			48.613	89.973
15/2	120.701	172.721			64.778	106.975
17/2	154.798	209.415			83.072	126.188
19/2	192.815	250.139			103.483	147.593
21/2					125.999	171.167
23/2					150.604	196.888
25/2					177.281	224.931

from the transition measurements [All04]. By calculating the mean square error (mse)

$$\Delta E_J^{sys} = \frac{1}{N}\sqrt{\sum_J (E_J^{exp} - E_J^{theo})^2}, \tag{5.3}$$

where N is the number of experimentally available levels E_J^{exp} [All04], an overall systematic error of $\Delta E_J = \pm 0.009\,\text{meV}$ for the theoretical values is obtained.

Figure 5.2 illustrates the potential energy curves relevant in the DR process[1] $HF^+ \rightarrow H(n = 2) + F(^2P_{3/2,1/2})$. The rotational fine structure levels of HF^+ (blue) as well as the atomic final levels are displayed. In the relevant energy range the $F(^2P)$ features a fine-structure splitting of 50.1 meV [Ral10]. The energy level of

[1] In the following, the electron inducing the fragmentation is omitted in the reaction equations for reasons of simplicity.

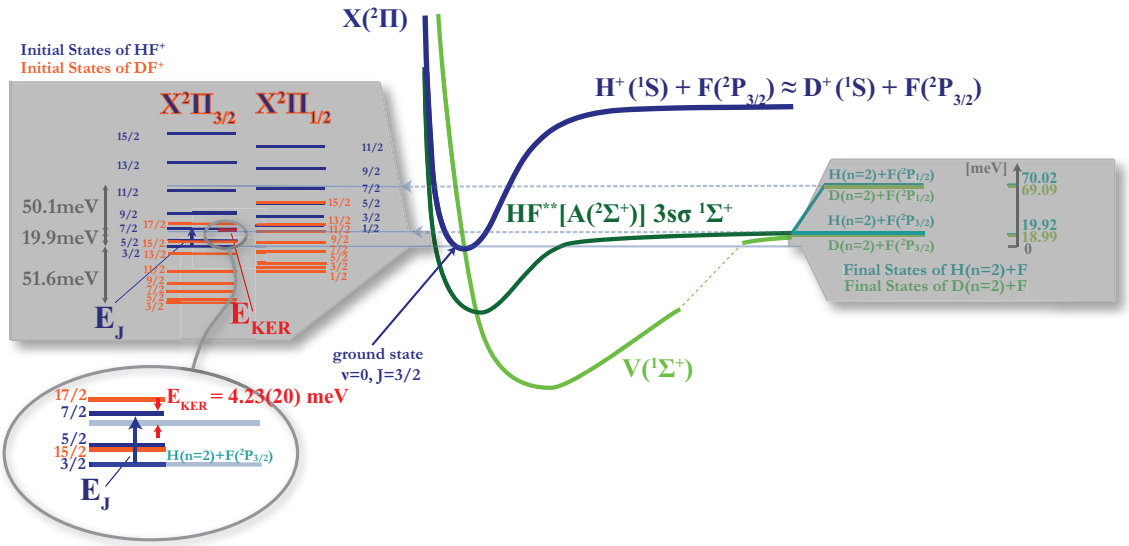

Figure 5.2 Sketch of the potential energy curves relevant for the DR process $HF^+ \rightarrow H(n=2) + F(^2P_{3/2,1/2})$. Rotational fine-structure levels are included for both ions, HF^+ (blue, values given in tab. 5.2) and DF^+ (orange, values calculated in sec. 5.2), and are related to the fine-structure split atomic final states. The kinetic energy release E_{KER} of the dissociation channel $HF^+(X^2\Pi_{3/2}, J = 7/2) \rightarrow H(n=2) + F(^2P_{3/2})$ is obtained from fitting the transversal distance distributions (sec. 5.4.1). This value, in turn, defines the energy level of the atomic final state relative to the ionic ground state $HF^+(X^2\Pi_{3/2}, J = 3/2)$. The fine-structure splitting of fluorine of 50.1 meV is taken from [Ral10]. Levels are not to scale with the potential curves. Curve shapes are taken from fig. 5.1.

the atomic final state $H(n{=}2) + F(^2P_{3/2})$ relative to the $HF^+(^2\Pi_{3/2})$ ground state has been stated to be 22 meV [Dju01]. A more precise value can be predicted from energies obtained by optical spectroscopy:

$$\begin{aligned} \Delta E_{KER} &= \Delta E[HF^+(^2\Pi_{3/2}) \rightarrow H(2s) \; + \; F(^2P_{3/2})] \\ &= -E_{I,\mathrm{HF}} + D^0_{IP,\mathrm{HF}} - E_{I,\mathrm{H}} - \mathcal{E}_{EA,\mathrm{F}} + E_{E,\mathrm{H}(1\rightarrow 2)} \\ &= 18.26(16)\,\mathrm{meV}. \end{aligned} \tag{5.4}$$

The corresponding measured values and their origins are listed in tab. 5.3.

As the ion state $HF^+(^2\Pi_{3/2})$ for $J = 1/2$ does not exist[2], the ionic ground state is $HF^+(^2\Pi_{3/2}, J = 3/2)$ which marks the zero level in fig. 5.2. At near-zero collision energy, there is not sufficient energy for the $J = 3/2$ and $J = 5/2$ states

[2] Hund's coupling case (b) (appendix A.1): for the lowest rotational state, i.e. $R = 0$ and $J = 1/2$, the $K = J - 1/2$ level does not exist, due to the restriction $K \geq \Lambda$, so that this state exists only for $\Omega = 1/2$.

Table 5.3 Relevant energies in the calculation of the HF^+ and DF^+ dissociation energies as well as the energetic differences between the HF^+ and DF^+ ionic ground states and the atomic levels $H(2s)/D(2s)$ + $F(^2P_{3/2})$. For values given without error bar, the last digit is significant.

Symbol	Reaction	Value [eV]	Method
$\mathcal{E}_{EA,\mathrm{F}}$	$F(^2P_{3/2}) \rightarrow F^-(^1S_0)$	−3.401 190(4)	tunable-laser photodetachment threshold (LPT) spectroscopy of F^- ions [Blo89]
$D^0_{IP,\mathrm{HF}}$	$HF(^1\Sigma) \rightarrow H^+ + F^-$	16.063 03(11)	threshold ion-pair production spectroscopy (TIPPS) [Hu06]
$E_{I,\mathrm{HF}}$	$HF(^1\Sigma^+) \rightarrow HF^+(^2\Pi_{3/2})$	16.046 33(12)	Zero kinetic energy photoelectron (ZEKE) spectroscopy [Man94]
$E_{I,\mathrm{H}}$	$H(1s) \rightarrow H^+$	13.598 434	[Ral10]
$E_{E,\mathrm{H}(1\rightarrow2)}$	$H(1s) \rightarrow H(2s)$	10.198 810	Phase coherent comparison with a microwave cesium fountain clock[Nie00]
ω_{e,HF^+}	$HF(^1\Sigma^+) \rightarrow HF^+(^2\Pi_{3/2})$	0.379 61(14)	Threshold photoelectron spectroscopy (TPES) [Yen99]
$(\omega_e x_e)_{\mathrm{HF}^+}$	$HF(^1\Sigma^+) \rightarrow HF^+(^2\Pi_{3/2})$	0.010 02(1)	TPES [Yen99]
$D^0_{IP,\mathrm{DF}}$	$DF(^1\Sigma) \rightarrow D^+ + F^-$	16.134 68(11)	TIPPS [Hu06]
$E_{I,\mathrm{DF}}$	$DF(^1\Sigma^+) \rightarrow DF^+(^2\Pi_{3/2})$	16.064(1)	TPES [Yen99]
$E_{I,\mathrm{D}}$	$D(1s) \rightarrow D^+$	13.602 134	[Ral10]
$E_{E,\mathrm{D}(1\rightarrow2)}$	$D(1s) \rightarrow D(2s)$	10.201 585	[Ral10]
ω_{e,DF^+}	$DF(^1\Sigma^+) \rightarrow DF^+(^2\Pi_{3/2})$	0.275 05(10)	TPES [Yen99]
$(\omega_e x_e)_{\mathrm{DF}^+}$	$DF(^1\Sigma^+) \rightarrow DF^+(^2\Pi_{3/2})$	0.007 26(1)	TPES [Yen99]

to dissociate. The first dissociation channel energetically allowed is $HF^+(^2\Pi_{3/2}, J = 7/2) \rightarrow H(n{=}2) + F(^2P_{3/2})$ with a kinetic energy release of little more than 4 meV. The exact KER depends on the final atomic state and is investigated in the following. As the rotational fine-structure levels of HF^+ are known (tab. 5.2), the final atomic state can be obtained by fitting the kinetic energy releases of the particular dissociation channels $HF^+(^2\Pi_{3/2,1/2}, J) \rightarrow H(n{=}2) + F(^2P_{3/2})$ in the transversal distance distribution.

5.2 On the isotopomer DF^+

Ionized deuterium fluoride DF^+ has been subject to far fewer investigations than HF^+. A number of spectroscopic measurements on HF/HF^+, quoted in the previous section, have also been performed on DF/DF^+. Due to the constantly improving resolution, recent threshold ion-pair production spectroscopy (TIPPS) experiments on the neutrals HF and DF yielded an estimate of the Born-Oppenheimer breakdown in the ground electronic state of the neutral molecule [Hu06].

Considering the DR of deuterium fluorine, however, no experiments have been reported in literature.

DF^+: energy level calculation

In the Born-Oppenheimer approximation, the major energy level differences between two isotopes result from unlike vibrational ground states and modification of the spacing between the rotational levels due to the change in the reduced mass. For low v, the electronic potential can be approximated by a harmonic potential including higher-order anharmonic corrections. This allows the calculation of vibrational levels via (eq. III., p. 76 in [Her54])

$$G(v) = \omega_e(v+\frac{1}{2}) - \omega_e x_e(v+\frac{1}{2})^2 \quad \xrightarrow{v=0} \quad G(0) = \epsilon^0 = \frac{1}{2}\omega_e - \frac{1}{4}\omega_e x_e. \tag{5.5}$$

With the vibrational constants listed in tab. 5.3, the vibrational ground state of DF^+ is calculated to lie below the one of HF^+ by $\Delta G(0) = [G(0)]_{HF^+} - [G(0)]_{DF^+} = 0.051\,59(17)\,\text{eV}$.

The theory behind eqs. (5.2) is based on coupling considerations between the electron spin, the electronic orbital angular momentum and the angular momentum of the nuclear rotation, which are not affected by a substitution of the hydrogen in HF^+ for a deuterium atom. Hence, like for HF^+, the rotational term values of the DF^+ doublet states components are calculated by means of eqs. (5.2). As there are no spectroscopic constants available for calculating the rotational spacings of DF^+, values are derived from those of HF^+ (tab. 5.1) by correcting for the change in reduced mass, $\mu_{HF+} = 19/20\,\text{u} \rightarrow \mu_{DF+} = 38/21\,\text{u}$, as follows.

Under the assumption of a harmonic potential, the average radius r_e does not

Table 5.4 Molecular constants for DF^+, derived from those of HF^+ (tab. 5.1) by correcting for the change in reduced mass. These constants are used to determine the rotational fine-structure levels of the $DF^+(X^2\Pi)$ ground state.

Parameter	Symbol	Value
rotational constant	B_ν	1.114 meV
rotational constant	D_ν	$7.6 \cdot 10^{-5}$ meV
spin-orbit coupling constant	A	-36.130 meV
A/B_ν	Y	-32.536

change due to the ground-state level shift. The difference in r_e between HF^+ and DF^+ because of the an-harmonicities can be neglected. Even though a value for $|r_{e,HF^+} - r_{e,DF^+}|$ is not reported in literature, it can be estimated from the behavior of other diatomic molecules to be below 0.0007 Å, as in the case of OH/OD [Ral10]. With $r_{e,HF^+} \approx r_{e,DF^+} = r_e$, the rotational constant of DF^+ is derived by

$$B_{\nu,DF^+} = \frac{\hbar}{4\,\pi\,c\,r_e^2 \mu_{HF^+}} \frac{\mu_{HF^+}}{\mu_{DF^+}} = B_{\nu,HF^+} \frac{\mu_{HF^+}}{\mu_{DF^+}}. \tag{5.6}$$

A similar procedure is applied to determine $D_{\nu,DF^+} \sim 1/\mu^2_{DF^+}$.

The fine-structure splitting constant A is expected to be independent of the molecular mass. Eqs (5.2) are based on the general ansatz $E_{FS} = A \cdot \Lambda \cdot \Sigma$, where A only depends on the interaction of a particular spin with the orbital momentum of the same electron and the orbital momenta of all other electrons, i.e. $A_{HF^+} = A_{DF^+} = A$. The constants derived from these considerations can be found in tab. 5.4.

The term values of DF^+ are listed in tab. 5.2 and illustrated in fig. 5.2. Apart from any effects beyond the Born-Oppenheimer approximation, the electronic ground state potentials of HF^+ and DF^+ are identical at large internuclear distances. Thus, the atomic final levels D(2s)+F(^2P) can be calculated relative to the H(2s)+F(^2P) levels by taking the slightly different ionization energy of the 2s states into account, which lies 0.925 meV lower ([Ral10] in tab. 5.3). Using the quantities in tab. 5.3, the predicted energy release from the DF^+ ground state is

$$\begin{aligned} \Delta E_{KER} &= \Delta E[DF^+(^2\Pi_{3/2}) \rightarrow D(2s) \,+\, F(^2P_{3/2})] \\ &= -\,E_{I,DF} + D^0_{IP,DF} - E_{I,D} - \mathcal{E}_{EA,F} + E_{E,D(1\rightarrow 2)} \\ &= 71.3(1)\,\text{meV}. \end{aligned} \tag{5.7}$$

5.3 Experimental setup and procedures

Imaging experiments on the DR of HF^+ have been performed twice using the heavy ion storage ring TSR. The kinetic energy release measured in the first beamtime in September 2007 already yielded a precise value of the HF^+ dissociation energy. As the measurement had not been optimized for this purpose and small discrepancies were found during the analysis, the measurements at near-zero collision energy were repeated two years later, this time with better control of all relevant parameters.

The ions were produced in a Penning ion source containing a mixture of CF_4 and H_2 gases. After extraction from the source, the ions were mass-selected and brought to 2.105 MeV by a single-stage Van-de-Graaff accelerator. They were then injected into the TSR and, within 2 s, brought to a final energy of $E_B = 4.65\,\mathrm{MeV}$ by synchrotron acceleration. As pointed out in [Kra09], a low electron temperature in the co-moving reference frame of the stored ions is of particular importance for efficient phase-space cooling at low beam velocities. Due to the much lower temperature of the photo cathode, the electron target, with an electron beam density of approximately $3 \cdot 10^6\,\mathrm{cm}^{-3}$, was not only used for inducing electron-ion collisions but also served as the cooling medium for the ion beam. Storage for another 2 s after the end of the acceleration ramp was sufficient to provide a well phase-space cooled ion beam with a diameter of less than 0.5 mm. This additional storage time ensured that the internal relaxation of the ions which are most likely produced in an initial state of vibrational excitation. According to theoretical calculations [Wer84], the lifetime of the excited vibrational levels within the $X^2\Pi$ state of HF^+ is in the millisecond range ($\tau_{\nu_1 \to \nu_0} = 1.6\,\mathrm{ms}$). In the same work, electronic radiative decay is predicted to deplete the excited $A^2\Sigma^+$ state on timescales of the order of 20 μs. These calculations provide evidence that at the time of shutter opening (4 s after injection), the infrared active ions have already decayed to their vibrational ground state. Following the electron target, the neutral fragments produced in the recombination of ions and electrons could now reach the multi-hit MCP detector where their impact positions were recorded. For each injection cycle, data were taken for 12 s.

In comparison to previous measurements, the spatial resolution of the neutrals' transverse impact positions was particularly optimized. For this purpose, the non-gated camera C_1, equipped with a lens of shorter focal length, was placed axially,

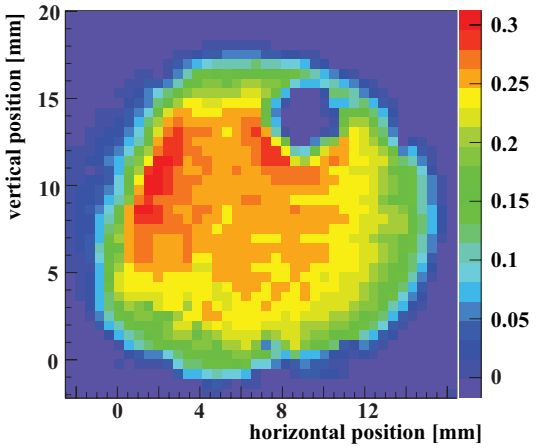

Figure 5.3 Electron beam profile revealing a hole in the electron density due to a defect of the photo cathode, measured at expansion factor $\alpha_t = 30$.

centered in front of the phosphor screen at a distance of approximately 21 cm. This in fact, inhibited 3D imaging, but allowed for an increased transversal spatial resolution and reduced the perspective distortion caused by the angle under which the camera usually views the screen. As discussed in sec. 4.2, due to the small focal distance, non-linear radius mapping from the phosphor screen to the image occurs. The so-called *barrel distortion* diminishes the radius mapping for large radii in comparison with small radii. However, an effective calibration method compensating for this effect, also presented in sec. 4.2, results in an almost homogeneously distributed conversion factor of 0.16 mm/pixel in both directions. The typical spot-size did not exceed 5×5 pixels, i.e. $0.8 \times 0.8\,\mathrm{mm}^2$. As no 3D imaging was intended, the voltage settings at the MCP differed slightly from the usual setup ($V_{MCP} = 1.8\,\mathrm{kV}$, $V_{phosphor} = 3.5\,\mathrm{kV}$). The intensity threshold value of camera C_1 was set to 300.

In order to measure the kinetic energy release with the best precision possible, all other quantities needed to be known precisely. During data acquisition, the ion beam energy was controlled several times by measuring the revolution frequency of the beam. Due to the low ion current of approximately 100 nA, the signal amplitude induced in the Schottky-noise pickup electrode – usually the standard way to determine E_B – was too weak to be measurable. During this measurement, the effect of a radiofrequency (rf) field, set close to the 34^{th} harmonic of the ion revolution frequency, but outside the range of synchrotron phase stabilization, was observed for the first time. The presence of the rf field caused pickup signals representing the revolution frequencies of amplitudes that were high enough to be detected by the pickup electrodes. These findings were further investigated in subsequent experiments [Kra10]. By repeating this procedure multiple times between the mea-

surements, a constant ion beam velocity could be assured.

The measurements have been focused on DR processes at near-zero collision energy. After finding the proper target settings that provided a well phase-space cooled ion beam, it was intended to keep these settings constant, especially the electron acceleration voltage and electron current. In addition, the electron beam profile was controlled at regular intervals. Data was acquired for three different electron target magnetic expansion factors ($\alpha_t = 20, 30, 40$). Unfortunately, the photo cathode used during the $\alpha_t = 30$ measurement revealed a defect that caused a localized minimum in the electron density (fig. 5.3). Due to the single-state resolution, this imperfection, in turn, had visible effects on the projected squared distance distribution. In order to rule out possible systematic effects in further analysis, the $\alpha_t = 30$ dataset was discarded.

During the same beamtime, experiments were also performed on the DR of DF^+, produced by a gas mixture of CF_4 and D_2. The accelerator line and TSR were operated at the same magnetic field settings, which due to the different charge-to-mass ratio enforced a slightly slower ion beam of 4.43 MeV energy. The DR of DF^+ was only measured for one magnetic expansion factor, $\alpha_t = 20$.

During the first HF^+ beamtime, DR measurements have also been performed for higher collision energies. After a precooling phase of 5 s, the shutter was opened and neutrals were detected for 10 s, originating from ion-electron collisions at 140 meV energy in the cm frame. For this measurement, the camera was moved further away from the phosphor screen, allowing the detection of events with larger transversal kinetic energy releases. In addition, measurements at near-zero collision energy have been performed at the same camera settings in order to visualize more events dissociating into the H(n=1) + F(^2P) channel.

Data analysis

The precision of the kinetic energy release measurement depends on many parameters. Usually, at typical kinetic energy releases of a few eV, rotational excitation of the parent ion cannot be resolved but rather causes a broadening of the projected distance distribution of the two neutrals in the detector plane. However, in the DR process of ground-state HF^+, the lowest kinetic energy released is expected to be of only $E_{KER} \approx 4$ meV, corresponding to a projected distance of $d_\perp \approx 1.7$ mm.

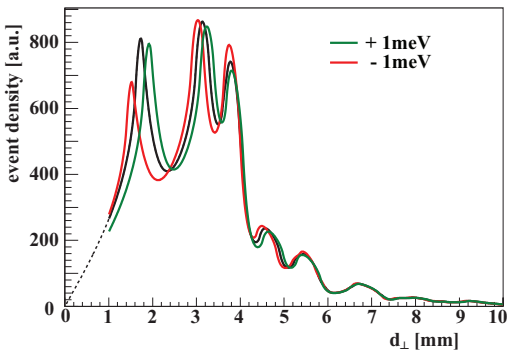

Figure 5.4 Fitted transversal distance $d_\perp$ of the neutrals H and F after DR of HF^+. (black) Optimized fit, leaving KER as a free parameter. (green) Same fit, but assuming a KER increased by 1 meV compared to (black). (red) Same fit, but assuming a KER decreased by 1 meV compared to (black).

The event histograms as a function of $d_\perp$ are fitted by a model function that is obtained from the analytical formula in eq. (3.15). Integrations are performed over the electron energies using the flattened energy distribution of eq. (3.2) with $k_B T_{e,\perp}$ and $k_B T_{e,\parallel}$ as parameters; the electron energies E_e are added to the energy release E_{KER}. A fixed interaction length L_t and a distance L between the center of the interaction region and the detector as well as an ion beam energy E_B are applied. Finally the distances are blurred with a Gaussian standard distribution $\sigma_{blurred}$. A typical fit function is given in fig. 5.4, which illustrates the fit of the lowest kinetic energy released being at $E_{KER} \approx 4$ meV (black curve). The change in projected distance caused by a change in the kinetic energy released, $\Delta E_{KER} = \pm\, 1$ meV is given by the green and red curve, respectively. In reverse, for small $d_\perp$ a small variation $\Delta d_\perp$ leads to significantly different measured kinetic energy releases. The accuracy of the fitting function was confirmed by applying it to simulated data from a Monte-Carlo procedure, which is based on the one introduced in sec. 4.4 but extended by some additional components.

Several parameters influence the detector resolution, such as finite phosphor screen granularity, finite MCP channel density (channel diameter $\varnothing = 25\mu$m) and position broadening within the Chevron due to the gap between the two MCP plates, which causes a spread of the electrons across multiple channels. There is not much known about these effects, leading to distinct assumptions that need to be made in a simulation. Therefore – in a simplified model – the transverse position resolution is assumed to be determined only by the MCP channel size, causing a position center spread of $\sigma_{blurred} \geq 25\,\mu$m.

The error on a spot position caused by the *DaVis peak-finding routine* is analyzed by varying the camera distance, peak-finding-box size and spot size. For box sizes

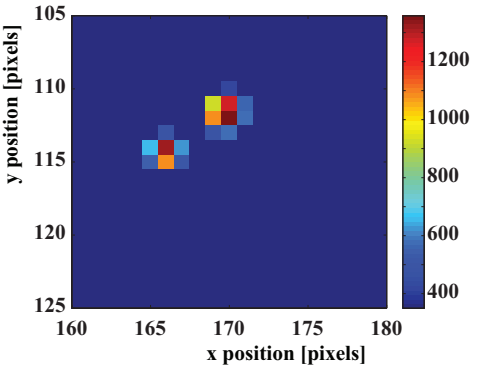

Figure 5.5 CCD camera image with typical spot sizes of the neutrals H and F originating from HF^+ DR measurements. By setting the search box-size to 5×5 pixels, artifacts created by the *DaVis peak-finding routine* can be avoided. The conversion from pixel to millimeter is 1 pixel $\widehat{=}$ 0.16 mm.

smaller than the spot diameter, the determined center-of-intensity turns out to depend strongly on the latter and leads to distributions in which the center-of-intensity is not equally distributed over the entire pixel but concentrated on the pixel center. A correction method, however, has been developed accounting for this effect.[3] After applying this correction to the measured data, the effect of the *DaVis peak-finding routine* is small compared to the position uncertainty due to the finite MCP channel diameter and therefore negligible. During the beamtime in which the data presented here was acquired, this effect has been addressed by setting the search box-size to 5×5 pixels, which is larger than the average spot diameter and therefore assures to cover the entire spot. A typical camera image for the smallest but still accepted spot distance of ~ 0.8 mm is given in fig. 5.5.

Fitting procedure

The fitting routine is implemented in ROOT [CER]. A new class `TO2DDD2B` has been developed, providing the fit function described above[3] (fig. 5.4). For fitting the histogram, the standard ROOT method `TH1::Fit` is used, which internally calls the `MINUIT` fitter.

The fitting procedure is tested by applying it to the simulated data. In case the data was produced assuming perfect conditions, i.e. $E_d = 0$, exactly known constants and vanishing detector effects, the fitted branching ratios of the particular dissociation channels and the obtained offset in the KER of all channels match the simulated parameters within the error bars.

The measured data is influenced by numerous quantities. In the fit, the target length L_t, the target-detector distance L, the longitudinal temperature $T_{e,\|}$,

[3] O. Novotný, private communications

the ion beam energy E_B and the blurring parameter σ_{blurr} are set to fixed values that are known from independent measurements. The rotational energy differences contributing to the KER of the individual signal components are also set fixed according to tab. 5.2. Limiting the number of free parameters is necessary to obtain a converging fit.

Each fit yields optimum values for the amplitudes of the contributions with various J and Ω, ΔE_{KER} of the KER corresponding to ΔE in eqs. (5.4) and (5.7), branching ratios and the transverse electron temperature $T_{e,\perp}$. From the deviation between fitting results and simulated values the influence of the parameter under consideration on the measured KER and $T_{e,\perp}$ can be quantified and systematic errors can be determined. In addition, the goodness-of-fit is reported in terms of the reduced sum of squared fit derivations[4] $\tilde{\chi}^2$.

5.4 Experimental results

The basis of all experimental results is the application of the fitting routine to the measured data. From the least squares fit, the kinetic energy release E_{KER} as well as the contributions of the individual dissociation channels at different collision energies are determined.

5.4.1 DR at near zero collision energy

At near-zero collision energy, data was measured for two different magnetic expansion values ($\alpha_t = 20, 40$), which implies at two different electron densities ρ_e and transversal electron temperatures $T_{e,\perp}$. Both data sets are analyzed individually by applying the fitting routine described in the previous section. As the energy spacing between the individual fine-structure rotational levels is assumed to be correct, ΔE_{KER} is the same for all dissociation channels and can be fitted globally. In addition, the transversal electron temperature $T_{e,\perp}$ is extracted from the fit. The values of the fixed parameters are listed in tab. 5.5 and are based on the following assumptions:

[4] $\tilde{\chi}^2 = \chi^2/n_d$, with n_d, the number of degrees of freedom, equal to the number of data points minus the number of fitted parameters [Nak10].

Ion beam energy E_B. The ion beam energy E_B is calculated from the revolution frequency measured by the Schottky pick-up electrode, which has been kept stable during data acquisition. The circumference of the actual ion orbit in the TSR is assumed to be 55.42 (15) m, where the given estimated error determines the uncertainty on E_B. An alternative way to calculate E_B is to determine the electron energy during cooling, i.e. at matching beam velocities. For this approach, the electron acceleration voltage U_{target}, the space charge potential ΔU of the electron beam and the difference in workfunction $\Delta\Phi$ between the GaAs photocathode and the chamber walls need to be known precisely [Sho]. Even though stable conditions of the rest gas pressure, the electron current I_{target} and acceleration voltage U_{target} were guaranteed during the measurement, the value of $\Delta\Phi$ is tied to a relatively large uncertainty, which is difficult to measure. Hence, the first method is used here. However, both values for E_B match within their estimated errors.

Target length L_t. The length of the interaction region is estimated from the measured rate coefficient and collision energy profile in the toroid region.[4] In this simplified model the angular distribution of DR events is assumed to be isotropic, even at non-zero collision energies. Moreover, variations of the branching ratios with the collision energy are not considered. The uncertainties are reflected in a 10% error of this parameter.

Target center-detector distance L. The distance between the target center and the detector has been precisely determined. As the guiding field of the electron beam in the toroids can be modified by steerers, however the center of the effective target length can change within approximately ± 1 cm.

Spot position spread $\sigma_{blurred}$. By fitting the simulated data, the image distortion in the pixel-to-meter calibration is found to have a negligible effect on the KER and cannot be misinterpreted as a blurring of the fragment positions on the MCP, described by $\sigma_{blurred}$. This parameter, in turn, appears to be highly non-linear in its effects of ΔE_{KER} and $T_{e,\perp}$. The strong inverse-correlation between $\sigma_{blurred}$ and $T_{e,\perp}$ could explain such an effect. As these two parameters cannot be fitted at the same time, $\sigma_{blurred}$ is fixed to 30 μm based on the MCP channel diameter. The assumed

[4] O. Novotný, private communications

Table 5.5 Systematic error balance for ΔE_{KER} and $k_B T_{e,\perp}$ in [meV].

			Systematic errors of	
Parameter	Value	α_t	ΔE_{KER}	$k_B T_{e,\perp}$
E_B	4.657 ± 0.025 MeV	20	± 0.02	± 0.02
		40	± 0.016	± 0.02
L_t	1.134 ± 0.1 m	20	± 0.03	± 0.12
		40	± 0.035	± 0.1
L	12.24 ± 0.01 m	20	± 0.01	± 0.002
		40	± 0.013	± 0.04
$\sigma_{blurred}$	$30 \pm 15\,\mu$m	20	± 0.008	± 0.03
		40	± 0.003	± 0.01
$k_B T_{e,\parallel}$	$50 \pm 20\,\mu$ eV	20	± 0.015	± 0.008
		40	± 0.015	± 0.011
total		20	± 0.04	± 0.13
		40	± 0.04	± 0.10

uncertainty of $\pm 50\%$ coincides with the observed difference between the simulated value and the value resulting from fitting the simulated data.

Longitudinal electron temperature $T_{e,\parallel}$. A typical value measured for the longitudinal temperature is $k_B T_{e,\parallel} \approx 50\,\mu$eV [Kra09]. As it is smaller than the transversal temperature by almost two orders of magnitude, it has less influence on the measurement. This value was obtained from dielectronic recombination measurements of much faster atomic ions and therefore at higher acceleration voltage, which is responsible for the reduction of $T_{e,\parallel}$ compared to the initial temperature of the electron beam. However, theory has shown that, at acceleration voltages above approximately 100 V, $k_B T_{e,\parallel}$ is almost independent of U_{target}, but mainly determined by plasma-relaxation effects which depend solely on the current density [Dik88]. In contrast, the theoretically predicted value for $k_B T_{e,\parallel}$ is approximately $30\,\mu$eV. Hence, the value of $k_B T_{e,\parallel} = 50\,\mu$eV is adopted with an uncertainty of $\pm 40\,\%$.

In the fitting procedure, these systematic parameters are fixed to the values listed in tab. 5.5, while the amplitudes of the various initial channels as well as $T_{e,\perp}$ and

E_{KER} are the free statistical parameters of the fit. The remaining number of free parameters still makes the fit ambiguous. In particular the initial channel amplitudes are strongly correlated with each other. Depending on the chosen starting parameters, side minima of χ^2 are sometimes found in the fitting routine. Therefore, the statistical errors on ΔE_{KER} and $T_{e,\perp}$ obtained from the fit are double-checked by investigating the χ^2 behavior close to its minimum. For various fixed values of the parameter of interest, ΔE_{KER} or $T_{e,\perp}$, the respective other one is fitted together with the dissociation channel amplitudes while recording the best-fit value of χ^2. As all parameters apart from the parameter of interest are set free during this fit, the $1\,\sigma$ uncertainty interval corresponds to the projection of the $\Delta\chi^2 = 1.0$ boundary onto the parameter axis [Nak10]. The two distributions acquired at $\alpha_t = 20$ and $\alpha_t = 40$ are analyzed separately, yielding the statistical errors $\Delta E^{stat}_{KER,20} = 0.03\,\text{meV}$, $k_B \Delta T^{stat}_{e,\perp,20} = 0.07\,\text{meV}$ and $\Delta E^{stat}_{KER,40} = 0.05\,\text{meV}$, $k_B \Delta T^{stat}_{e,\perp,40} = 0.06\,\text{meV}$, which appear to be slightly smaller than the errors returned from the `MINUIT` fitting procedure. It should be noted that inter-fragment transversal distances below 0.8 mm are not fitted. The assumption of a Gaussian smoothing of the projected distance distribution is not valid for distances comparable to σ_{blurr}. In fact, simulations have shown that for such low distances the blurring is asymmetric and makes the distances appear larger on average.

A similar procedure is used to study the systematic uncertainties of ΔE_{KER} and $T_{e,\perp}$. Each parameter listed in tab. 5.5 is varied within its uncertainty range while fitting the amplitudes, ΔE_{KER} and $T_{e,\perp}$ and keeping all other systematic parameters fixed at their mean values. The obtained results are included in tab. 5.5. The overall systematic error ΔE^{sys} is obtained by

$$\Delta E^{sys} = \sqrt{\sum_i \left(\Delta E_i^{sys}\right)^2}, \tag{5.8}$$

where the index i stands for all systematic parameters, including the error of $\pm 0.009\,\text{meV}$ in the theoretically determined energy of the HF^+ rotational fine-structure levels (sec. 5.1.2).

Fitting the transversal distance distributions of H and F produced in the DR of HF^+ yields two values for the kinetic energy release offset $\Delta E_{\Delta KER}$, corresponding

to the two values of α_t used in the experiment,

$$\Delta E_{KER,20} = (19.98 \pm 0.03 \pm 0.04)\,\mathrm{meV} \tag{5.9}$$

$$\Delta E_{KER,40} = (19.86 \pm 0.05 \pm 0.04)\,\mathrm{meV} \tag{5.10}$$

and the transversal electron temperature $T_{e,\perp}$

$$k_B T_{e,\perp,20} = (1.84 \pm 0.07 \pm 0.13)\,\mathrm{meV} \tag{5.11}$$

$$k_B T_{e,\perp,40} = (1.25 \pm 0.06 \pm 0.10)\,\mathrm{meV}, \tag{5.12}$$

where the first error gives the statistical error and the second one the systematical error. The corresponding transversal distance distributions including the fits are illustrated in fig. 5.6 and fig. 5.7.

The two values $\Delta E_{KER,20}$ and $\Delta E_{KER,40}$ do not coincide within their uncertainties as would be expected. This could be caused by remaining shortcomings of the model on which the fitting procedure is based. This is supported by the difference in transversal electron temperature $T_{e,\perp}$ found between the two data sets. The measured ratio $T_{e,\perp,20}/T_{e,\perp,40} = 1.47$ differs from the theoretically expected ratio of $T_{e,\perp,20}/T_{e,\perp,40} \stackrel{!}{=} 40/20 = 2$ by more than 25 %. A possible reason for such an effect are derivations from the electron velocity distribution of the assumed Gaussian shape. Non-perfectly aligned beams, which could be caused by the various correction coils along the target, could give rise to a 'heating' effect and therefore a broader electron energy distribution. In addition, the assumption of a sharply limited overlap length in the target is simplified as it does not take the effect of changing collision energies E_d in the toroidal regions into account. In addition, the rate coefficient and the fragmentation anisotropy probably vary within the thermal collision energy distribution. As reported in [Dju01], the measured cross section also reveals resonant structures in addition to the overall $1/E_d$ decrease for near-zero collision energies. These are presumed to be caused by indirect processes and are not included in the fitting routine.

It is assumed, that the difference between the two results for different α_t approximately reflects this uncertainty. Therefore, the overall error on ΔE_{KER} is assumed to be in the order of the difference between the values given in eq. (5.9) and eq. (5.10).

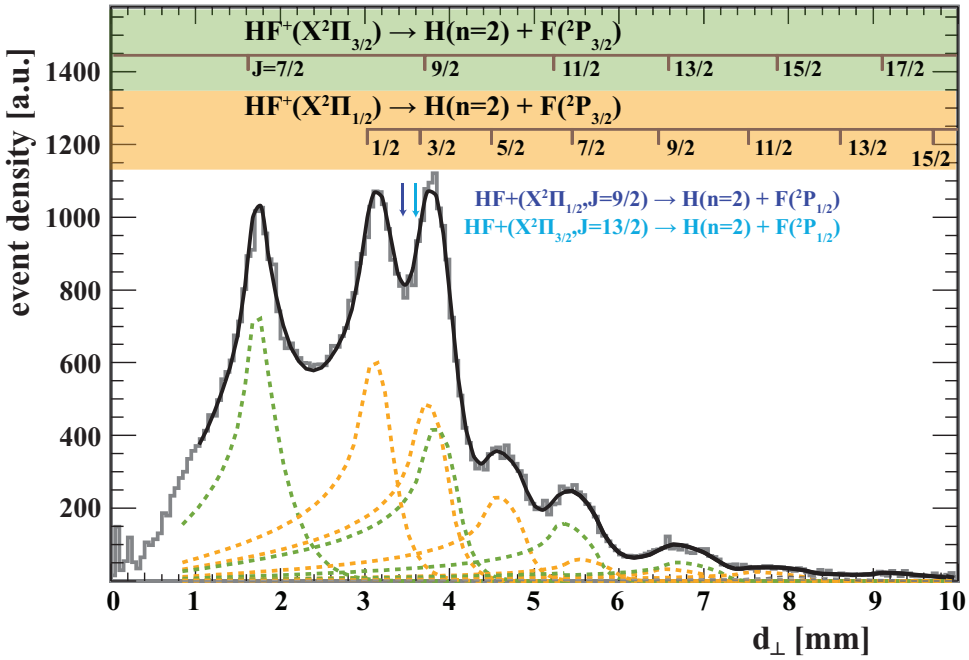

Figure 5.6 Transversal distance distribution of H and F produced in the DR of HF^+ (gray histrogram), acquired at $\alpha_t = 20$. The solid black line displays the sum of all fitted dissociation channels, the dashed green lines illustrate the contributions from the individual channels dissociating from $HF^+(X^2\Pi_{3/2})$ into the atomic final level $H(2s) + F(^2P_{3/2})$. The dashed orange lines, in contrast, display the dissociation channels starting in a $HF^+(X^2\Pi_{1/2})$ state. The theoretically predicted relative kinetic energy releases given in tab. 5.2 are indicated by the combs in the upper part of the frame. The blue arrows indicate the expected peak positions of the two lowest channels dissociating into the higher atomic final level $H(2s) + F(^2P_{1/2})$.

As there is no reason to favor the measurement at a certain α_t over the other, the final result on the KER offset is determined by the mean value to be

$$\Delta E_{KER} = (19.92 \pm 0.2)\,\text{meV}, \tag{5.13}$$

yielding an atomic final state $H(2s) + F(^2P_{3/2})$ that lies 19.92 meV above the $HF^+(X^2\Pi_{3/2}, J = 3/2)$ ground state (fig. 5.2).

In addition to the precise value for the kinetic energy released in the dissociation of the individual initial states, fitting the transversal distance distributions reveals another interesting fact. Apparently, at near-zero collision energy, no HF^+ states dissociate into the higher-lying atomic level $H(2s) + F(^2P_{1/2})$. Assuming the ions are in thermal equilibrium at 300 K, almost 10 % of the ions populate rota-

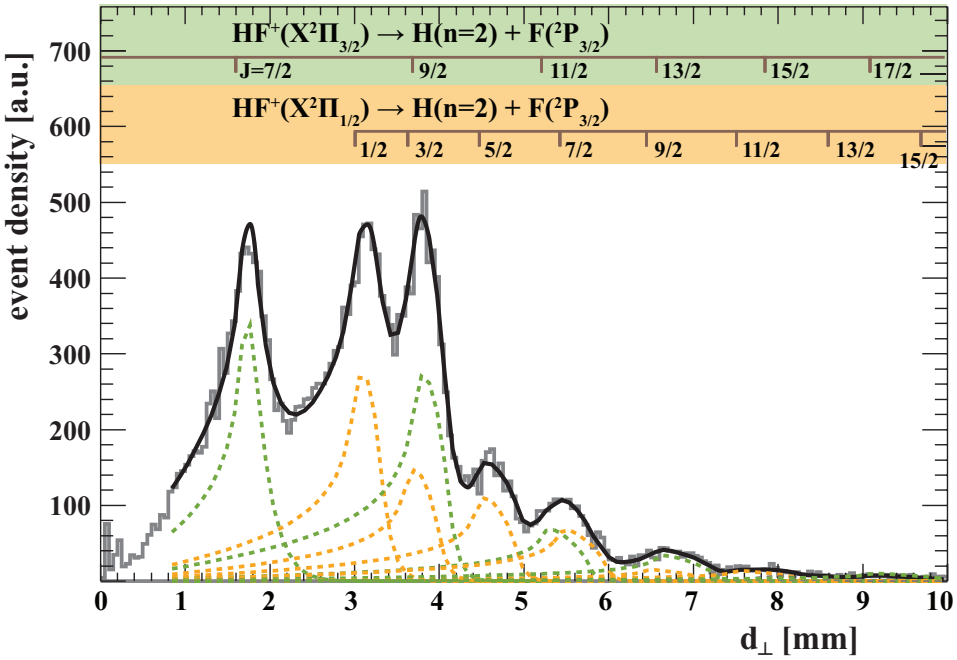

Figure 5.7 Transversal distance distribution of H and F produced in the DR of HF^+ (gray histrogram), acquired at $\alpha_t = 40$. Color code and labeling as in caption of fig. 5.6.

tional states that lie more than 70 meV above the ground state and would allow such a dissociation. The channels with the two lowest kinetic energy releases are $HF^+(^2\Pi_{1/2}, J = 9/2) \rightarrow H(2s) + F(^2P_{1/2}) + 17.52\,\text{meV}$ and $HF^+(^2\Pi_{3/2}, J = 13/2) \rightarrow H(2s) + F(^2P_{1/2}) + 20.54\,\text{meV}$, which would appear in the transverse distance distribution between the second and third peak (fig. 5.6, blue arrows). Including these states in the analysis would worsen the fit results. Especially the dip between these two adjacent peaks is much better reproduced by fitting the distribution without the contribution of any states dissociating into the higher final state.

This observation, however, seems to change for larger collision energies. Figure 5.8 illustrates the projected distance distribution measured at $E_d = 140\,\text{meV}$ collision energy. The contributing dissociation channels are indicated in the upper part of the figure and illustrate clearly the main contribution of ionic states dissociating into the $H(2s)$+$F(^2P_{1/2})$ state.

5.4.2 Dissociation energy of HF^+

As mentioned at the beginning of this chapter, a minimum value for $D^0_{HF^+}$ was reported in 1970. In [Bru70], the dissociation energy $D^0_{HF^+}$ has been estimated

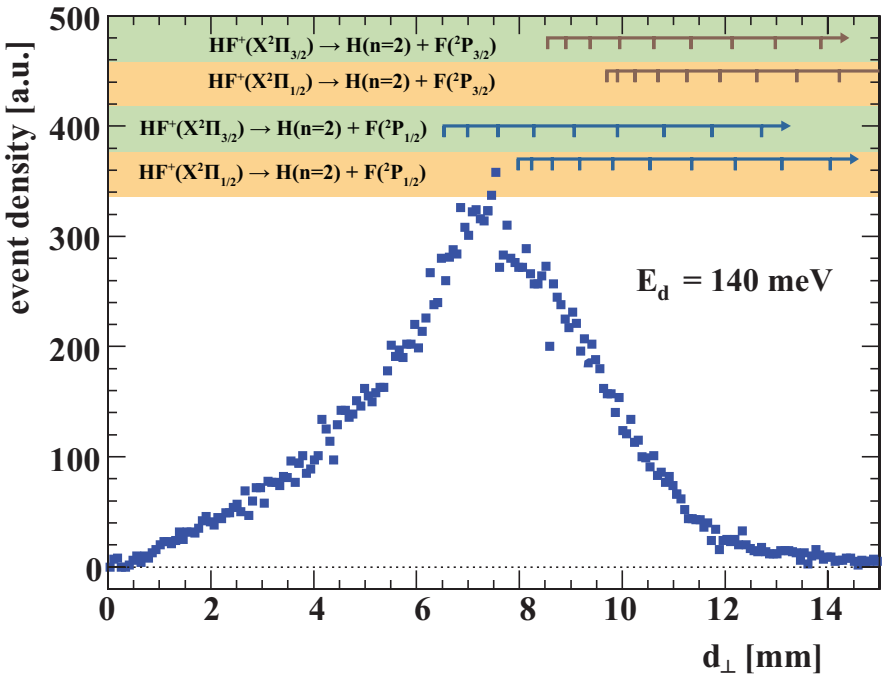

Figure 5.8 Transverse distance distribution of H and F produced in the DR of HF^+ at $E_d = 140\,\text{eV}$ collision energy. The expected peak positions of the individual dissociation channels are indicated in the upper part of the figure. The fact that the measured data peaks at $d_\perp \approx 7\,\text{mm}$ indicates that dissociations into the $H(2s)$+$F(^2P_{1/2})$ state dominate at $E_d = 140\,\text{meV}$.

to be $D^0_{HF^+} > 3.41(5)\,\text{eV}$. Five years later, a value of $D^0_{HF^+}$ =3.4202(62) meV was reported [Gew75]. A more precise value can be calculated from a combination of later optical spectroscopy results, listed in tab. 5.3:

$$D^0_{HF^+} = D^0_{IP,HF} - \mathcal{E}_{EA,F} - E_{I,HF} = 3.41788(16)\,\text{eV}. \tag{5.14}$$

Alternatively, the dissociation energy can be calculated from the results for ΔE_{KER} of the presented experiment. This result can be used to determine $D^0_{HF^+}$ via

$$D^0_{HF^+} = \Delta E_{KER} - E_{E,H(1\to2)} + E_{I,H} = 3.41953(20)\,\text{eV}, \tag{5.15}$$

Clearly, the result for ΔE_{KER} is most sensitive to the position of the signal component for the dissociation $HF^+(^2\Pi_{3/2}, J = 7/2) \to H(2s) + F(^2P_{3/2})$, that appears at the lowest KER. As the errors of $E_{E,H(1\to2)}$ and E_I, H are below 10^{-3} meV, the determination is very direct and the uncertainty of E_{KER} determines the overall

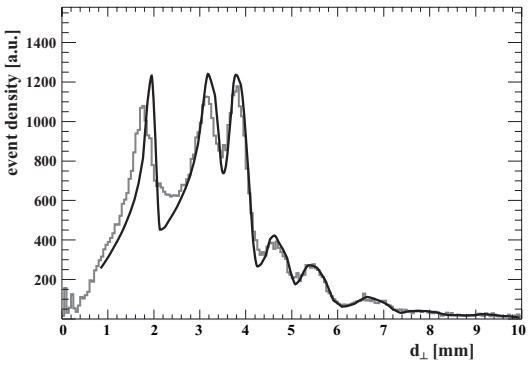

Figure 5.9 Transverse distance distribution as presented in fig. 5.6, but fitted with a fixed $\Delta E_{\Delta KER} = 3.734\,\text{meV}$ that corresponds to $D^0_{\text{HF}^+} = 3.41788(16)\,\text{eV}$ obtained from the combination of optical spectroscopy results given in eq. (5.14).

error of $D^0_{HF^+}$.

The discrepancy of the two independently obtained values of $D^0_{HF^+}$ given in eq. (5.14) and eq. (5.15) of more than 1.6 meV is by far not covered by the estimated uncertainties. The detailed analysis of the contributing uncertainties in the fitting procedure does not approve a for larger uncertainty estimation. This can also be illustrated by fitting the transverse momentum spectrum with a fixed KER offset value of $\Delta E_{KER} = 18.26\,\text{meV}$, corresponding to the value $D^0_{\text{HF}^+} = 3.41788(16)\,\text{eV}$ obtained from optical spectroscopy (eq. (5.14)). In order to reproduce the transverse distance data, the routine converges in this case to a fit based on a completely unrealistic transverse electron temperature of $k_B T_{e,\perp} = 1.4 \cdot 10^{-2}\,\text{meV}$. Even then, the peak positions for small KER, where the momentum distribution is most sensitive to changes in the dissociation energy, are not reproduced. A different explanation for the 'missing' KER measured in a merged-beams experiment might be based on electron capture in a time-dependent saddle-point potential created by the motion of the ion through the toroidal regions of the electron target [Hör06]. However, this would imply a capture solely into a state 1.62 meV below the continuum which seems unlikely for a non-resonant process. In case of the electrons captured into multiple states reaching up to the continuum, the observed peaks in the momentum spectrum would appear to be much broader.

In summary, imaging of the HF^+ DR fragments offers the opportunity of determining the molecular dissociation energy $D^0_{\text{HF}^+}$ with sub-meV precision in a much more direct way than this could be done previously. The present method benefits from the fact that only two additional quantities, the very precisely known ionization and excitation energies of hydrogen $E_{I,\text{H}}$, are needed from other sources. In contrast, the determination presented in eq. (5.14) is more indirect, as results from different

experiments in which large energy intervals are measured, need to be combined.

5.4.3 Dissociation energy of DF^+

The transverse distance distribution of D and F produced in the DR of DF^+ is displayed in fig. 5.10. As expected from the level calculations in sec. 5.2, the fraction of dissociation events into the $D(2s) + F(^2P)$ atomic state is reduced compared to those into the $D(1s) + F(^2P)$, so that the contribution from the latter channel becomes relatively more pronounced. In fact, less than 10% of the thermalized ions populate the states $DF^+(X^2\Pi_{3/2}, J > 17/2)$ and $DF^+(X^2\Pi_{1/2}, J > 11/2)$, which lie above the dissociation threshold $D(2s) + F(^2P_{3/2})$ (illustrated in fig. 5.2). The fitting procedure in this case is applied to the transverse distance distribution with $k_B T_{e,\perp}$ fixed to 1.84 meV (the value obtained from analyzing the HF^+ data). According to the level prediction of tab. 5.2 and the predicted ΔE_{KER} for the DF^+ ground state from eq. (5.7), the $DF^+(X^2\Pi_{1/2}, J = 11/2)$ state is expected to be the one with the lowest kinetic energy released during dissociation into the $D(2s) + F(^2P_{3/2})$ state, amounting to 3.9(10) meV. However, the fitting analysis yields a KER which is by 1.03 meV smaller than the expected one (2.86 meV). As a consequence, the kinetic energy released in the dissociation of $DF^+(X^2\Pi_{1/2}, J = 11/2)$ is so small, that the corresponding transverse distance peak is only party visible due to the limited detector resolution. The first completely visible peak originates from the DR of $DF^+(X^2\Pi_{3/2}, J = 17/2)$, with a measured KER of E_{KER}=10.74 meV (expected $E_{KER} = 11.77$ meV), which is approximately 2.5 times higher than the KER of the lowest open dissociation channel in the spectrum of HF^+ and therefore less precisely measured from the distance distribution. Even though the most sensitive peak of the DR of $DF^+(X^2\Pi_{1/2}, J = 11/2)$ is only partly visible, the subsequent peaks, produced by single molecular dissociation channels, are narrow and thus allow for a precise KER fitting. In addition, the energy differences between the first three visible rotational levels are tested to be unique in the rotational fine-structure pattern of ground state of DF^+, so that a correct assignment of the peaks can be assured. The overall uncertainty of ΔE_{KER} resulting from the fit is estimated to be the same as in the analysis of the HF^+ momentum distribution.

Thus, with the measured $\Delta E_{KER} = 72.33(20)$ meV, the dissociation energy of

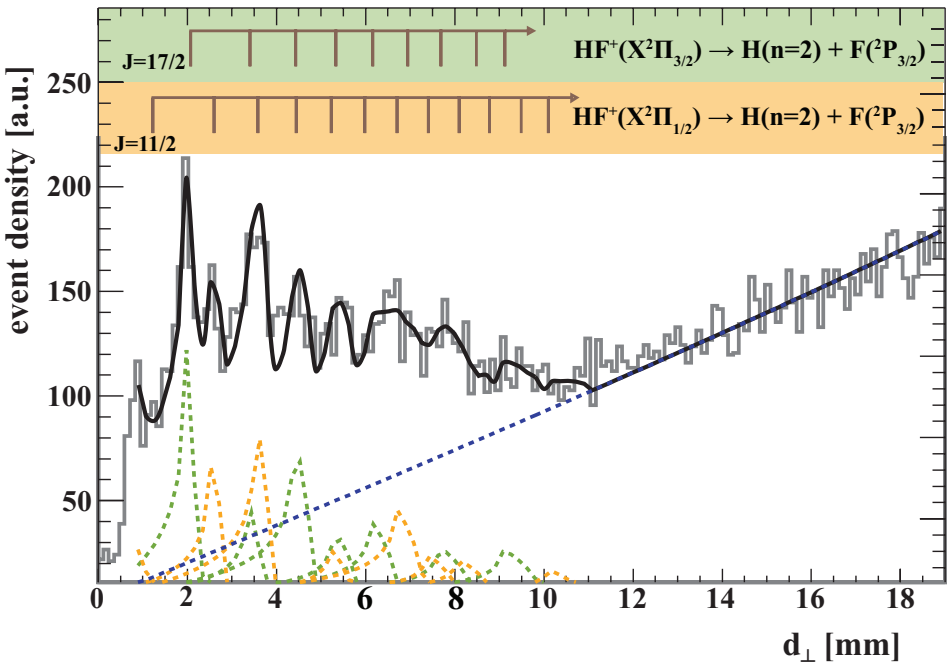

Figure 5.10 Transverse distance distribution of D and F produced in the DR of DF^+. Color code and labeling as in caption of fig. 5.6. The dashed blue line indicates the contribution of dissociations into the atomic final level $H(1s) + F(^2P)$.

DF^+ can then be calculated as

$$D^0_{DF^+} = \Delta E_{KER} - E_{E,\mathrm{D}(1\to 2)} + E_{I,\mathrm{D}} = 3.47287(20)\,\mathrm{eV}. \tag{5.16}$$

As for HF^+, the dissociation energy can also be calculated from spectroscopically obtained constants according to eq. (5.14), replacing the HF ion pair formation threshold $D^0_{IP,\mathrm{HF}}$ and the HF ionization energy $E_{I,\mathrm{HF}}$ by the corresponding values for DF, given in tab. 5.3:

$$D^0_{DF^+} = D^0_{IP,\mathrm{DF}} - \mathcal{E}_{EA,\mathrm{F}} - E_{I,\mathrm{DF}} = 3.472(1)\,\mathrm{eV}. \tag{5.17}$$

which is in excellent agreement with eq. (5.16). However, it should be mentioned that the DF spectroscopic data are less precise compared to HF.

Born-Oppenheimer breakdown in the electronic ground states of the isotopes HF^+ and DF^+

As described in the previous section, DR measurements of the isotopes HF^+ and DF^+ allow the determination of the dissociation energies D^0 of both ions. These energies differ by

$$\Delta D^0 = D^0_{DF^+} - D^0_{HF^+} = 53.34(30)\,\text{meV}. \tag{5.18}$$

In the Born-Oppenheimer approximation, the dissociation energies should differ only by the difference in zero point energies of $\Delta G(0) = 51.59(17)\,\text{meV}$ (eq. (5.5)). However, the observed difference is slightly larger. This is likely to reflect the non-Born-Oppenheimer correction to the adiabtic energy levels, for which a value of $\Delta D_e = \Delta D^0 - \Delta G(0) = 1.75(35)\,\text{meV}$ is determined. For the neutral molecules HF and DF a difference between their classical bond dissociation energies of $\Delta D_e = 1.549\,(62)\,\text{meV}$ has been measured, from which an experimental estimate of the Born-Oppenheimer breakdown in the ground electronic state is provided [Hu06].

The present result suggests that the precision of the fragmentation energy measurement is sufficient to detect a similar shift for the ions HF^+ and DF^+. They can be interpreted as a shift of the DF^+ classical bond potential minimum by 1.75 meV with respect to that of HF^+. The occurrence of a shift towards lower energies is in agreement with the effective potential energy for isotopes when Born-Oppenheimer breakdown is taken into account [Wat80, Hu06]:

$$U_{HF^+/DF^+}(R) = U_{BO}(R) + \frac{m_e u_{H/D}(R)}{M_{H/D}} + \frac{m_e u_F(R)}{M_F}, \tag{5.19}$$

where $U_{BO}(R)$ is the Born-Oppenheimer potential function and $m_e u(R)/M$ are the correction terms which are mass dependent. The advantage of this isotopic comparison is that the dissociation energy of both ions has been determined by the same method. By subtracting the obtained values for D^0 from each other, possible systematical effects, as for example the binding of very high Rydberg electrons in the toroidal regions of the target, are most likely to cancel out. However, the calculation of the zero-point energies relies on molecular constants derived from threshold photoelectron spectroscopy (tab. 5.3) and therefore reveal a relatively large uncertainty. Spectroscopic data of higher precision, preferentially from optical spectroscopy, are

necessary to verify the proposed Born-Oppenheimer breakdown in the electronic ground states of the isotopes HF^+ and DF^+.

Chapter 6

Dissociation Pathways in the Dissociative Recombination of D_3O^+

Due to its high relevance in the oxygen chemistry of water in the interstellar medium (ISM), the hydronium ion (H_3O^+) is one of the most studied polyatomic species with respect to dissociative recombination [Lar08]. In addition, it plays a decisive role in many other fields ranging from fundamental quantum chemistry over applications in the chemistry of acid-base and redox equilibria [But96] to the chemistry of atmospheric ion clusters [Wit08].

In this chapter, DR experiments on the deuterated species D_3O^+ are presented, with a focus on the dissociation into the three fragments $OD + D + D$. The experimental results combined with theoretical calculations of the involved potential energy surfaces allow for a better understanding of the DR dissociation mechanism.

6.1 On the polyatomic ion D_3O^+

The existence of the hydronium ion (H_3O^+) was first postulated at the beginning of the 20^{th} century in a theoretical study concerning ester formation [Gol07]. Since then, it has been the subject of wide interest, both experimentally and theoretically. A short summary of the activities on D_3O^+ and the corresponding reactions are outlined in the following section.

6.1.1 H_3O^+ properties and interactions

Collision experiment research of H_3O^+ in the first half of the 20$^{\text{th}}$ century were mainly dedicated to flame studies, where H_3O^+ was found to be the principal ion formed in the combustion of hydrocarbon gases. Experiments have been focusing on the loss rate of these ions by electron recombination and its temperature dependence [But96]. The overall process controlling the concentration of H_3O^+ was found to be $H + H + OH \rightleftharpoons H_3O^+ + e^-$. This reaction was proposed to proceed via the formation of an excited water molecule $H + OH \rightleftharpoons H_2O^*$ that would further interact with an atomic hydrogen leading to hydronium via $H + H_2O^* \rightleftharpoons H_3O^+ + e^-$ [Kne60].

The abundance of H_2O in the ISM is of great interest. Not only is water a prerequisite for life, it is also an important coolant in interstellar cloud collapse and thus contributes to the star formation rate [Neu95]. Ground-based direct detection of interstellar water is difficult due to the atmospheric water concentration. This problem was addressed by the more viable approach of indirectly establishing the interstellar concentration of H_2O. The spectral emissions related to the intramolecular dynamics of the inversion (umbrella) motion[1] of H_3O^+ [Woo91] were used as an indicator for the water abundance. In 1983 the hydronium ion was observed in the ISM for the first time [Woo86]. The production of hydronium in dense clouds is initiated through $H_3{}^+$ [Wil96]:

$$\begin{aligned} H_3^+ + O &\rightarrow OH^+ + H_2 \\ OH^+ + H_2 &\rightarrow H_2O^+ + H \\ H_2O^+ + H_2 &\rightarrow H_3O^+ + H \end{aligned} \tag{6.1}$$

The major destruction mechanisms are *proton transfer* to species (denoted as LPA) having *large proton affinities*

$$H_3O^+ + \text{LPA} \rightarrow H(\text{LPA})^+ + H_2O \tag{6.2}$$

[1] Vibrational modes are discussed at the end of this paragraph.

and dissociative recombination with low-energy electrons[2]:

$$\begin{aligned} H_3O^+ + e^- &\rightarrow H + H_2O + (E^0_{KER})^{(\alpha)} \\ &\rightarrow OH + H_2 + (E^0_{KER})^{(\beta)} \\ &\rightarrow OH + H + H + (E^0_{KER})^{(\gamma)} \\ &\rightarrow O + H_2 + H + (E^0_{KER})^{(\delta)}. \end{aligned} \tag{6.3}$$

The branching ratios of the different fragmentation channels in eq. (6.3) are critical parameters in models of interstellar molecular synthesis. If H_2O is the main DR product it is also the dominant oxygen-containing molecule, whereas if the DR primarily leads to the formation of OH, the main oxygen-containing species will be O_2 [Mil88]. This increased interest in branching ratios of the hydronium DR was reflected by flowing afterglow [Her90] and merged-beams experiments. In 1996 water synthesis from the DR of H_3O^+ was observed for the first time at the ASTRID storage ring [And96]. While satisfying results for the absolute rate coefficient have been obtained from many experiments using different techniques [Mul83], further studies on the branching ratios [VC97, Jen00, Nev07, Nov10] revealed only partial agreement. Also theoretical attempts to predict the branching ratios yielded contradictory results [Bat91, Her78], depending on the identification of appropriate crossings of the potential curves for the polyatomic molecular ion and the repulsive potential energy curves of the products.

Since the late 1990s, theoretical product branching ratios have also been obtained from *ab initio* calculations of the DR of H_3O^+ [Ket99, Kay06, Tac00]. In [Ket99] the structures and relative energies of the initial ion and its DR products including their branching ratios have been calculated. From a comparison with the experimental results [VC97, And96] it was proposed that, even though the reaction leading to the products $H_2O + H$ is the most exothermic one, this decay does not constitute the product channel of the largest branching ratio. Rather, in the presence of sufficient excess internal energy, a large fraction of water molecules might undergo further dissociation to OH + H. The so far most ambitious effort to calculate product branching ratios is reported in [Kay06], where surface hopping in regions of two potential surfaces being close was included in the *ab initio* directly calculated trajectories. For a more detailed overview of the research on H_3O^+ DR see [Lar08]

[2]The energy release $(E^0_{KER})^{(i)}$ of this exothermic reaction is discussed in the next paragraph.

and references therein.

Hydronium is a stable ion with pyramidal C_{3v} equilibrium geometry. In its $X\,^1A_1$ ground state, the O-H distance was found to be $r_e = 0.9758\,\text{Å}$ with an angle of $\alpha_e = 111.3°$ between any pair of bonds [Sea85]. The potential function of hydronium reveals a low barrier to inversion of only 83 meV [Sea85], for which reason the planar symmetry (D_{3h}) is the relevant equilibrium for most of the levels [Luo99]. Due to its symmetry it has four normal modes: the symmetric stretch (breathing) mode $v^{(1)}$, the symmetric bend (umbrella) mode $v^{(2)}$, and two asymmetric stretch modes $v^{(3)}$ and $v^{(4)}$, each doubly degenerate. The vibrational frequencies are given in table A.1 of the appendix. H_3O^+ is isoelectronic with ammonia, NH_3, i.e. it features a closed electronic shell, which makes the direct DR impassable for low collision energies[3]. Therefore, the DR of H_3O^+ is believed to proceed via the indirect mechanism. In particular, Jahn-Teller coupling between the antisymmetric modes is expected to play an important role.

Finally, it should be mentioned that, even though it is H_3O^+ which is of astrophysical interest, the DR measurement presented here has been performed with its fully deuterated analog D_3O^+ for experimental reasons. The cone size of the dissociating fragments in the water producing channel with a maximum kinetic energy release (KER) of more than 6 eV (see the following section) would have been too large to be fully detected by the imaging detectors due to the lighter masses of the hydrogen atoms. In addition, mass separation with the EMU detector would have been far more difficult in the case of H_3O^+.

6.1.2 Dissociative recombination of D_3O^+: energy considerations

As noted, the DR of D_3O^+ with low-energy electrons is an exothermic reaction that leads to four final channels, corresponding to those given in eq. (6.3) for H_3O^+. The energies $(E^0_{KER})^{(i)}$, which are released during the reaction, reflect the change in binding energy during the transition from the initial to the final state. Figure 6.1 illustrates the energies released for the different dissociation channels accessible at near-zero collision energy. The energy release $(E^0_{KER})^{(\alpha)}$ in the heavy-water producing two-body channel can be calculated from the deuterium affinity of water $E_{D_3O^+ \to D_2O + D^+} = 7.24\,\text{eV}$ [Cot73] and the ionization potential of deuterium

[3] V. Kokoouline, private communications

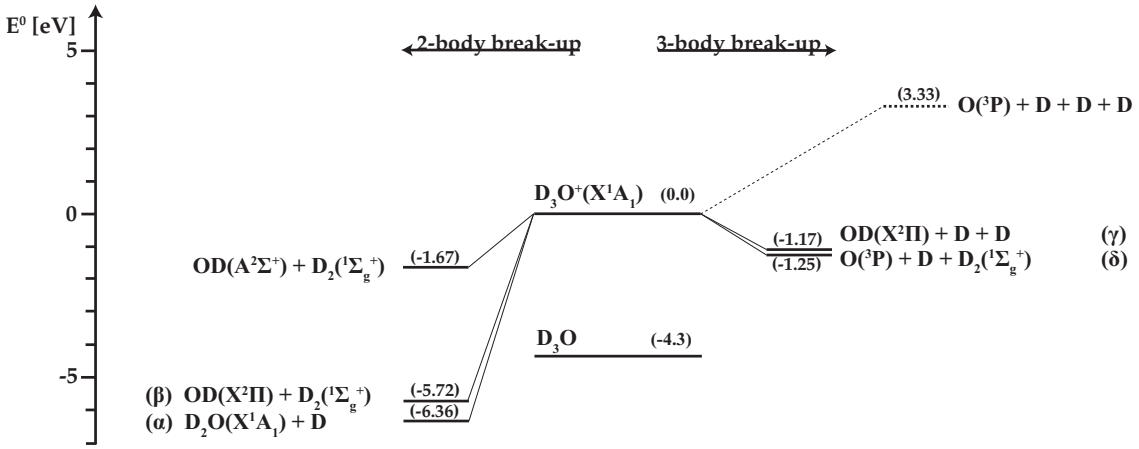

Figure 6.1 Level diagram of the DR decay channels of D_3O^+ accessible at near zero collision energy. The two-body break-up is displayed on the left, the three-body break-up on the right. Even though not accessible at collisions with cold electrons, the dashed line indicates the dissociation into the four-body channel. The labels (α), (β), (γ), (δ) correspond to the labeling in eq. (6.3), where the energy difference between the ground state D_3O^+ and these ground state product channels is given as $(E^0_{KER})^{(i)}$.

$E_{I,\mathrm{D}} = 13.60\,\mathrm{eV}$ [Kel87]:

$$(E^0_{KER})^{(\alpha)} = -\left(E_{\mathrm{D_3O^+\to D_2O+D^+}} - E_{I,\mathrm{D}}\right) = 6.36\,\mathrm{eV} \tag{6.4}$$

In the three-body channels, the energy release is reduced by the various binding energies of water, $D^0_{\mathrm{D_2O\to OD+D}} = 5.19\,\mathrm{eV}$ [Har01], and $D^0_{\mathrm{D_2O\to O+D_2}}$, which is obtained from the binding energies of OD and D_2, given by $D^0_{\mathrm{OD}} = 4.47\,\mathrm{eV}$ and $D^0_{\mathrm{D_2}} = 4.55\,\mathrm{eV}$, respectively [Eyl93]:

$$(E^0_{KER})^{(\gamma)} = -\left(E_{\mathrm{D_3O^+\to D_2O+D^+}} - E_{I,\mathrm{D}} + D^0_{\mathrm{D_2O\to OD+D}}\right) = 1.17\,\mathrm{eV} \tag{6.5}$$

$$(E^0_{KER})^{(\delta)} = -\left(E_{\mathrm{D_3O^+\to D_2O+D^+}} - E_{I,\mathrm{D}} + D^0_{\mathrm{D_2O\to OD+D}} + D^0_{\mathrm{OD}} - D^0_{\mathrm{D_2}}\right) = 1.25\,\mathrm{eV} \tag{6.6}$$

By subtracting the binding energy of OD, D^0_{OD}, from the latter value, the energy released in the second two-body channel, $(E^0_{KER})^{(\beta)}$, can be calculated:

$$(E^0_{KER})^{(\beta)} = -\left(E_{\mathrm{D_3O^+\to D_2O+D^+}} - E_{I,\mathrm{D}} + D^0_{\mathrm{D_2O\to OD+D}} - D^0_{\mathrm{D_2}}\right) = 5.72\,\mathrm{eV} \tag{6.7}$$

Energy conservation demands a transformation of the released energy E^0_{KER}, originally stored in the chemical bonds, into energy of the system's other degrees of

freedom. A general energy balance is given by

$$E^0_{KER} = \underbrace{(E_{KER} + E^f_{el} + E^f_{vib} + E^f_{rot})}_{\text{product energies}} - \underbrace{(E_e + E^i_{el} + E^i_{vib} + E^i_{rot})}_{\text{reactant energies}}, \tag{6.8}$$

with E_{KER} being the total kinetic energy released in the break-up. As mentioned in sec. 3.3, the KER is an important quantity of the reaction, addressed by fragment imaging experiments. Any electronic excitations of the products are combined in E^f_{el}. All product deuterium atoms in the reactions given in eq. (6.3) are produced in their electronic ground state with principal quantum number $n = 1$. The large energy amount of almost 10 eV, which is necessary for a transition into the lowest excited state $n = 2$, inhibits such an excitation. The same holds for the oxygen atom – here as well, the excitation energy of more than 9 eV into the $n = 3$-state [Ral10] is too high to be overcome by the energy released in the dissociation process. The OD molecule is the only product who's lowest electronic excited state $OD(A^2\Sigma)$ can be accessed by the energy available (fig. 6.1). Furthermore, all molecular fragments can carry away some of the released energy in terms of vibrational (E^f_{vib}) and rotational (E^f_{rot}) excitation.

The second term in eq. (6.8) denotes the energy in the system prior to the reaction. E_e indicates the collision energy between the hydronium and the free electron. In the following, experiments with a velocity-matched cold electron beam are presented. In this case, E_e is determined by the electron temperature of approximately $1.0\,\mathrm{meV}/k_B$ in the cm frame of the beams and can essentially be neglected compared to the other energies. The remaining variables, E^i_{el}, E^i_{vib} and E^i_{rot}, denote the energy stored in the parent ion as electronic, vibrational and rotational excitations, respectively. As the first exited state $D_3O^+(^1A''_2)$ lies 11.3 eV above the ground state $D_3O^+(X^1A_1)$ [Kle96], an electronic excitation can be excluded. However, excitations of rotational and vibrational states are possible. Rough estimations on the lifetimes of vibrationally and rotationally excited states of D_3O^+ can be found in appendix A.2. The lifetimes of vibrational excitations have been determined to be in the millisecond range. In the experiment discussed here data are acquired only after several seconds of storage time and thus, the probability of finding vibrationally excited states is vanishing. However, the molecular ions are likely to be produced in the ion source in rotationally excited states. Since transitions to lower J states are suppressed due to the $\Delta K = 0$

selection rule for dipole radiation of non-planar symmetric top molecules (eq. (3.39) in [Tow55]), considerable rotational excitation of the parent ion cannot be ruled out. That the lifetimes of several rotational excitations are longer than the typical experimental storage times is supported by calculations of Sergei Yurchenko and Per Jensen, motivated through this work.[4]

Taking these considerations into account, eq. (6.8) reduces to

$$E_{KER} = E^0_{KER} + E_e + E^i_{rot} - E^f_{el} - E^f_{vib} - E^f_{rot}. \tag{6.9}$$

As the total energy release E^0_{KER} and the collision energy E_e are known, information on the rotational excitation E^i_{rot} of the stored D_3O^+ ions as well as on the overall excitation energy $E^f_{el} + E^f_{vib} + E^f_{rot}$ of the molecular fragments can be obtained by measuring the kinetic energy release E_{KER} of the different break-up channels.

The experimental results presented in the following focus on 3D fragmentation patterns and KER measurements of the symmetric three-body dissociation channel $D_3O^+ \rightarrow OD + D + D$. In addition, for a complete picture on the DR of D_3O^+ with cold electrons, results from the two-body channels, which were obtained using the EMU detector system, are shortly summarized.

6.2 Experimental setup and procedures

The experiments on the DR of D_3O^+ have been performed at the heavy ion storage ring TSR, which has been introduced in chap. 3. A Penning ion source was used to produce the D_3O^+ ions from a gas mixture of D_2O and D_2. The ions were accelerated to 2 MeV by a Van-de-Graaff accelerator and, after being injected into the storage ring, brought to a final energy of 4.23 MeV within 2.5 s by synchrotron acceleration.

For a single-charged cation of mass 22 u, this energy corresponds to a magnetic beam rigidity of 1.4 Tm, i.e. close to the maximum allowed by the bending field (sec. 3.1.2). As in the DR measurement of HF^+ presented earlier, the electron target was not only used for inducing electron-ion collisions but also served as the cooling medium for the ion beam.

After a phase-space cooling period of 7-10 s with an electron beam density of approximately $5 \cdot 10^6\,\mathrm{cm}^{-3}$, an ion beam diameter of less than 1 mm was achieved.

[4] University of Wuppertal, private communications

At this point the shutter that protects the detectors during the injection and synchrotron acceleration phase was removed, allowing the neutral fragments to reach either the EMU detector or alternatively, with the latter moved out of the beam path, the multi-hit optical gating detector at the end of the beamline. Throughout the entire measurement period, starting 10 s after injection and lasting until the beam was dumped after 20 s of storage time, the electron energy was not changed, i.e. the DR measurements presented in the following were performed at thermal collision energies of approximately 1 meV. During background measurements only, the beam velocities were detuned to a collision energy of 1 eV. The D_3O^+ DR cross section has a minimum at this energy [Jen00], which made it a suitable choice for obtaining the rate of charge-transfer collisions of the ions with the residual gas relative to the DR signal rate at near-zero collision energies. This ratio was found to be less than 0.1 %.

Imaging data were accumulated by repeating the procedure described above. Several 10^5 DR events were acquired using EMU. Considerably fewer events were obtained from the 3D multi-hit optical gating detector due to the lower acquisition rate and the limited measurement time of 20h – approximately $1.5 \cdot 10^5$ two-body and three-body events were recorded.

During the intensity calibration measurement the intensity thresholds of the two imaging detector cameras C_1 and C_2 (sec. 3.2.2) were set to 150 and 500, respectively. The latter threshold was changed to 50 during the actual DR measurement. Further, the edge length of the rectangular boxes defining the expected spot size in C_1 and C_2 were chosen to be 5 pixels and 17 pixels, respectively.

6.3 Experimental results

In the upcoming section, results obtained from the fragment imaging experiments described above are shown. Here, the presentation focuses on the full 3D imaging results regarding the three-body fragmentation channel OD + D + D, from which conclusions on the dissociation pathways can be drawn. There are two three-body channels open at near-zero collision energy (fig. 6.1) for which the individual fragment masses are too similar to be distinguished by the 3D multi-hit imaging detector (specifically 18 u, 2 u, 2 u for OD + D + D vs. 16 u, 4 u, 2 u for $O + D_2 + D$). However, branching ratio measurements with EMU [Nov10] clearly confirm a very low

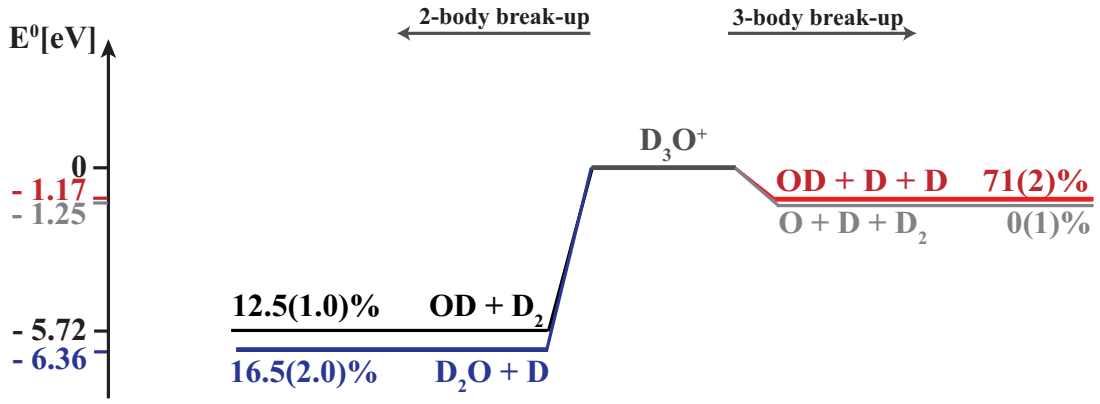

Figure 6.2 Level diagram and fragmentation branching ratios for the dissociative recombination of D_3O^+ at near zero collision energy [Nov10]. The errors are given in parentheses.

fragmentation into the $O + D + D_2$ channel (fig. 6.2). Therefore, 3D imaging results with the multi-hit optical gating detector can be directly interpreted as those of the channel $OD + D + D$. In contrast, this is not the case for the two-body channels $D_2O + D$ and $D_2 + OD$, with mass ratios also too similar to be reliably distinguished. Only EMU measurements make the distinction possible [Buh10b] and therefore provide complementary information on the DR process. These results for the two-body channels yield important conclusions about the dissociative dynamics induced by collisions with cold electrons, which are shortly summarized in the upcoming section.

6.3.1 2D imaging with EMU

As mentioned in sec. 3.2.1, analysis of the pulse heights from individual strips of the EMU detector directly yields the branching into the open dissociation channels (eq. (6.3), fig. 6.2). Further, the cm position is determined, from which the mass-weighted squared projected distance D^2 (eq. (3.6)) and the transversal kinetic energy release $E_\perp$ (eq. (3.7), fig. 6.5) are obtained for each production channel. The 3D KER distribution is then reconstructed from the measured D^2 distributions by fitting the latter by a sum $\sum_j \alpha_j \tilde{P}(D^2, (E_{KER})_j)$, as described in sec. 4.4. The derived kinetic energy release histograms for the three production channels at near-zero collision energy are shown in fig. 6.3.

As indicated in fig. 6.2, the expected kinetic energy release in the two-body channel

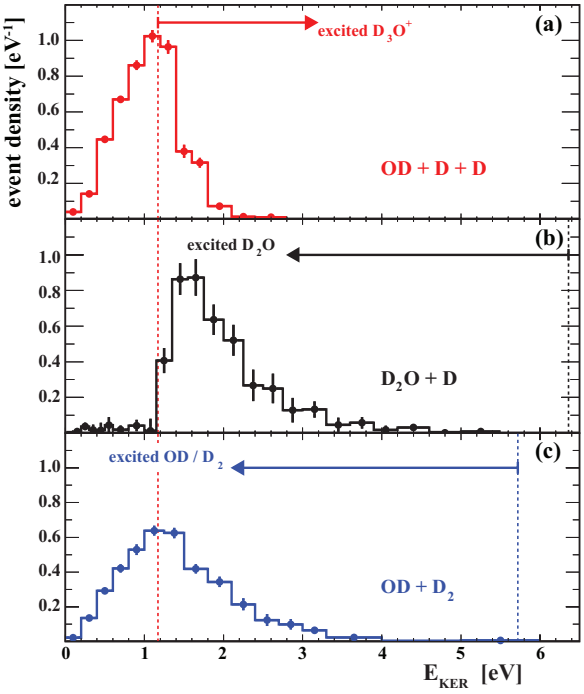

Figure 6.3 Normalized kinetic energy release histograms derived from EMU measurements of the D^2 distributions of (a) the OD + D + D fragmentation channel, (b) the D_2O + D channel, (c) the OD + D_2 channel. The dashed lines mark the energy released in the corresponding break-up (fig. 6.2), assuming no internal excitation in neither the parent ion nor the dissociation fragments [Buh10b].

$D_2O + D$ for ground-state educts and products is $(E^0_{KER})^{(\alpha)} = E_{D_2O,D} = 6.36\,eV$. However, the KER histogram in fig. 6.3 (b) shows no DR events in which more than 60 % of the available energy is converted to kinetic energy. In fact, more than 90 % of all events in this channel occur with KER deficiencies of more than 3 eV compared to $E_{D_2O,D}$. Furthermore, a remarkable sharp cutoff in the E_{KER} distribution of this channel can be noted at $(E^0_{KER})^{(\gamma)} = E_{OD,D,D}$, i.e. the KER below which no events of the water producing channel are detected coincides with the dissociation energy of D_2O.

These findings suggest a high internal excitation of the water molecules occurring in the two-body channel. As explained in sec. 6.1.2, any energy missing in the KER of a dissociation must be stored in the internal degrees of freedom of the fragments. KER deficiencies of more than 3 eV suggest that the excitation of the water molecules is predominantly vibrational, as the lowest electronically excited state of water lies more than 7 eV above the ground state [Rub08] and rotational excitation of several eV would require the existence of an enormous amount of angular momentum in the D_2O molecule, much higher than initially found in the D_3O^+ molecule. (It corresponds to a rotational energy not exceeding ~ 1 eV as discussed in sec. 6.3.2).

In the initial phase of DR, high Rydberg states of the D_3O radical are likely to be formed. The possibility of radiative emission from these states causing the lack

of KER is discussed in [Buh10b]. Even though the lowest state of the D_3O radical is determined to lie little more than 1 eV above the D_2O + D threshold [Luo99] and could possibly be a reason for the sharp cutoff at 1.17 eV in the KER histogram, recent charge exchange measurements on H_3O^+ [Man09] find almost no signs of radiative decay for the lower H_3O^+ levels studied.

Also the KER histogram of the second two-body channel OD + D_2 reveals a large KER deficit with respect to the channel energy release of $(E^0_{KER})^{(\beta)} = E_{\mathrm{OD,D_2}}$, as can be seen in fig. 6.3 (c). Since *both* fragments can be internally excited in this channel, possible structures indicating a decrease in the event density due to the opening of the branches OD + D + D and $\mathrm{OD}(\mathrm{A}^2\Sigma^+)$ + D_2 might be blurred. The fact that the only decline in fig. 6.3 (c) is to the left of the maximum at $E_{KER} \sim 1.2$ eV, which is close to the opening of the three-body channel, gives rise to the conclusion that, first, the branching to $\mathrm{OD}(\mathrm{A}^2\Sigma^+)$ is minor and, second, the OD fragment is only weakly excited compared to the D_2. This is in good agreement with previous measurements [Gou97], where OH fragments from the DR of H_3O^+ were found to be produced only in lower vibrational states ($v \leq 3$). It should be mentioned that, as $E_{\mathrm{O,D,D_2}}$ also coincides with the maximum in fig. 6.3 (c), the decline in that histogram might be caused by an increase of three-body events O + D + D_2. However, as mentioned above (see fig. 6.2), less than 1 % of all events were found in that dissociation channel. The KER histogram in fig. 6.3 (a) will be discussed in the next section.

6.3.2 3D imaging with the multi-hit optical gating detector

Full 3D kinetic energy release

Unlike the EMU detector, where the kinetic energy release distribution shown in fig. 6.3 (a) needs to be reconstructed from the projected data by means of a Monte-Carlo simulation based on additional assumptions (fig. 6.3 (a)), the multi-hit optical gating detector yields a directly measured 3D KER of the D_3O^+ three-body DR channel. This 3D KER is shown by the red curve in fig. 6.4, a broad distribution ranging from near-zero to approximately 2.7 eV with a peak at 1.17 eV that coincides with the expected kinetic energy release in the three-body channel of ground-state reactant and products, $E_{\mathrm{OD,D,D}}$. Modeling the KER by means of a Monte-Carlo simulation assuming a single-valued kinetic energy release $E_{KER} = E_{\mathrm{OD,D,D}}$ and perfect detector resolution, a distribution indicated by the blue curve in fig. 6.4 is

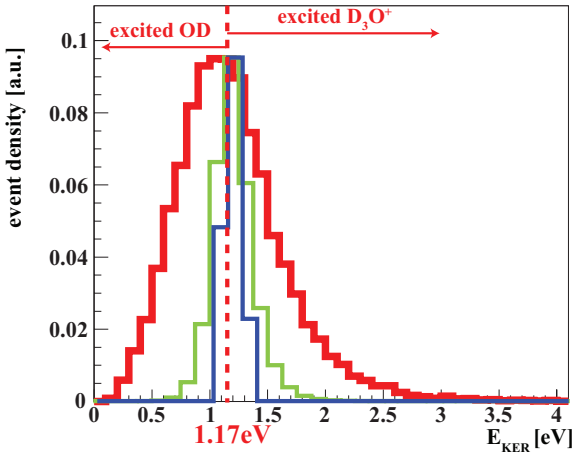

Figure 6.4 KER distribution of the DR channel $D_3O^+ \rightarrow$ OD+D+D. (red) Experiment, data obtained with the 3D imaging detector, corrected by additional gating time correction (see fig. 4.12). (blue) Simulation, isotropic distribution, single $E_{KER} = E_{\mathrm{OD,D,D}}$, perfect spatial and timing resolution, target length $L_t = 1.13\,\mathrm{m}$. (green) Simulation as (blue), additional limited timing resolution of $\sigma_t = 1.1\,\mathrm{ns}$.

obtained. The broadening compared to the expected δ-function is caused by the extended interaction region in the target. Additional broadening is created by the limited time resolution of the detector, which is illustrated by the green curve in fig. 6.4. This curve displays the total width induced by instrumental insufficiency. So, the deviation of this curve from the measured distribution allows the conclusion that the differences in shape and broadness are physical.

The KER distribution measured with the 3D detector avoids the additional assumptions on the dissociation geometries required in the reconstruction of the corresponding curve from the 2D EMU data (fig. 6.3 (a)). The shapes are similar and reveal a peak in the KER distribution of $E_{\mathrm{OD,D,D}} = 1.17\,\mathrm{eV}$. In addition, it discloses that approximately 40 % of all DR events have a KER lower than $E_{\mathrm{OD,D,D}}$ while about the same fraction features a KER that exceeds the channel energy release by up to approximately 1.25 eV. After accounting for the discussed broadening effects due to the extended interaction region and the finite timing resolution of the detector, more than 30 % of all three-body events reveal additional kinetic energy of up to approximately 1 eV. The KER distribution reconstructed form the EMU data (fig. 6.3 (a)) shows a similar tail to higher energies which extends up to $\sim 1\,\mathrm{eV}$, in good agreement with this conclusion.

Similar observations have been made in 2D fragment imaging measurements of the three-body channel by [Zha09a], where *projected* distances in the OD + D + D dissociation channel corresponding to kinetic energy releases above $E_{\mathrm{OD,D,D}}$ were reported. The corresponding transverse distributions of the projected KER, $E_\perp$, for the present experiment, as obtained by the two different detectors, are shown in

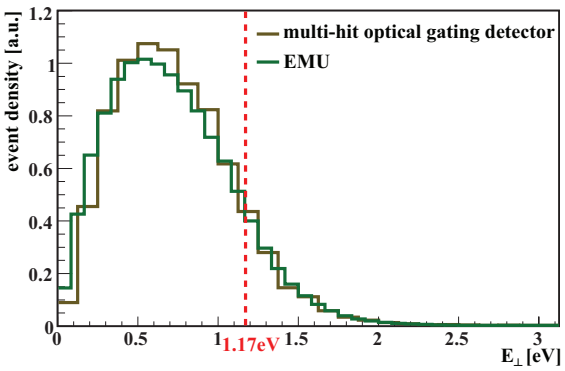

Figure 6.5 Transversal kinetic energy $E_\perp$ of the experimentally observed D_3O^+ DR channel OD + D + D, measured with the multi-hit optical gating detector (brown) and the EMU (green). Given the difference in efficiency and the slightly differing measurement conditions, the measured distributions demonstrate good agreement.

fig. 6.5. In the previous experiment [Zha09a] approximately 17 % of the measured data contributing to the squared transverse distance distribution were estimated to originate from residual gas collisions. Consequently, all events implying such an energy excess were, in that experiment, interpreted as background and disregarded in the further analysis. Referring to the non-zero dipole moment of the H_3O^+ ground state and to the fact that all vibrational modes of the molecular ion are infrared active, a storage time of 5 s was assumed to be sufficient for complete internal cooling of the ions. The vibrational excitation of the parent ion was believed to be vanishingly small and the rotational temperature was considered to correspond to the ambient temperature of 300 K, which then appeared to justify such a procedure.

In the present experiment, however, the background contribution in the squared transverse distance distribution can be directly measured either through the center-of-mass cut or by background measurement at $E_d = 1$ eV where the DR cross section has a minimum (sec. 6.2), from which it is found to be less than 0.1 %. Therefore, a large background contribution as assumed in [Zha09a] can be ruled out. The only viable explanation for the observed excess energy is significant excitation of the hydronium ions undergoing DR.

As pointed out earlier, the calculated transition dipoles [Col83] for all vibrational modes imply lifetimes of the infrared-active states of less than 1 s (appendix A.2). This leaves rotational excitation as the only possible source of the excess energy observed. This conclusion is supported by the fact that plasma discharge ion sources, used in the current experiment as well as in [Zha09a], are known for producing ions in an initial state of high rotational excitation. Although a long persistence of such an excitation is not expected generally, as radiative lifetimes of even the lowest

inversion-rotational states are predicted to be below a second [Bot83], the $\Delta K = 0$ selection rule governing the decay of rotating non-planar symmetric top molecules (eq. (3.39) in [Tow55]) does suppress transitions to lower J states, resulting in long-lived rotational states of the D_3O^+ ions.

Similar to the EMU results (fig. 6.3 (a)), also a significant number of events with energy releases below $E_{\mathrm{OD,D,D}}$ are observed in fig. 6.4. Like in the two-body channels, these findings indicate the production of internally excited fragments. With OD being the only molecular fragment, it must be this particle absorbing some fraction of the released energy. Previous measurements indicate the OH fragments from the DR of H_3O^+ to be mainly in the $v = 0$ and $v = 1$ states with almost equal probabilities [Gou97, Zha09a], which well explains the shape of the measured KER below $E_{\mathrm{OD,D,D}}$.

Dalitz Plots

In sec. 3.3.2 Dalitz plots were described as an established method to represent the fragmentation geometries of three-body dissociations. Figure 6.6 (a) shows the results of the present experiment for OD + D + D. As the two D atoms in the three-body channel can not be distinguished, the data set for each molecule is additionally symmetrized with respect to permutations of the identical fragments. This procedure is necessary in order to avoid artifacts in the plots caused by the arbitrary numbering of the D atoms during image processing. As a result, the Dalitz plots exhibit a twofold symmetry with the $\eta_1 = 0$ axis being the axis of reflection (eq. (3.19)). All dissociations of isosceles geometry are represented by coordinates along this axis. In contrast, coordinates at the plot's edge stand for dissociations resulting in a linear configuration. In more detail, the coordinates $(\eta_1, \eta_2) = (0, -\frac{1}{3})$ at the bottom of the circle display a linear dissociation in which the OD stays at rest and momentum conservation enforces a back-to-back dissociation of the D atoms. Break-ups with both D atoms being emitted at the same velocity and direction, corresponding to an effective two-body dissociation geometry where the D fragments have zero distance, are represented at the top of the circle with the coordinate $(\eta_1, \eta_2) = (0, \frac{1}{3})$. Another case of an effective two-body geometry, where the impact positions of one D and the OD coincide, is displayed on the left and right side of the circle close to (but not exactly at) $(\eta_1, \eta_2) = (\frac{1}{3}, 0)$ and $(\eta_1, \eta_2) = (-\frac{1}{3}, 0)$, respectively. Simulations have demonstrated that the limited ability of the camera to separate fragments arriving

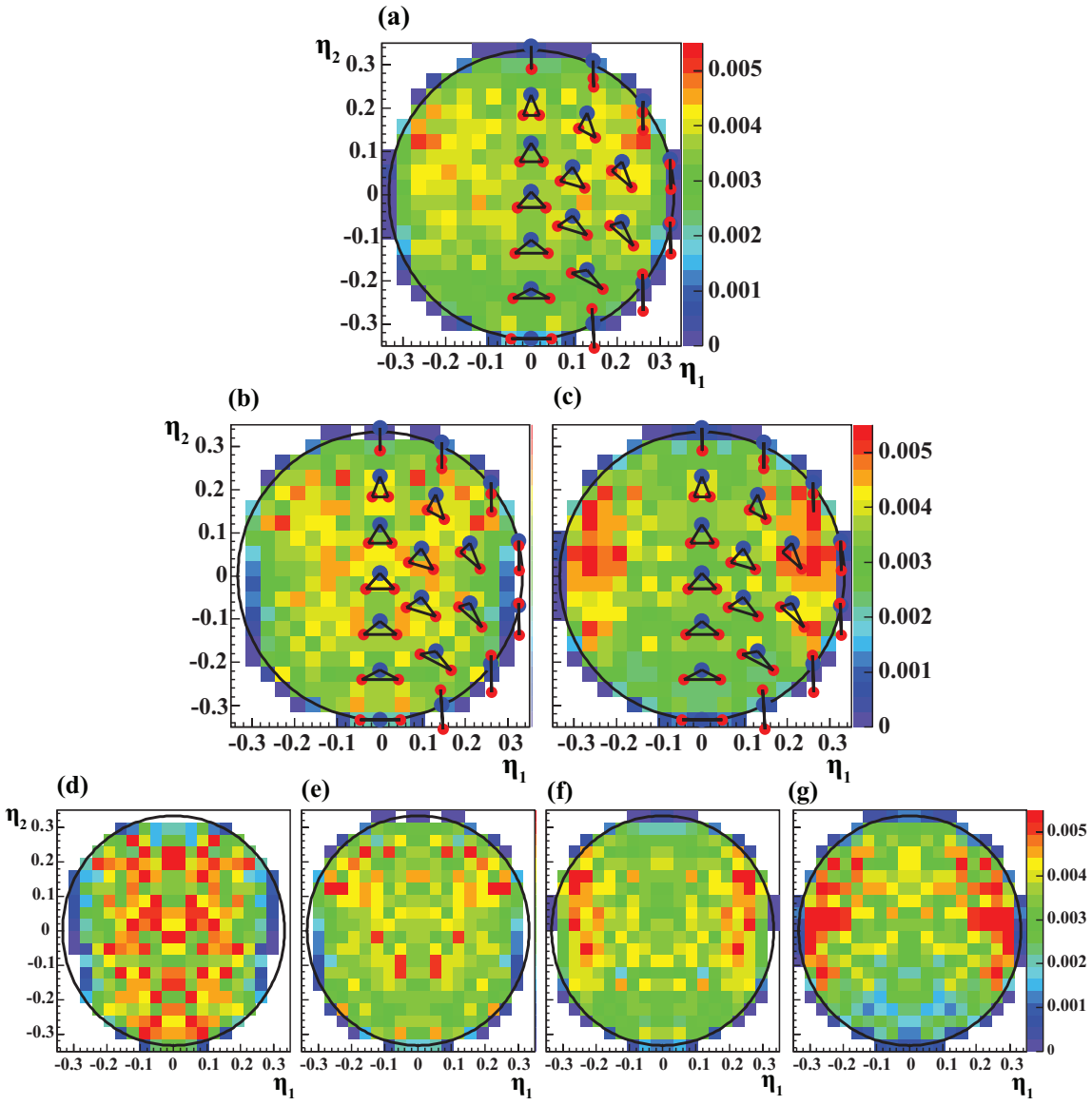

Figure 6.6 3D Dalitz plots, as defined in sec. 3.3.2, of the experimentally observed DR three-body channel $D_3O^+ \rightarrow OD+D+D$ for different KER. (a) all E_{KER}. (b) $E_{KER} < 1.17\,\text{eV}$. (c) $E_{KER} > 1.17\,\text{eV}$. (d) $E_{KER} < 0.7\,\text{eV}$ (e) $0.7\,\text{eV} < E_{KER} < 1.1\,\text{eV}$. (f) $1.1\,\text{eV} < E_{KER} < 1.5\,\text{eV}$. (g) $E_{KER} > 1.5\,\text{eV}$. The small triangles indicate the dissociation geometry for selected points of the Dalitz plots.

at small mutual distances reduces the detector acceptance for these geometries close to the two-body geometry in particular at small KER. As expected, this effect particularly becomes apparent for events of small kinetic energy releases, as can be seen in fig. 6.6 (b,d).

Unfortunately, the low statistics that could be acquired in spite of $\sim 20\,\mathrm{h}$ of total data taking time enforce the rough binning of the Dalitz plots in fig. 6.6. Still, the data in fig. 6.6 (a) clearly reveal an anisotropy of the break-up geometries distribution preferring asymmetric dissociations ($|\eta_1| > 0$) in which a significant part of the released kinetic energy is distributed to the heavy OD fragment. Moreover, smaller opening angles between the D atoms ($\eta_2 \geq -0.1$) are preferred. In a further analysis the dissociation geometries are considered in dependence of the KER, separately plotting events with $E_{KER} < 1.17\,\mathrm{eV}$ (fig. 6.6 (b)) and $E_{KER} > 1.17\,\mathrm{eV}$ (fig. 6.6 (c)). In these representations, a remarkable difference can be observed. While the plot of low KER events is mostly homogeneous, indicating no preferred dissociation geometry, a clearly structured histogram is found for $E_{KER} > 1.17\,\mathrm{eV}$. This suggests that a pronounced anisotropy occurs in the three-body decay of DR events with higher KER. Figure 6.6 (c) reveals a local enhancement of up to 40 % for $|\eta_1| \gtrsim 0.2$, indicating an increased number of dissociations in which one D atom is released at much smaller velocity than the other, as in the corresponding geometry one D atom is found at large distance from the OD subunit while the other D fragment is detected adjacent to the heavy fragment. A further subdivision of the data into even smaller KER ranges is displayed in the third row of fig. 6.6. In spite of the low statistics, a considerable change in the shape of the resonance can be observed for high KER fig. 6.6 (f), (g). This observation raises questions about the dissociation mechanism and its relation to the findings from the two-body channels. These are addressed in the upcoming section.

6.4 Dissociation mechanisms

The question of possible dissociation pathways of the hydronium after colliding with cold electrons has been raised previously, mainly in the context of investigating the tendency in the branching ratios. Motivated by the results from ion-storage ring experiments [And96, VC97], but also by experimental limitations in the investigation of the details of the reaction mechanism, *ab initio* calculations have been performed [Ket99]. Herein, the ground- and energetically accessible excited-state potential energy surfaces that connect H_3O to its various decay products are investigated. In particular, the surprising fact that, even though the water producing two-body channel is the most exothermic reaction pathway (fig. 6.1), the branching into the

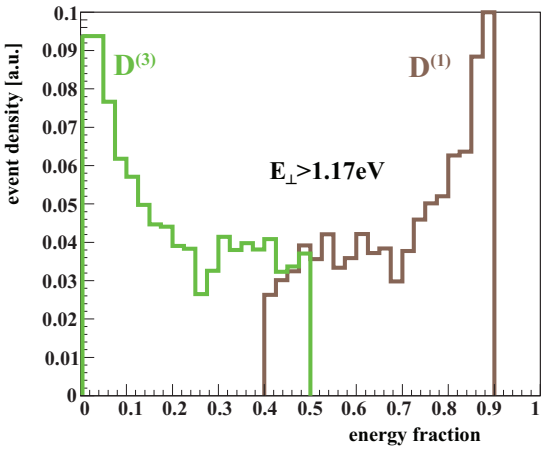

Figure 6.7 Relative transversal kinetic energy distributions of the two D atoms detected in the DR three-body channel $OD + D + D$ of D_3O^+. Only events with $E_\perp > 1.17\,\text{eV}$ are shown. The distributions are normalized to the corresponding distribution obtained from a Monte Carlo simulation calculating breakup geometries equally distributed in phase space. $D^{(1)}$ and $D^{(3)}$ are defined such that $E_\perp^{D^{(3)}} < E_\perp^{D^{(1)}}$.

three-body channel $OD + D + D$ (fig. 6.2) is dominant, has attracted attention. The theoretical investigations in [Ket99] proposed most of the three-body dominance to be explained by a possible sequential decay, with the internal energy of the water allowing the further decay to produce $OD + D + D$:

$$D_3O^+ + e^- \rightarrow D_2O^* + D \rightarrow OD + D + D. \tag{6.10}$$

6.4.1 Evidence for a sequential decay

The results obtained from the current experiment and presented in the previous paragraphs might be the first experimental evidence for the two-step process of eq. (6.10) in the three-body DR channel OD+D+D of D_3O^+. The local enhancement of up to 40 % for $|\eta_1| \gtrsim 0.2$ detected in the Dalitz plot for events of large KER (fig. 6.6 (c)) suggests such an interpretation: the first D is ejected within femtoseconds as the lifetime of the D_3O^* resonance initially formed in the electron collision is comparable to the vibrational period in this system [FM06]. Besides, the intermediate water molecule has a dissociative lifetime longer than a few picoseconds, which is long enough for the initially split-off D atom to become essentially ineffective for the subsequent D_2O^* decay [Mau97]. Thus, the two bond break-ups are independent of each other concerning the resulting angles between the fragments.

In [Zha09b] the sequential formation of the $CH_3 + H + H$ channel in the DR of CH_5^+, studied in a similar ion-storage ring experiment, is discussed. Here, the fraction of the total transversal kinetic energy released, which is received by each of

the hydrogen atoms, $E_\perp^{H^{(1)}}$ and $E_\perp^{H^{(3)}}$ is plotted, where the smaller energy is always denoted as $E_\perp^{H^{(3)}}$. The illustration reveals a preference for one of the hydrogen atoms to receive only a small fraction of the available energy, while the second H atom is released with the major fraction of the KER. This is interpreted as an indication for a preference in energy distribution implying the sequential decay of $CH_5^+ + e^- \rightarrow CH_4^* + H \rightarrow CH_3 + H + H$.

An analogous representation of the relative transversal kinetic energy distribution of the two D atoms detected in the DR three-body channel of D_3O^+ is illustrated in fig. 6.7. As in [Zha09b], the density of events is normalized to that obtained from the Monte-Carlo simulation of an isotropic break-up with a flat statistical distribution of dissociation geometries. Clearly, events with a strong asymmetric energy partitioning are favored. The characteristics of the observed normalized energy distributions agree well with the ones presented in fig. 2 (c) of [Zha09b], and similarly indicate the presence of a sequential dissociation as described in eq. (6.10).

In addition, the sharp cut-off found in the KER distribution of the two-body channel $D_2O + D$ in the EMU data is another indication for the formation of an intermediate state. The minimum KER of the water producing channel at 1.17 eV in fig. 6.3 agrees perfectly with the expected stability limit of D_3O^+ towards three-body dissociation, suggesting the further dissociation of any highly excited water molecules above the first dissociation threshold, D_2O^*, into $OD + D$, still within the electron target.

6.4.2 Pathways to dissociation

Considering the distances r_1 and r_3 of the two D atoms from the OD subunit in a dissociating D_3O molecule, the structure of the relevant potential energy surfaces is roughly sketched in fig. 6.8. The initial capture of an electron leads to D_3O Rydberg states, which, as the binding becomes stronger, open towards the configuration $D_2O + D$ (along r_3). As shown in fig. 6.8 (a), the release of one D atom can lead to the formation of a vibrationally excited water molecule as soon as the energy of the separating D atom exceeds 1.17 eV. On the other hand, for lower energy release, three-body dissociation into $OD + D + D$ occurs. For such decays, the motion in the r_1-r_3-plane is not strongly restricted and can proceed in a wide range around the diagonal $r_1 = r_3$. Such events are expected to be rather equally distributed in phase

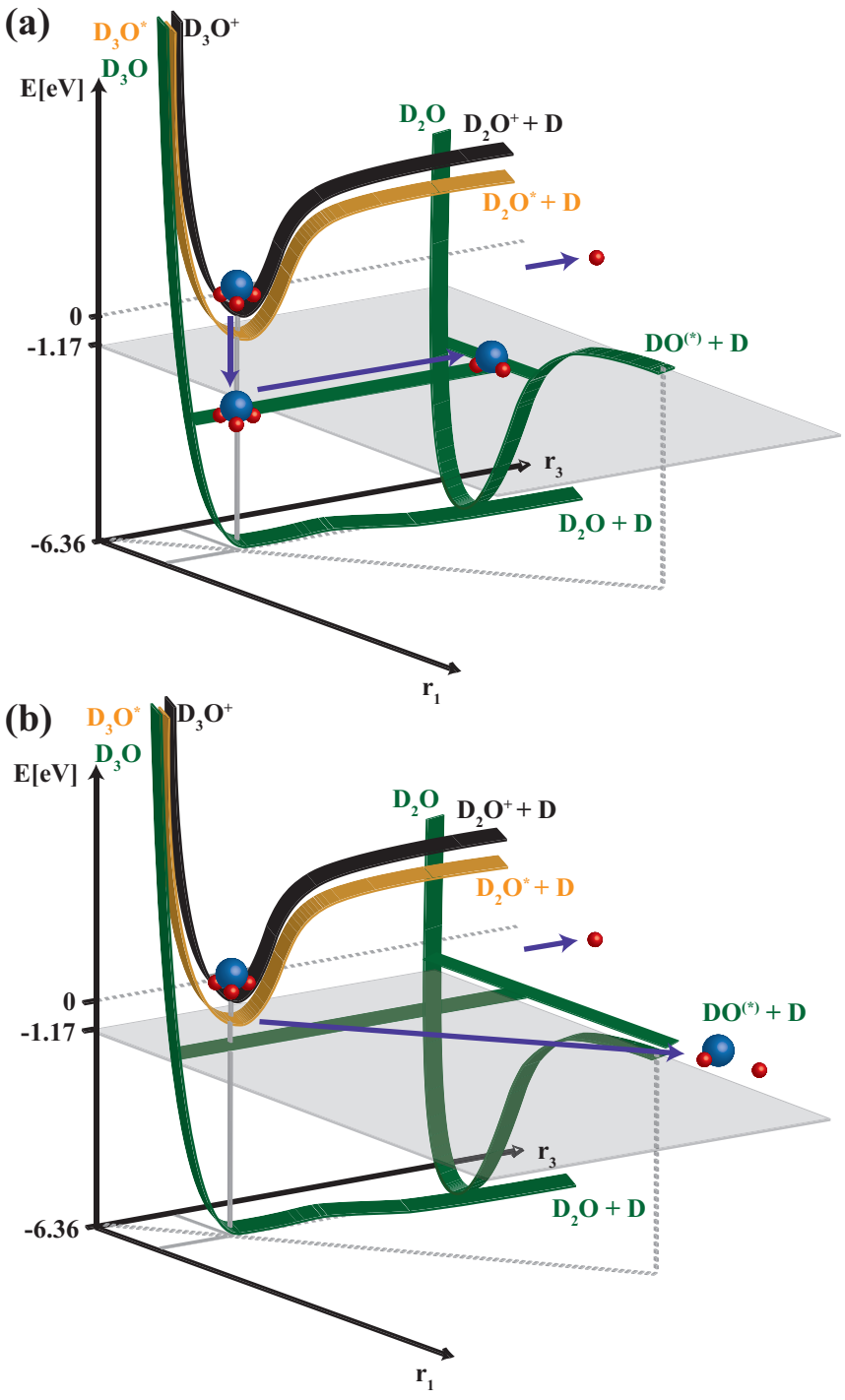

Figure 6.8 Sketch of proposed pathways in the dissociative recombination of near ground-state D_3O^+ into (a) $D_2O + D$ and (b) $OD + D + D$.

space and to result in a flat Dalitz plot as measured for low KER (fig. 6.6 (b)). This will also be connected with a rather equal sharing of the kinetic energy between the two D atoms.

Scenarios leading to an unequal sharing of the two D fragments, as observed under some conditions, are illustrated in fig. 6.9. Depending on the involved potential energy surface, the D atom dissociating from a highly excited water receives either the major amount or a very small fraction of the available energy.

As the resonances in the Dalitz plot indicating sequential decay appear only for higher three-body KER, the collision system can be expected to carry a considerable amount of rotational excitation introduced by the parent ion. Hence, the strongly vibrating D_2O can be expected to also carry a considerable amount of rotational energy due to angular momentum conservation [Buh10b]. If the total ro-vibrational energy exceeds the dissociation limit of water by some amount, the levels available in this energy range could be populated behind a rotational barrier. Then, the rotational predissociation [Ler71, Car81] of these states would produce D fragments released with only little kinetic energy in the second decay step (fig. 6.9 (a)). It should be noted that the picture used here does not take into account the various vibrational modes of D_2O. Hence, also vibrational modes along other coordinates than the one sketched here can carry additional energy and lead to similar predissociation.

In contrast, an inverted energy partitioning might be expected from the process illustrated in fig. 6.9 (b). Calculations[5] predict a dissociative PES of $D_2O^* + D$, on which, at least considering the energy balance of such a process, a water molecule could be born through emission of a low-energetic D atom. This surface then decreases steeply forming OD^* and a high-energetic D atom. In this case, the rotationally dressed shape of the ionic potential would be of minor importance for the two-step process to proceed. Rather, the system has to evolve into the repulsive water state, for which the additional energy in the initial state may be helpful. Clearly, the amount of energy available in the first dissociation step would be small, leaving the major part to be received by the second D atom. At this point, calculations are needed to evaluate the plausibility of the different scenarios to occur. These are presented in the upcoming paragraph.

[5] A. E. Orel, private communications

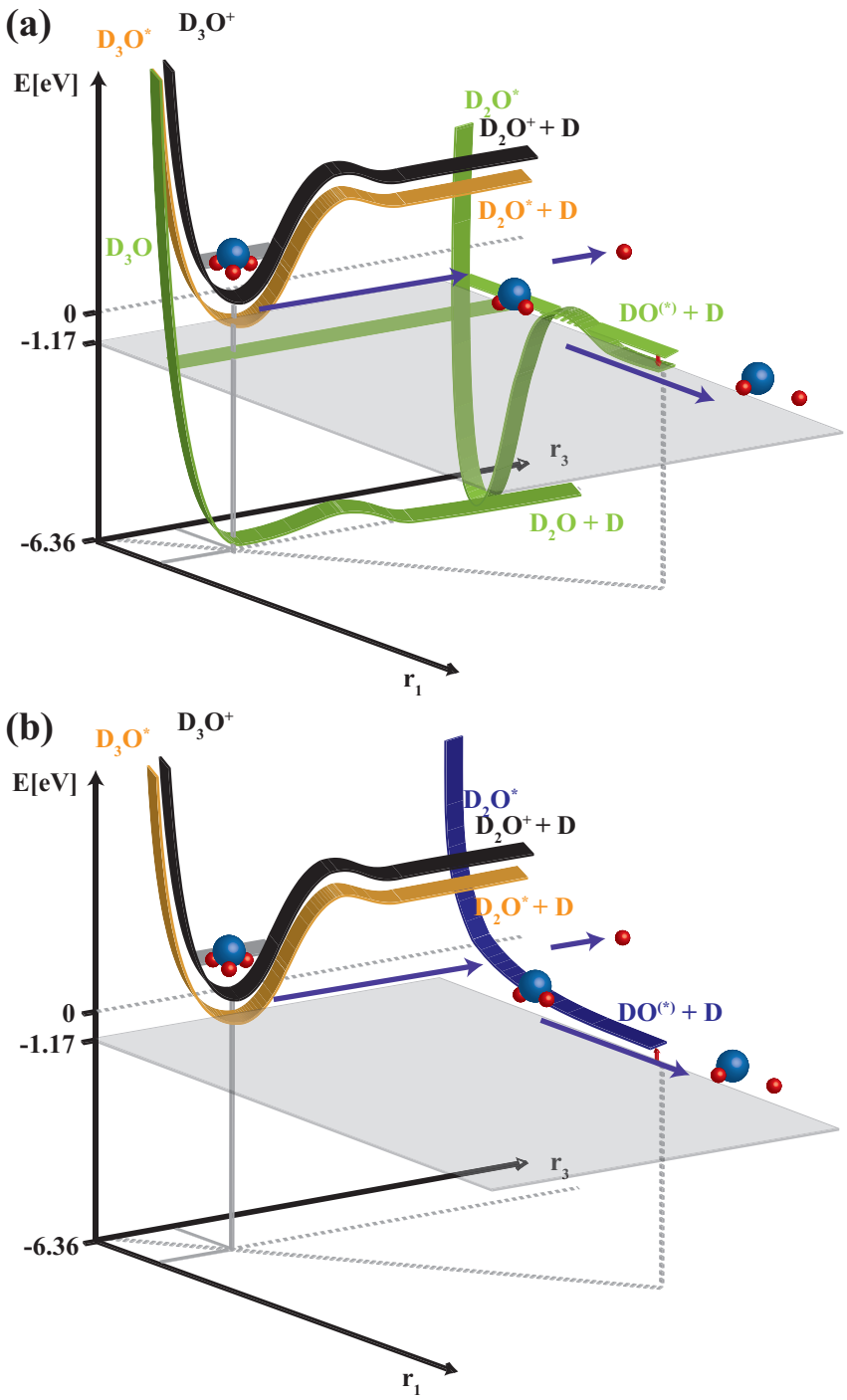

Figure 6.9 Sketch of proposed pathways in the dissociative recombination of rotationally excited D_3O^+ into $OD + D + D$. (a) The first D atom is released with the major fraction of the available kinetic energy. (b) The first D atom receives only a very small amount of the available kinetic energy.

6.4.3 Investigating possible dissociation pathways

A simple model is used to estimate the effects of a sequential decay on the configurations displayed in a 3D Dalitz plot. For the kinematic model, it is assumed that (a) the D_3O^+ is in its ground state, (b) the distance between interaction point and detector is single-valued, (c) the KER is fixed to $E_{KER}^{fix} = 1.17\,\text{eV}$, i.e. there is no internal excitation of the products, (d) the two dissociations occur instantaneously at the same interaction point. Further, the energy fraction released in the first decay step is a constant fraction α of the total KER E_{KER}^{fix}, leading to

$$\begin{aligned} E_{KER_1} &= \alpha \cdot E_{KER}^{fix} = \frac{1}{2}\, m_{\mathrm{D_2O}}\, v_{\mathrm{D_2O}}^2 + \frac{1}{2}\, m_{\mathrm{D^{(1)}}}\, v_{\mathrm{D^{(1)}}}^2 \\ E_{KER_2} &= (1-\alpha) \cdot E_{KER}^{fix} = \frac{1}{2}\, m_{\mathrm{OD}}\, v'^2_{\mathrm{OD}} + \frac{1}{2}\, m_{\mathrm{D^{(3)}}}\, v'^2_{\mathrm{D^{(3)}}}, \end{aligned} \tag{6.11}$$

where v_{OD} and $v'_{\mathrm{D^{(3)}}}$ are the velocities in the co-moving frame of D_2O after the first decay. A velocity vector diagram of the described break-up is shown in fig. 6.10.

Considering momentum conservation in each decay step yields, together with some geometric relations, the kinetic energies of the fragments as a function of α and γ:

$$\begin{aligned} \hat{E}_D^{(3)} &= \frac{E_D^{(3)}}{E_{KER}^{fix}} = \frac{m_{\mathrm{D^{(1)}}} m_{\mathrm{D^{(3)}}}}{m_{\mathrm{D_2O}} M}\alpha + \frac{m_{\mathrm{OD}}}{m_{\mathrm{D_2O}}}(1-\alpha) + 2\sqrt{\frac{m_{\mathrm{D^{(1)}}} m_{\mathrm{D^{(3)}}} m_{\mathrm{OD}}}{m_{\mathrm{D_2O}}^2 M}(1-\alpha)\alpha}\,\cos\gamma \\ \hat{E}_D^{(1)} &= \frac{E_D^{(1)}}{E_{KER}^{fix}} = \frac{m_{\mathrm{D_2O}}}{M}\alpha \\ \hat{E}_{OD} &= \frac{E_{OD}}{E_{KER}^{fix}} = \frac{m_{\mathrm{OD}} m_{\mathrm{D^{(1)}}}}{m_{\mathrm{D_2O}} M}\alpha + \frac{m_{\mathrm{D^{(3)}}}}{m_{\mathrm{D_2O}}}(1-\alpha) - 2\sqrt{\frac{m_{\mathrm{D^{(1)}}} m_{\mathrm{D^{(3)}}} m_{\mathrm{OD}}}{m_{\mathrm{D_2O}}^2 M}(1-\alpha)\alpha}\,\cos\gamma \end{aligned} \tag{6.12}$$

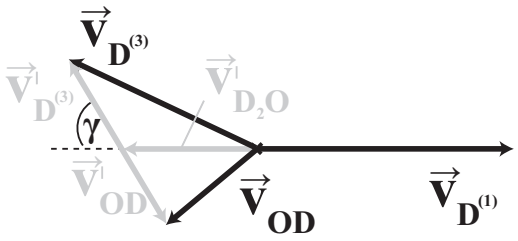

Figure 6.10 Sketch of a simple model describing the sequential decay $D_3O^+ + e^- \rightarrow D_2O^* + D \rightarrow OD + D + D$. The black vectors $\vec{v}_i$ indicate the three-body dissociation in the co-moving frame of the neural compound, while the gray vectors $\vec{v}_i\,'$ illustrate the second decay in the co-moving frame of the sub-system D_2O^*.

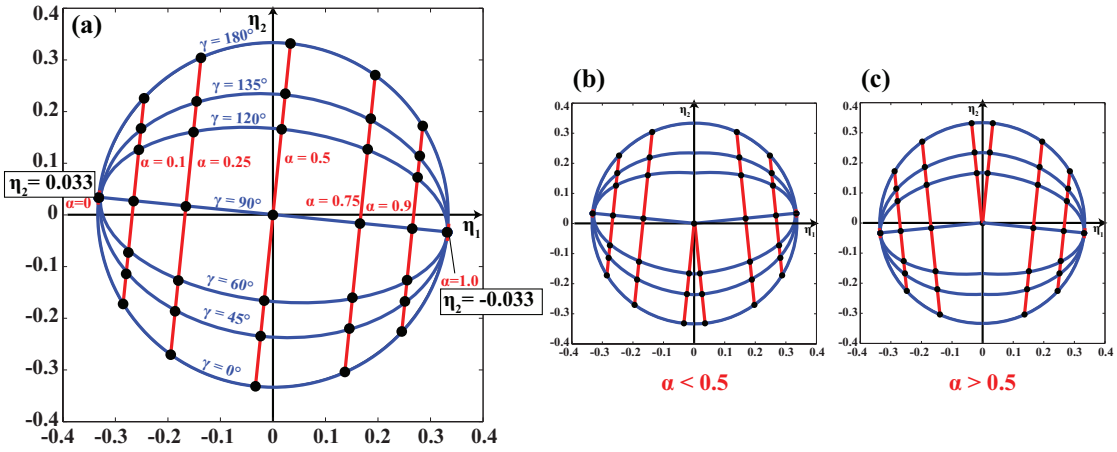

Figure 6.11 Sketch of a Dalitz plot illustrating a sequential decay. (a) Resonances ($\alpha = const.$) appear as straight lines, whereas the fragmentation angle γ in the second step varies along these lines. In (b) and (c) the Dalitz plot is symmetrized around the $\eta_1 = 0$ axis due to the indistinguishability of the D atoms. This leads to the two cases $\alpha < 0.5$ (a) and $\alpha > 0.5$ (c).

where M is the total mass of the ion D_3O^+. Inserting these energies in eq. (3.19) yields the Dalitz coordinates η_1 and η_2.

Molecules dissociating with an energy ratio α randomly distributed along the interval [0,1] would fill the area of the 3D Dalitz plot. In contrast, resonances ($\alpha = \text{const.}$) appear as straight lines in the Dalitz plot (fig. 6.11), whereas the fragmentation angle γ in the second decay step varies along these lines. Figure 6.11 (a) illustrates the different configurations for dissociations in which the major amount of the available energy is released with the first D atom ($\alpha \lesssim 1$) and the inverse case, in which almost all energy is released with the second D atom ($\alpha \gtrsim 0$). Due to the indistinguishability of the D atoms in the experiment, the Dalitz plot is symmetrized regarding the $\eta_1 = 0$ axis, so it can either represent a decay, in which the first $D^{(1)}$ atom is released with the major amount of kinetic energy ($\alpha > 0.5$, fig. 6.11 (b)) or the case, in which the $D^{(3)}$ atom in the second decay step dissociates with most of the kinetic energy available ($\alpha < 0.5$, fig. 6.11 (c)). Both cases are distinguised by the slopes of the lines. The tendencies of these rough calculations have been confirmed by a Monte-Carlo simulation of the two-step decay with varying α.

A comparison with the measured data fig. 6.6 reveals the interesting finding, that, depending on the kinetic energy released in the total break-up, different mechanisms seem to play the dominant role. While for $1.1\,\text{eV} < E_{KER} < 1.5\,\text{eV}$ (fig. 6.6 (f)) the

shape of the resonance seems to correspond to a dissociation in which $D^{(1)}$ is ejected with the major amount of energy, for the highest observed kinetic energy releases $1.5\,\mathrm{eV} < E_{KER}$ (fig. 6.6 (g)) the slope of the resonance appears to have changed, indicating a favored two-step decay in which $D^{(3)}$ is released with most of the KER available. These findings are explored further in the next paragraph.

6.4.4 Proposed dissociation pathways

The rough considerations of the previous paragraph have been useful supporting the assumption of excited D_3O dissociating preferentially via an intermediate step. However, the questions on the dissociation pathways remain unanswered: how does the dissociation proceed so that water is produced only in highly excited states? How does the direct decay into the fragments OD + D + D occur? And what mechanisms could lead to the observed two-step decays?

Approaching these questions, theoretical input is indispensable. Previous experiments on the electron capture process of H_3O^+ and the corresponding need for support regarding the interpretation of the results have been motivation for *ab initio* calculations of the neutral molecule. High H_3O^* Rydberg states are generated in this process, which eventually deexcite by electronic transitions. Therefore, these states have been investigated with precise quantum chemical calculations [Luo99] for the equilibrium geometry of H_3O^+, from which possible dissociation paths of metastable H_3O^* and barriers were expected to be found.

As the work of [Luo99] has not been treating the OH + H + H channel, new calculations for the analysis of the current experiment were needed. Recently, *ab initio*

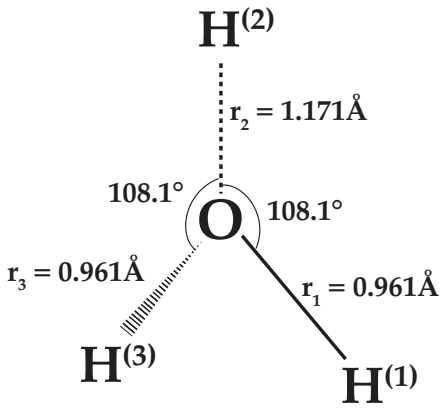

Figure 6.12 Structural formula of H_3O, calculated by [Ket99] to be the transition state for the dissociation of ground-state H_3O into ground state $H_2O(X^1A_1)$ and H (named N 14 in [Ket99]). The dihedral angle between the surface spanned by $H^{(1)} - O - H^{(2)}$ and the surface defined by $O - H^{(2)} - H^{(3)}$ is determined to be 117.0°.

Table 6.1 Calculated energies for the lowest electronic states of H_3O and the ion H_3O^+. Data taken from [Luo99].

State	Space group	Symmetry	Ionization potential [eV]
ion	C_{3v}	$^1A_1$	–
$3pa_1$	C_{3v}	$^2A_1$	−2.5718
3pe	C_s	$^2A''$	−3.2537
3pe	C_s	$^2A'$	−3.2509
$3sa_1$	C_{3v}	$^2A_1$	−5.3573

calculations of adiabatic potentials for the ion H_3O^+ and the 20 lowest states of H_3O have been performed[6]. In [Ket99], a specific geometry of the molecule, shown in fig. 6.12, is suggested to be the transition state for the dissociation of ground-state H_3O into ground-state H_2O and H. Based on this geometry, two-dimensional PES were calculated as a functions of the two H distances r_1 and r_3. The potentials were found to depend only weakly on the dihedral angle (as defined in fig. 6.12), and were calculated for fixed angles as well as for a fixed bond length r_2. Contour plots of the ion ground state, the neutral ground state and three selected excited states are presented as functions of the two H distances, r_1 and r_3, in fig. 6.13 and one-dimensional diagonal cuts through the PES at $r = r_1 = r_3$ are displayed in fig. 6.14. A larger set of potentials is also shown for fixed equilibrium distances r_2 and r_3 as a function of a single H distance r_1 in fig. 6.15. The same calculations performed for the equilibrium geometry compare well with the results from [Luo99], which are listed in tab. 6.1.

Although the potential energy surfaces in fig. 6.13 and fig. 6.15 are simplified and cannot be expected to precisely reproduce the real PES, some significant conclusions can be drawn from these calculations in combination with the findings from [Luo99], [Ket99] and [Kok]:

Electronic deexcitation. At geometrical equilibrium, the potential energy surfaces of A'-states and A''-states are connected by conical intersections (fig. 6.15). Thus, after electron capture, the electronic deexcitation of the excited Rydberg state is aided by the Jahn-Teller coupling between the degenerate states (indicated

[6] A. E. Orel, private communications

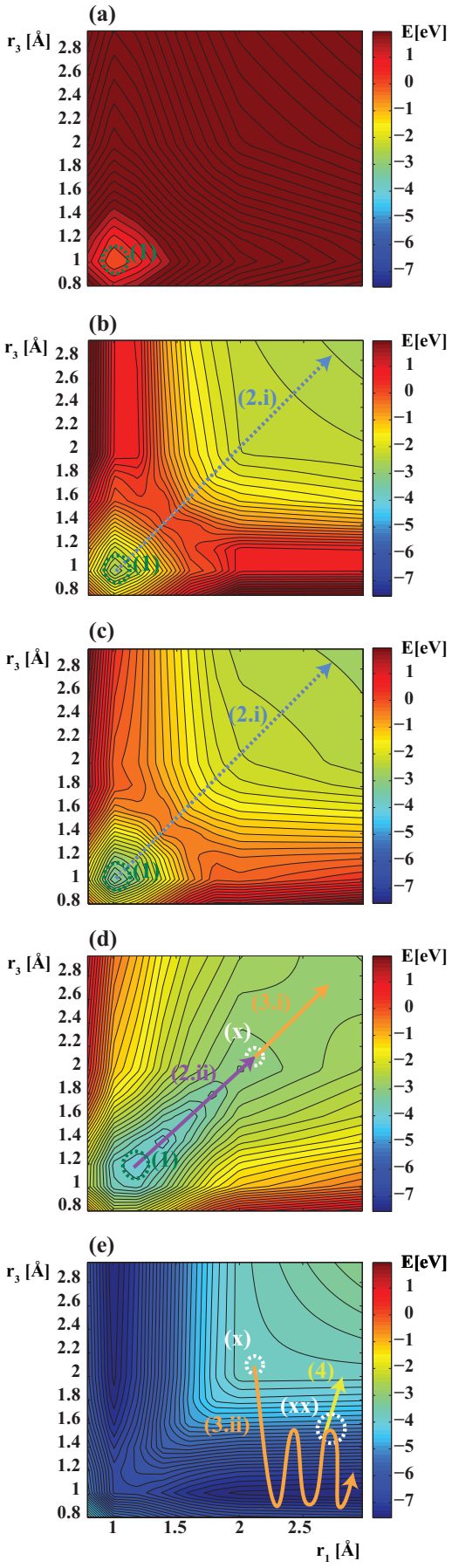

Figure 6.13 Contour plots of the H_3O two-dimensional potential energy surfaces calculated as a function of the two H distances r_1 and r_3 (nomenclature as in fig. 6.12). All angles and the bond length r_2 have been kept fixed. (a) Ionic ground state. (b)-(d) Selected excited states. (e) Neutral ground state. Process steps are indicated as follows:
(1) After electron capture, step-wise deexcitation of the excited Rydberg state by Jahn-Teller coupling is assumed. The decrease in total electronic energy is compensated by an increase of vibrational energy.
(2.i) Alternatively, the initial energy of the molecule after capturing the electron is sufficient to overcome the potential barrier for increasingly vibrating H atoms ($r_1 = r_3 \approx 1.5$ Å). In this case, a direct dissociation into the thee-body channel would be possible.
(2.ii) The vanishing barrier in the lowest excited state allows for the following steps at point(x):
(3.i) a direct dissociation into the three-body channel $OH^* + H + H$ (yielding an isotropic Dalitz plot),
(3.ii) non-adiabatic transitions towards dissociation into the electronic ground state $H_2O^* + H$, with the water being vibrationally excited.
(xx) Intramolecular vibrational redistribution from the energy, which is stored in a vibrating $O - D^{(2)}$ bond as well as in the vibrational modes changing the angles, to the vibrational energy of the $O - D^{(1)}$ and $O - D^{(3)}$ bonds, is expected.
(4) The coupling to the degrees of freedom in the intermolecular vibrational redistribution drives the dissociation into $OD + D + D$.
All PES calculated by A. E. Orel.

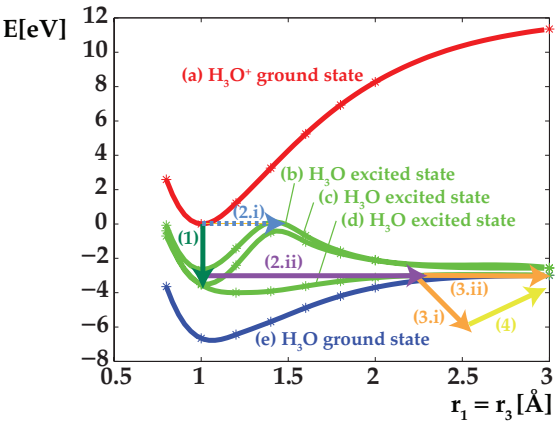

Figure 6.14 One-dimensional cut through the potential energy surfaces, presented in fig. 6.13, along the diagonal. A detailed description of the different steps towards dissociation are given in the caption of fig. 6.13. Calculations from A. E. Orel.

by step (1) in fig. 6.14 and point (1) in fig. 6.13). At this, the decrease in electronic energy must be compensated by an increase of vibrational and, possibly, internal rotational energy.

Water production. During dissociation into the two-body channel $D_2O + D$, the energy stored in the vibration along the $H^{(1)} - O$ axis (or $H^{(3)} - O$, as $H^{(1)}$ and $H^{(3)}$ are indistinguishable) is gradually increased on the PES near point (1) until the bond eventually breaks approximately along *the diagonal* $r_1 \approx r_3$. The calculations reveal, near the H_3O^+ equilibrium geometry, an energetic gap of more than 3 eV between the H_3O first excited and electronic ground states (fig. 6.13 (d) and (e)). Since the H_2O ground state is correlated with the H_3O ground state PES, this rules out any transition into the ground state of H_2O in the H_3O^+ geometry. However, the population of higher vibrational states of near symmetric excitation of two $H - O$ bonds becomes essential (step (2.ii)), allowing a non-adiabatic transition into the ground state at $r_1 = r_3 \approx 2.3$ Å, where the two PES have moved close to each other (step (x)). On the ground state PES, a dissociation into $H_2O^* + H$ becomes possible, with the water being internally excited (line (3.ii)).

Direct dissociation into the three-body channel OH + H + H. In principle, a direct dissociation into the three-body channel is possible along the diagonal of the PES (fig. 6.13), as soon as the vibrational energy directly after the electron capture is sufficient to overcome the potential barrier at $r_1 = r_3 \approx 1.5$ Å (step (2.i)). As the Jahn-Teller coupling is expected to play an important role in the theoretical treatment of the DR process of H_3O^+, the dominant pathway towards direct three-

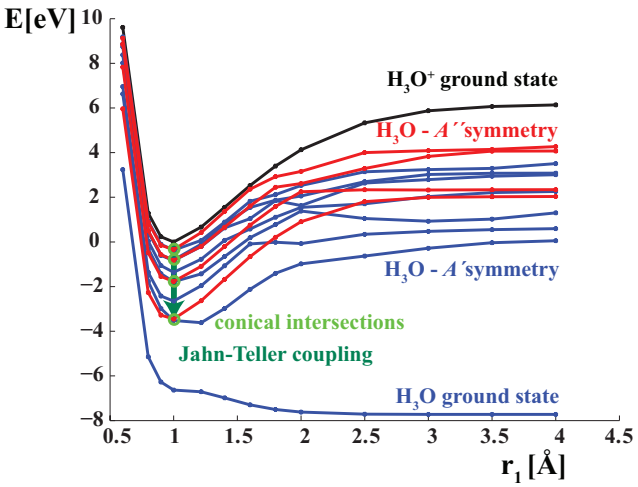

Figure 6.15 One-dimensional potential curves as a function of r_1, with r_2 and r_3 in equilibrium configuration (fig. 6.12). The red and blue curves represent different states of H_3O of A' and A'' symmetry, respectively. In equilibrium configuration, these states are doubly degenerate, leading to conical intersections (chap. 2). The Jahn-Teller coupling is expected to play a crucial role in the DR process of D_3O^+ as it leads to electronic deexcitation [Kok]. Calculations carried out by Ann Orel.

body dissociation proceeds probably – as in the water producing channel – via the PES in fig. 6.13 (d) because of its vanishing potential barrier in diagonal direction. The system can dissociate further along the diagonal by gaining vibrational energy equally distributed among the two coordinates $H^{(1)}$ and $H^{(3)}$ (step (3.i)).

Sequential fragmentation into the three-body channel OH + H + H. In fig. 6.9, two mechanisms have been proposed that could drive the sequential dissociation in case of rotationally excited parent ions. The calculated two-dimensional potential energy surfaces now facilitate an evaluation of the plausibility of each pathway. As discussed above, a transition into the H_3O ground state becomes possible only for configurations of large internuclear distances r. The height of a possible rotational barrier of the final H_2O (or D_2O) was estimated assuming a rotational excitation of 3500 K of the initial ion, as extracted from the analysis of the experimental data (appendix A.3). At $r_1 = r_3 \approx 2.3$ Å, the additional energy due to rotations of the molecule has decreased to less than 40 meV. The small estimated size of the rotational barrier suggests that the assumed population of states behind it, followed by rotational predissociation of the water [Buh10b], is rather unlikely.

A closer look at the measured geometries in the Dalitz plots (fig. 6.6) reveals, despite the bad statistics, a clear change in the preferred geometries for different kinetic energy releases. At small E_{KER}, geometries resembling isosceles triangles ($\eta_1 \approx 0$) dominate (fig. 6.6 (d)). With increasing E_{KER}, the geometries in favor change towards asymmetric configurations in which one D atom is located much

closer to the OD molecule than the other D atom (fig. 6.6 (f),(g)). As the kinetic energy released in all dissociations displayed in fig. 6.6 (d) is considerably smaller than $E_{\mathrm{OD,D,D}}$, these events should be associated to an OD fragment carrying internal excitation. The predominantly symmetric fragmentation geometries observed indicate that the dissociation occurs most probably along the diagonal of the PES (steps (2.ii) $\rightarrow$ (3.ii)).

Towards higher kinetic energy releases (fig. 6.6 (e), (f)), a resonance resembling the two-step pattern for large α (corresponding to the release of a slow D atom in the second step, sec. 6.4.3) gradually develops. In these cases, information on the energy fraction stored in the OD is not accessible anymore. However, for the largest kinetic energy releases (fig. 6.6 (g)), a significant excitation can be clearly excluded, since any additional energy stored in the OD fragment implies an even higher excitation of the parent ion. Hence, fig. 6.6 (g) clearly shows the Dalitz plot of three-body events originating from the DR of rotationally excited D_3O^+ with OD fragments of marginal internal excitation. In this case, a clear two-step pattern remains; however, it more strongly resembles the case for small α.

As discussed above, an essential requirement for a sequential dissociation with large α is the existence of long-lived, highly excited water states. Recently, state-selective spectroscopy experiments have provided evidence for quasibound states of water with lifetimes of up to 60 ps [Gre10]. Generally called Feshbach resonances, these states are characterized by a weak coupling to the reaction coordinate (r_3 in the present case). In order to dissociate, intramolecular energy needs to be redistributed. The PES presented in fig. 6.13 are based on two D fragments dissociating from the D_3O, while all other coordinates, such as angles and the OD bond length r_2 remain fixed. This is a simplification and most certainly does not describe nature accurately. Energy cannot only be stored in the vibrations of the two D atoms dissociating, but is probably also stored in vibrations of the third one, which remains bound in the OD molecule. In first approximation, the $\mathrm{O} - \mathrm{D}^{(2)}$ distance can be thought of as a harmonic oscillator, yielding higher energies as the distance r_2 is varied. The water ground-state is well separated from adjacent electronic states (fig. 6.13), which enhances the probability for intramolecular vibrational redistribution (IVR, [Her06]) to occur (step (xx)). The energy stored in a vibrating $\mathrm{O} - \mathrm{D}^{(2)}$ bond as well as in vibrational modes changing the angles is assumed to be redistributed to the manifold of all other vibrational modes including motion along r_3. In particular,

a coupling to the degrees of freedom that drive the dissociation into OD + D + D is expected. The time scale of such IVR processes in molecules has been found to reach from the picosecond range up the nanosecond region [Her06], which coincides with the lifetimes of the quasibound states of water observed in [Gre10].

This proposed dissociation mechanism does not depend on the initial excitation of the parent ion, which was previously assumed to be a requirement for the two-step decay to occur. In fact, it probably can be observed for any initial state of the ion. For ground-state ions this sequential dissociation is only possible if all energy stored in the vibrational modes of the water molecule is redistributed by IVR into a single vibrating $H^{(3)}$ that eventually splits off. Now, the higher the excitation of the parent ion, the higher is the chance of the water undergoing a second dissociation into OD + D, as it does not have to redistribute all energy stored in its vibrational modes.

This is supported by the findings in fig. 6.6 (f), (g) where the preferred configurations indicating the sequential decay clearly appear. For $1.1\,\mathrm{eV} < E_{KER} < 1.5\,\mathrm{eV}$ (fig. 6.6 (f)), the additional rotational energy brought into the system by the ion is not yet significant. But, since the E_{KER} exceeds $E_{\mathrm{OD,D,D}}$ by a small amount, the total energy is too high for producing a stable water molecule in the channel D_2O + D. In cases when the OD subsystem or angular degrees of freedom are vibrationally excited, the interaction potentials also do not allow a dissociation into OD + D + D, but only the formation of a temporarily bound D_2O^*. At this, the highly excited water D_2O^* above the dissociation limit can undergo a further decay into OD + D via IVR.

At higher energy, corresponding to fig. 6.6 (g) for $E_{KER} > 1.5\,\mathrm{eV}$, the excitation energy of the initial system may help this second dissociation process: the internal excitation of the ion is not essential for a sequential decay of this type to occur, but it increases the probability for such a dissociation. The observation though, that the dynamics in the two-step process seem to become inverted with increasing energy, is not explainable in this picture. Better statistics of the experimental data would clarify the findings and further, more detailed, theoretical input considering more degrees of freedom in the calculations would help to get an even better understanding of the dissociation mechanism of D_3O^+ following collisions with near-zero energetic electrons.

Chapter 7

Conclusions

In the presented thesis the fragmentation of the multi-electron molecular ions HF^+, DF^+ and D_3O^+ was investigated in slow electron collisions leading to dissociative recombination (DR). It has been shown that the reaction mechanisms and possible dissociation pathways can be deduced from observation of the DR fragmentation dynamics. In addition, for the two hydrogen fluorine isotopes it was possible to derive molecular constants from precision measurements of the kinetic energy released in the recombination process.

The DR process of the two isotopes HF^+ and DF^+ has been studied with optimal control of the accessible experimental parameters. Due to the unique structure of HF^+ leading to kinetic energy releases in the meV range for near-zero collision energies, a rotationally and fine-structure resolved momentum spectrum could be measured by fragment imaging of the reaction products. Acquiring such a detailed spectrum from storage rings DR measurements has not been possible with any other system. Due to the small experimental uncertainty, however, the dissociation energy could be deduced with sub-meV precision. The same was possible for the deuterium fluoride, even though the number of DR events leading to the final atomic state of interest in the detected momentum spectrum was reduced due to a lower zero-point energy of DF^+ compared to HF^+. The assumed rotational levels, which were calculated from molecular constants derived from those of HF^+, did model the kinetic-energy-release spectrum perfectly. The phenomenon of Born-Oppenheimer breakdown in isotopes could be investigated by comparing their classical bond dissociation energies. The difference in the measured dissociation energies revealed a dis-

crepancy from the Born-Oppenheimer approximated difference in zero-point energy in the electronic ground state towards a slightly larger spacing, which is in agreement with the effective potential energy for isotopes when non-Born-Oppenheimer effects are taken into account.

Even though merged-beam experiments in combination with neutral fragment imaging is usually not dedicated to measure such effects, a clear advantage of this method is that systematical errors chancel out to a large extent when subtracting the two dissociation energies. However, the uncertainty of this result could be improved significantly by the availability of DF^+ molecular constants obtained by optical spectroscopy. As all of these results rely on the small kinetic energy released in the dedicated DR channel of HF^+ and DF^+, this experiment most probably cannot be repeated for other molecules with this precision.

The DR of the astrophysically relevant ion D_3O^+ was studied by employing two different detectors that yield partly complementary information. Due to the mass sensitivity of the EMU detector, the transversal kinetic energy release distribution could be measured for the different dissociation channels, yielding information on the internal state of the products as well as the parent ion. In particular, the water molecules produced in the two-body channel were found to carry an internal excitation of more than 3 eV in 90 % of the recombination events. These findings, in combination with a full 3D fragmentation geometry distribution of the three-body channel OD + D + D obtained from the multi-hit optical gating detector, allowed the deduction of possible dissociation pathways. For case of high kinetic energy releases, a strongly asymmetric energy partitioning among the deuterium products suggested a sequential decay via an excited water molecule D_2O^*. This was supported by additional input from theory, providing adiabatic potential energy surfaces of the ground and several excited states of the neutral D_3O. These potential energy surfaces allowed the proposal of a qualitative mechanism that describes the interrelated dissociation into $D_2O + D$ and $OD + D + D$. Furthermore, in contrast to the inital assumptions, theory suggests that the internal excitation of the ion is not essential for the sequential decay to occur, but rather increases the probability of such a dissociation due to the formation of Feshbach resonances with picosecond lifetimes, before they undergo intramolecular vibrational redistribution and dissociate.

For a verification of this proposed mechanism, more control over the ion state is

essential. Repeating the measurement with cold D_3O^+, for which only few rotational states are populated, could provide valuable insights. Such a measurement would be possible using the *Cryogenic Storage Ring* (CSR), which is currently under construction at the Max-Planck-Intitut für Kernphysik. This electrostatic ring is designed to store ions at ambient temperatures below 10 K in order to avoid any heating of the ions by black-body radiation. Equipped with a dedicated cold source producing ions in the vibrational ground state with only very few rotational states populated, investigations of the DR of D_3O^+ in the CSR could reveal whether or not the two-step process occurs independently of the initial parent ion excitation. Due to the electrostatic ion-optics, the ions, unfortunately, have to be stored at much slower velocities in the CSR. This rules out the use of surface barrier detectors, since the fragment energy is too small to penetrate the dead layer on the surface of these detectors. The EMU concept of mass identification, therefore, cannot be realized. In contrast, MCP-based detectors such as the multi-hit optical gating detector or MCP-delay-line detectors will profit from the lower ion beam energy. The slow beam velocity leads to larger arrival-time differences between the individual fragments at the detector. Hence, the time resolution would improve significantly and, in case of the optical gating detector, partly compensate the observed negative effect of the different fragment masses on the time resolution.

Appendix A

A.1 Hund's Coupling Cases

In 1926, Hund [Hun26] introduced the concept of classifying the spectral terms of diatomic molecules by a number of coupling cases for the different angular momenta. Depending on whether the coupling between the electronic spin $\vec{S}$ and the molecular axis is very weak or very strong, the states of light diatomic molecules can be specified as one of the two extreme cases:

Hund's coupling case (a) In case of a strong interaction between $\vec{S}$ and the projection of the total orbital electronic angular momentum $\vec{L}$ onto the molecular axis, Λ, the spin is tightly coupled to the molecular axis. Consequently, the projection Ω of the total electronic angular momentum onto the axis of symmetry is the sum of Λ and the quantization of the spin projection, Σ, i.e. $\Omega\,\vec{e}_z = \Lambda\,\vec{e}_z + \Sigma\,\vec{e}_z$. For a rotating molecule, Ω and the angular momentum of nuclear rotation, $\vec{R}$, form the resultant total angular momentum $\vec{J}$ (fig. A.1 (a)).

Hund's coupling case (b) The opposite case is realized, when the forces ex-

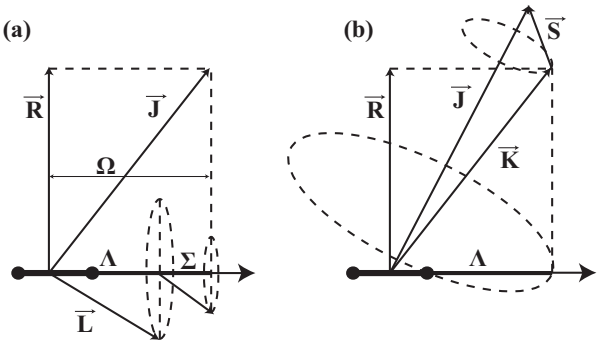

Figure A.1 Vector diagrams for Hund's coupling cases (a) and (b).

erted on $\vec{S}$ by the molecular rotation are large compared to the interaction between the spin and Λ. Thus, the spin is only loosely coupled to the rest of the molecule, resulting in a precession around $\vec{K}$, the resultant angular momentum of orbital momentum $\Lambda\,\vec{e}_z$ and nuclear rotation momentum $\vec{R}$, i.e. $\vec{J} = \vec{K} + \vec{S}$ with $\vec{K} = \Lambda\,\vec{e}_z + \vec{R}$ (fig. A.1 (b)). Diatomic molecular ions consisting of at least one L-shell atom have a considerable number of electrons producing states that often can be described by a intermediate case between (a) and (b).

A.2 Estimation of Vibrational and Rotational Lifetimes of D_3O^+

Assuming the D_3O^+ ion to be in its electronic ground state and neglecting any impact induced depletion, the average lifetime of an initial rovibrational state i is given by the reciprocal sum of *Einstein coefficients* for spontaneous emission, A_{fi}, that indicate the transition probabilities into final states f of lower energy:

$$\tau_i = \frac{1}{\sum\limits_f A_{fi}}. \tag{A.1}$$

An expression for A_{fi} in the dipole approximation can be found e. g. in [Dem03]:

$$A_{fi} = \frac{4\omega_{fi}^3}{3\hbar c^3}\frac{1}{4\pi\epsilon_0}|\hat{\mu}_{fi}|^2, \tag{A.2}$$

where ω_{fi} terms the transition frequency and $|\hat{\mu}_{fi}|^2$ represents the square of the dipole moment matrix element for the transition, summed over the three perpendicular directions in space. In the following the transition dipole moment $\hat{\mu}_{fi} = \langle f|\hat{\mu}|i\rangle$ is calculated separately for purely vibrational and rotational transitions.

Vibrational lifetimes of D_3O^+ In the Born-Oppenheimer approximation [Bor27] the dependence of $\hat{\mu}$ on the nuclear coordinates can be approximated by the first term of its Taylor expansion about the normal coordinate Q_k^0, so the total electric-dipole transition matrix element becomes [Wil55]

$$\langle v_f|\hat{\mu}|v_i\rangle = \sum_{k=1}^{3N-6}\left(\frac{\delta\hat{\mu}}{\delta Q_k}\right)_0\langle v_f|Q_k - Q_k^0|v_i\rangle. \tag{A.3}$$

Table A.1 Einstein coefficients and lifetimes for $\Delta v = -1$ transitions into the fundamentals for each normal mode $v^{(n)}$ $(n = 1, 2, 3, 4)$. The vibrational frequencies ω_{fi} and infrared intensities are taken from [Col83].

Transition	ω_{fi} [cm^{-1}]	Intensities [$D^2/\mathring{A}$ amu]	A_{fi} [Hz]	τ [s]
$v_{i=1}^{(1)} \rightarrow v_{f=0}^{(1)}$	2722	0.6	23.46	0.042
$v_{i=1}^{(2)} \rightarrow v_{f=0}^{(2)}$	617	6.6	13.26	0.075
$v_{i=1}^{(3)} \rightarrow v_{f=0}^{(3)}$	2907	7.0	624.32	0.0016
$v_{i=1}^{(4)} \rightarrow v_{f=0}^{(4)}$	1304	1.3	23.2	0.043

The selection rule $\Delta v = \pm 1$ for electric-dipole transitions constrains the final state to $f = i - 1$. Expressing the position operator $\hat{x}$ by means of creation and annihilation operators, i.e. $\hat{x} = \sqrt{\frac{\hbar}{2\,m\,\omega_{fi}}}\langle v-1|\hat{a}+\hat{a}^+|v\rangle$, and using the relation $\hat{a}|v\rangle = \sqrt{v}|v-1\rangle$ yields

$$A_{i-1,i} = \frac{4\omega_{fi}^3}{3\hbar c^3}\frac{1}{4\pi\epsilon_0}\frac{v\,\hbar}{2\,m\,\omega_{i-1,i}}\left(\frac{\delta\mu}{\delta x}\right)^2. \tag{A.4}$$

In first approximation, the degeneracy of v_3 and v_4 doubles the dipole derivative in these eigenmodes.

Einstein coefficients and lifetimes of the $i = 1$ normal modes are given in tab. A.1. Even though the ions are likely to be produced in the ion source in a vibrational state $i > 1$, the lifetimes calculated for the $i = 1$ state indicate an efficient radiative cooling. Thus, a storage time of 9 s before data acquisition justifies the assumption of vibrationally cooled ions in the ring. In addition, this lifetime approximation only considers radiative cooling – superelastic collisions [Sha09] with the electrons might reduce the lifetime even further.

Rotational lifetimes of D_3O^+ For a nonplanar symmetric top molecule, as the D_3O^+ in its ground state, the selection rules for purely rotational dipole radiation are (eq. (3.39) in [Tow55])

$$\Delta J = 0, \pm 1 \qquad \Delta K = 0 \qquad + \rightarrow -, \tag{A.5}$$

where + and − specify the inversion level and K is the component of the angular momentum J along the axis going through O and midway between the three D

atoms. Similar to the atomic quantum number m_z, K may have a number of values but can never be larger than J, it is $K = J, J-1, ..., -J$. From eq. (A.5) a long lifetime of the lower rotational states can be deduced: since $\Delta K = 0$ for each transition the molecules will 'get stuck' at $K = J$. These states can only deexcite via non-dipole transitions which have much smaller intensities resulting in long lifetimes of the corresponding states.

Sergei Yurchenko and Per Jensen[1] confirmed the existence of long-lived states by simulating the line strengths of transitions involving term values of less than $1000\,\mathrm{cm}^{-1}$ obtained from *ab initio* potential energy and dipole moment surface calculations. These line strengths were used to generate the Einstein coefficients for spontaneous emission transitions into lower lying energy levels. Eq. (A.1) then yielded the lifetime of the initial level. They found the $J = K$ levels to have lifetimes between $10^2\,\mathrm{s}$ and even $10^{24}\,\mathrm{s}$ – in any case much longer than the storage time in the ring.

A.3 Rotational barrier estimation of D_3O

In [Bul97], the rotational Hamiltonian for a dipolar, prolate symmetric top molecule is given as

$$\mathcal{H} = C\left(\hat{J}^2 + \left(\frac{B_x}{B_z} - 1\right) J_z^2\right), \tag{A.6}$$

with B_a and B_c (and B_b) being the rotational constants regarding a rotation around the symmetry axes a and c (and b) for a given geometry of the molecule. For a prolate, symmetric top molecule these axes are defined by the moments of inertia I_x, I_y and I_z, with $I_x < I_y = I_z$. The total angular momentum operator $\hat{J}$ and its maximum projection J_z are estimated assuming an occupation of the rotational states according to a Boltzmann distribution for $T = 3500\,\mathrm{K}$. For each point on the two-dimensional potential energy surface the corresponding configuration yields the moments of inertia, from which the rotational constants can be calculated via

$$B_x = \frac{\hbar}{4\pi I_x}, \qquad B_y = \frac{\hbar}{4\pi I_y}, \qquad B_z = \frac{\hbar}{4\pi I_z}. \tag{A.7}$$

[1] University of Wuppertal, private communications

As expected, the additional energy, brought into the system due to rotations, is almost 400 meV at equilibrium geometry. At $r_1 = r_3 \approx 2.3\,\text{Å}$, where the transition into the D_3O ground state is assumed to occur, the additional energy due to rotations of the molecule has decreased to less than 40 meV.

Bibliography

[All04] M. D. Allen, K. M. Evenson, and J. M. Brown. Part of the far-infrared laser magnetic resonance spectrum of the HF^+ free radical. *J. Mol. Spectrosc.*, **227**(1), (2004) 13.

[Ami96] Z. Amitay, D. Zajfman, P. Forck, U. Hechtfischer, B. Seidel, M. Grieser, D. Habs, R. Repnow *et al.* Dissociative recombination of CH^+: Cross section and final states. *Phys. Rev. A*, **54**(5), (1996) 4032.

[Ami98] Z. Amitay, A. Baer, M. Dahan, L. Knoll, M. Lange, J. Levin, I. F. Schneider, D. Schwalm *et al.* Dissociative recombination of HD^+ in selected vibrational quantum states. *Science*, **281**(5373), (1998) 75.

[And96] L. H. Andersen, O. Heber, D. Kella, H. B. Pedersen, L. Vejby-Christensen, and D. Zajfman. Production of water molecules from dissociative recombination of H_3O^+ with electrons. *Phys. Rev. Lett.*, **77**(24), (1996) 4891.

[Bar68] J. N. Bardsley. The theory of dissociative recombination. *J. Phys. B: At. Mol. Phys.*, **1**(3), (1968) 365.

[Bat50] D. R. Bates. Dissociative recombination. *Phys. Rev.*, **78**(4), (1950) 492.

[Bat91] D. R. Bates. Dissociative recombination of polyatomic ions. *J. Phys. B: At. Mol. Opt. Phys.*, **24**(14), (1991) 3267.

[Ber71] J. Berkowitz, W. A. Chupka, P. M. Guyon, J. H. Holloway, and R. Spohr. Photoionization Mass Spectroscopic Study of F_2, HF, and DF^*. *J. Chem. Phys.*, **54**(12), (1971) 5165.

[Ber01] I. B. Bersuker. Modern aspects of the Jahn-Teller effect theory and applications to molecular problems. *Chem. Rev.*, **101**(4), (2001) 1067.

[Beu00] M. Beutelspacher, M. Grieser, D. Schwalm, and A. Wolf. Longitudinal and transverse electron cooling experiments at the Heidelberg heavy ion storage ring TSR. *Nucl. Instrum. Methods Phys. Res., Sect. A*, **441**(1-2), (2000) 110.

[Blo89] C. Blondel, P. Cacciani, C. Delsart, and R. Trainham. High-resolution determination of the electron affinity of fluorine and bromine using crossed ion and laser beams. *Phys. Rev. A*, **40**(7), (1989) 3698.

[Bor27] M. Born and R. Oppenheimer. Quantum theory of molecules. *Ann. Phys.*, **84**(20), (1927) 0457.

[Bot83] P. Botschwina, P. Rosmus, and E. A. Reinsch. Spectroscopic properties of the hydroxonium ion calculated from SCEP CEPA wavefunctions. *Chem. Phys. Lett.*, **102**(4), (1983) 299.

[Boy03] T. J. M. Boyd and J. J. Sanderson. *The Physics of Plasmas*. Cambridge, 2003.

[Bra98] C. Brandau, F. Bosch, G. Dunn, B. Franzke, A. Hoffknecht, C. Kozhuharov, P. H. Mokler, A. Müller *et al.* Dielectronic recombination of lithium-like gold: Towards QED tests. *Hyperfine Interact.*, **114**(1-4), (1998) 45.

[Bro00] A. Brown and G. G. Balint-Kurti. Spin-orbit branching in the photodissociation of HF and DF. I. A time-dependent wave packet study for excitation from v=0. *J. Chem. Phys.*, **113**(5), (2000) 1870.

[Bru70] C. R. Brundle. Ionization and Dissociation Energies of HF and DF and their Bearing on $D_0^\circ(F_2)$. *Chem. Phys. Lett.*, **7**(3), (1970) 317.

[Buh06] H. Buhr. *Electron collisions and internal excitation in stored molecular ion beams*. Ph.D. thesis, Ruperto-Carola-University of Heidelberg, Germany (2006).

[Buh10a] H. Buhr, M. B. Mendes, O. Novotný, D. Schwalm, J. Stützel, M. H. Berg, D. Bing, O. Heber *et al.* Energy-sensitive imaging detector applied to the dissociative recombination of D_2H^+. *Phys. Rev. A*, **81**(6), (2010) 062702.

[Buh10b] H. Buhr, J. Stützel, M. B. Mendes, O. Novotný, D. Schwalm, M. Berg, D. Bing, M. Grieser *et al.* Hot Water Molecules from Dissociative Recombination of D_3O^+ with Cold Electrons. *Phys. Rev. Lett.*, **105**(10), (2010) 103202.

[Bul97] J. Bulthuis, J. Moller, and H. J. Loesch. Brute force orientation of asymmetric top molecules. *J. Phys. Chem. A*, **101**(41), (1997) 7684.

[But96] C. J. Butler and A. N. Hayhurst. Kinetics of dissociative recombination of H_3O^+ ions with free electrons in premixed flames. *J. Chem. Soc. Faraday T.*, **92**(5), (1996) 707.

[Car81] A. Carrington, J. Buttershaw, R. A. Kennedy, and T. P. Softley. Observation of bound to quasibound vibration-rotation transitions in the HeH^+ ion. *Mol. Phys.*, **44**(5), (1981) 1233.

[CER] CERN. *http://www.root.cern.ch.*

[Col83] M. E. Colvin, G. P. Raine, H. F. Schaefer, and M. Dupius. Infrared intensities of H_3O^+, H_2DO^+, HD_2O^+, and D_3O^+. *J. Chem. Phys.*, **79**(3), (1983) 1551.

[Cot73] R. J. Cotter and W. S. Koski. Reaction of D_3O^+ with D_2: Proton affinity of water. *J. Chem. Phys.*, **59**(2), (1973) 784.

[Dal53] R. H. Dalitz. On the Analysis of $\tau-$Meson Data and the Nature of the $\tau-$Meson. *Philos. Mag.*, **44**(357), (1953) 1068.

[Dan94] H. Danared, G. Andler, L. Bagge, C. J. Herrlander, J. Hilke, J. Jeansson, A. Kallberg, A. Nilsson *et al.* Electron Colling with an Ultracold Electron Beam. *Phys. Rev. Lett.*, **72**(24), (1994) 3775.

[Dec96] B. Deconihout, P. Gerard, M. Bouet, and A. Bostel. Improvement of the detection efficiency of channel plate electron multiplier for atom probe application. *Appl. Surf. Sci.*, **94-5**, (1996) 422.

[Dem03] W. Demtröder. *Molekülphysik.* Oldenbourg Wissenschaftsverlag, 2003.

[Dik88] N. S. Dikansky, V. I. Kudelainen, V. I. Lebedev, V. A. Meshkov, V. V. Parkhomchuk, A. A. Sery, A. N. Skrinsky, and B. N. Sukhina. Ultimate possibilities of electron cooling. *preprint.*

[Dju01] N. Djuric, G. H. Dunn, A. A. Khalili, A. M. Derkatch, A. Neau, S. Rosén, W. Shi, L. Vikor *et al.* Resonant ion-pair formation and dissociative recombination in electron collisions with ground-state HF^+ ions. *Phys. Rev. A*, **64**(2), (2001) 022713.

[Eyl93] E. E. Eyler and N. Melikechi. Near-threshold continuum structure and the dissociation energies of H_2, HD, and D_2. *Phys. Rev. A*, **48**(1), (1993) R18.

[Fis09] D. Fischer, M. Schulz, K. Schneider, M. F. Ciappina, T. Kirchner, A. Kelkar, S. Hagman, M. Grieser *et al.* Systematic analysis of double-ionization dynamics based on four-body Dalitz plots. *Phys. Rev. A*, **80**(6), (2009) 062703.

[FM06] A. I. Florescu-Mitchell and J. B. A. Mitchell. Dissociative recombination. *Phys. Rep.*, **430**(5-6), (2006) 277.

[Fro67] D. Frost, C. A. McDowell, and D. Vroom. Photoelectron Spectra of the Halogens and the Hydrogen Halides. *J. Chem. Phys.*, **46**(11), (1967) 4255.

[Gew75] S. Gewurtz, H. Lew, and P. Flainek. The Electronic Spectrum of HF^+. *Can. J. Phys.*, **53**(11), (1975) 1097.

[Gol07] H. Goldschmidt and O. Udby. Ester formation. *Z. Phys. Chem.-Stoechiom.*, **60**(6), (1907) 728.

[Gou97] T. Gougousi, R. Johnsen, and M. F. Golde. Yield determination of OH(v=0,1) radicals produced by the electron-ion recombination of H_3O^+ ions. *J. Chem. Phys.*, **107**(7), (1997) 2430.

[Gre10] M. Grechko, P. Maksyutenko, T. R. Rizzo, and O. V. Boyarkin. Communication: Feshbach resonances in the water molecule revealed by state-selective spectroscopy. *J. Chem. Phys.*, **133**(8), (2010) 081103.

[Gri93] M. Grieser, H. Deitinghoff, D. Habs, R. von Hahn, E. Jaeschke, C. Kleffner, V. Kossler, S. Papureanu *et al.* Upgrading of the Heidelberg accelerator facility with a new high current injector. *Nucl. Instrum. Methods Phys. Res., Sect. A*, **328**(1-2), (1993) 160.

[Guy76] P. M. Guyon, R. Spohr, W. A. Chupka, and J. Berkowitz. Threshold photoelectron spectra of HF, DF, and F_2. *J. Chem. Phys.*, **65**(5), (1976) 1650.

[Hab89] D. Habs, W. Baumann, J. Berger, P. Blatt, A. Faulstich, P. Krause, G. Kilgus, R. Neumann *et al.* First Experiments with the Heidelberg Test Storage Ring TSR. *Nucl. Instrum. Methods Phys. Res., Sect. B*, **43**(3), (1989) 390.

[Har01] S. A. Harich, X. F. Yang, D. W. H. Hwang, J. J. Lin, X. M. Yang, and R. N. Dixon. Photodissociation of D_2O at 121.6 nm: A state-to-state dynamical picture. *J. Chem. Phys.*, **114**(18), (2001) 7830.

[Her54] G. Herzberg. *Molecular Spectra and Molecular Structure, I. Spectra of Diatomic Molecules.* Krieger Publishing Company, Malabar, Florida, 1954.

[Her78] E. Herbst. What are the products of polyatomic ion-electron dissociative recombination reactions? *Astrophys. J.*, **222**(2), (1978) 508.

[Her90] C. R. Herd, N. G. Adams, and D. Smith. OH production in the dissociative recombination of H_3O^+, HCO_2^+, and N_2OH^+: comparison with theory and interstellar implications. *Astrophys. J.*, **349**(1), (1990) 388.

[Her05] E. Herbst. Chemistry of star-forming regions. *J. Phys. Chem. A*, **109**(18), (2005) 4017.

[Her06] I. V. Hertel and W. Radloff. Ultrafast dynamics in isolated molecules and molecular clusters. *Rep. Prog. Phys.*, **69**(6), (2006) 1897.

[Hil28] E. Hill and J. H. V. Vleck. On the quantum mechanics of the rotational distortion of multiplets in molecular spectra. *Phys. Rev.*, **32**(2), (1928) 0250.

[Hör06] M. Hörndl, S. Yoshida, A. Wolf, G. Gwinner, M. Seliger, and J. Burgdörfer. Classical dynamics of enhanced low-energy electron-ion recombination in storage rings. *Phys. Rev. A*, **74**(5), (2006) 052712.

[Hos99] T. Hoshino and Y. Nishioka. Etching process of SiO_2 by HF molecules. *J. Chem. Phys.*, **111**(5), (1999) 2109.

[Hu06] Q. J. Hu and J. Hepburn. Energetics and dynamics of threshold photoion-pair formation in HF/DF. *J. Chem. Phys.*, **124**(7), (2006) 074311.

[Hun26] F. Hund. Concerning the importance of some appearances in the molecular spectra. *Z. Angew. Phys.*, **36**(9-10), (1926) 657.

[Jen00] M. J. Jensen, R. C. Bilodeau, C. P. Safvan, K. Seiersen, L. H. Andersen, H. B. Pedersen, and O. Heber. Dissociative recombination of H_3O^+, HD_2O^+, and D_3O^+. *Astrophys. J.*, **543**(2), (2000) 764.

[Kay06] M. Kayanuma, T. Taketsugu, and K. Ishii. Ab initio surface hopping simulation on dissociative recombination of H_3O^+. *Chem. Phys. Lett.*, **418**(4-6), (2006) 511.

[Kel87] R. Kelly. Atomic and ionic spectrum lines of hydrogen through krypton. *J. Phys. Chem. Ref. Data*, **16**.

[Ket99] A. E. Ketvirtis and J. Simons. Dissociative recombination of H_3O^+. *J. Phys. Chem. A*, **103**(33), (1999) 6552.

[Kle96] S. Klein, E. Kochanski, and A. Strich. Electric properties of the oxonium ion in its ground and two lowest excited states. *Chem. Phys. Lett.*, **260**(1-2), (1996) 34.

[Kne60] P. F. Knewstubb and T. M. Sugden. Mass-spectrometric studies of ionization in flames. I. The spectrometer and its application to ionization in hydrogen flames. *Proc. R. Soc. London, Ser. A*, **255**(1283), (1960) 520.

[Kok] V. Kokoouline. First principles theoretical framework to study dissociation recombination in highly-symmetric polyatomic molecular ions: Example of H_3O^+. *to be published.*

[Kok03] V. Kokoouline and C. H. Greene. Unified theoretical treatment of dissociative recombination of D_{3h} triatomic ions: Application to H_3^+ and D_3^+. *Phys. Rev. A*, **68**(1), (2003) 012703.

[Kra09] C. Krantz. *Intense Electron Beams from GaAs Photocathodes as a Tool for Molecular and Atomic Physics.* Ph.D. thesis, Ruperto-Carola-University of Heidelberg, Germany (2009).

[Kra10] C. Krantz, K. Blaum, Y. A. Litvinov, R. Repnow, and A. Wolf. Enhanced Schottky signals from electron-cooled, coasting beams in a heavy-ion storage ring. *submitted to Nucl. Instr. Methods Phys. Res., Sect. A.*

[Lam04] L. Lammich. *Fragmentation Studies with Stored Beams of Small Polyatomic Ions.* Ph.D. thesis, Ruperto-Carola-University of Heidelberg, Germany (2004).

[Lar97] M. Larsson. Dissociative recombination with ion storage rings. *Annu. Rev. Phys. Chem.*, **48**, (1997) 151.

[Lar08] M. Larsson and A. E. Orel. *Dissociative Recombination of Molecular Ions.* Cambridge University Press, 2008.

[LaV03] LaVision© GmbH, Anna-Vandenhoeck-Ring 19, D-37081 Göttingen, Germany. *PicoStar HR Manual* (2003).

[LaV04] LaVision© GmbH, Anna-Vandenhoeck-Ring 19, D-37081 Göttingen, Germany. *Time Resolved Event Detection Manual* (2004).

[Lem68a] H. J. Lempka, T. R. Passmore, and W. C. Price. The Photoelectron spectra and ionized states of the halogen acids. *Proc. R. Soc. London, Ser. A*, **304**(1476), (1968) 53.

[Lem68b] H. J. Lempka and W. C. Price. Ionization Energies of HF and DF. *J. Chem. Phys.*, **48**(4), (1968) 1875.

[Ler71] R. Leroy and R. B. Bernstein. Shape Resonances and Rotationally Predissociating Levels: The Atomic Collision Time-Delay Functions and Quasibound Level Properties of $H_2(X^1\Sigma_g^+)$. *J. Chem. Phys.*, **54**(12), (1971) 5114.

[Les07] M. Lestinsky. *High-Resolution Electron Collision Spectroscopy with Multicharged Ions in Merged Beams.* Ph.D. thesis, Ruperto-Carola-University of Heidelberg, Germany (2007).

[Les08] M. Lestinsky, E. Lindroth, D. A. Orlov, E. W. Schmidt, S. Schippers, S. Böhm, C. Brandau, F. Sprenger *et al.* Screened radiative corrections from hyperfine-split dielectronic resonances in lithiumlike scandium. *Phys. Rev. Lett.*, **100**(3), (2008) 033001.

[Luo99] M. Luo and M. Jungen. The H_3O Rydberg radical. *Chem. Phys.*, **241**(3), (1999) 297.

[Man94] A. Mank, D. Rodgers, and J. Hepburn. Threshold photoelectron spectroscopy of HF. *Chem. Phys. Lett.*, **219**(3-4), (1994) 169.

[Man09] J. E. Mann, Z. Xie, J. D. Savee, J. M. Bowman, and R. E. Continetti. Production of vibrationally excited H_2O from charge exchange of H_3O^+ with cesium. *J. Chem. Phys.*, **130**(4), (2009) 041102.

[Mau97] C. Maul and K. H. Gericke. Photo induced three body decay. *Int. Rev. Phys. Chem.*, **16**(1), (1997) 1.

[McC98] B. J. McCall, T. R. Geballe, K. H. Hinkle, and T. Oka. Detection of H_3^+ in the diffuse interstellar medium toward Cygnus OB2 No. 12. *Science*, **279**(5358), (1998) 1910.

[Men07] M. Mendes. *Hochauflösende dreidimensionale Fragementabbildung bei Speicherringexperimenten mit Molekülionen.* Master's thesis, Ruperto-Carola-University of Heidelberg, Germany (2007).

[Men10] M. Mendes. *Molecular fragmentation by recombination with cold electrons studied with a mass sensitive imaging detector*. Ph.D. thesis, Ruperto-Carola-University of Heidelberg, Germany (2010).

[Mes] Mesytec GmbH. *http://www.mesytec.de*.

[Mic] Micron Semiconductors Ltd. *http://www.micronsemiconductor.co.uk*.

[Mil88] T. J. Millar, D. J. Defrees, A. D. McClean, and E. Herbst. The sensitivity of gas-phase models of dense interstellar clouds to changes in dissociative recombination branching ratios. *Astron. Astrophys.*, **194**(1-2), (1988) 250.

[Mul83] P. M. Mul, J. W. McGowan, P. Defrance, and J. B. A. Mitchell. Merged electron-ion beam experiments: V. Dissociative recombination of OH^+, H_2O^+, H_3O^+ and D_3O^+. *J. Phys. B: At. Mol. Opt. Phys.*, **16**(16), (1983) 3099.

[Mül98] A. Müller, T. Bartsch, C. Brandau, A. Hoffknecht, H. Knopp, S. Schippers, O. Uwira, J. Linkemann *et al.* Recent dielectronic recombination experiments. *Hyperfine Interact.*, **114**(1-4), (1998) 229.

[Nak10] K. Nakamura and Particle Data Group. 2010 Review of Particle Physics. *J. Phys. G*, **37**, (2010) 075021.

[Neu95] D. A. Neufeld, S. Lepp, and G. J. Melnick. Thermal balance in dense molecular clouds: radiative cooling rates and emission-line luminosities. *Astrophys. J. Suppl. Ser.*, **100**(1), (1995) 132.

[Neu97] D. A. Neufeld, J. Zmuidzinas, P. Schilke, and T. G. Phillips. Discovery of interstellar hydrogen fluoride. *Astrophys. J.*, **488**(2), (1997) L141.

[Neu05] D. A. Neufeld, M. G. Wolfire, and P. Schilke. The chemistry of fluorine-bearing molecules in diffuse and dense interstellar gas clouds. *Astrophys. J.*, **628**(1), (2005) 260.

[Nev07] I. Nevo, S. Novotny, H. Buhr, V. Andrianarijaona, S. Altevogt, O. Heber, J. Hoffmann, H. Kreckel *et al.* Three-body kinematical correlation in the dissociative recombination of CH_2^+ by three-dimensional imaging. *Phys. Rev. A*, **76**(2), (2007) 022713.

[Nie00] M. Niering, R. Holzwarth, J. Reichert, P. Pokasov, T. Udem, M. Weitz, T. W. Hänsch, P. Lemonde *et al.* Measurement of the Hydrogen $1S$-$2S$ Transition Frequency by Phase Coherent Comparison with a Microwave Cesium Fountain Clock. *Phys. Rev. Lett.*, **84**(24), (2000) 5496.

[Nov05] S. Novotny. *Fast-beam molecular fragmentation imaging using a high-speed gated camera system.* Master's thesis, Ruperto-Carola-University of Heidelberg, Germany (2005).

[Nov08a] S. Novotny. *Fragmentation of molecular ions in slow electron collisions.* Ph.D. thesis, Ruperto-Carola-University of Heidelberg, Germany (2008).

[Nov08b] S. Novotny, H. Rubinstein, H. Buhr, O. Novotný, J. Hoffmann, M. B. Mendes, D. A. Orlov, C. Krantz *et al.* Anisotropy and molecular rotation in resonant low-energy dissociative recombination. *Phys. Rev. Lett.*, **100**(19), (2008) 193201.

[Nov10] O. Novotný, H. Buhr, J. Stützel, M. B. Mendes, M. H. Berg, D. Bing, M. Froese, M. Grieser *et al.* Fragmentation Channels in Dissociative Electron Recombination with Hydronium and Other Astrophysically Important Species. *J. Phys. Chem. A*, **114**(14), (2010) 4870.

[Orl04] D. A. Orlov, U. Weigel, D. Schwalm, A. S. Terekhov, and A. Wolf. Ultracold electron source with a GaAs-photocathode. *Nucl. Instrum. Methods Phys. Res., Sect. A*, **532**(1-2), (2004) 418.

[Orl09] D. A. Orlov, C. Krantz, A. Wolf, A. S. Jaroshevich, S. N. Kosolobov, H. E. Scheibler, and A. S. Terekhov. Long term operation of high quantum efficiency GaAs(Cs,O) photocathodes using multiple recleaning by atomic hydrogen. *J. Appl. Phys.*, **106**(5), (2009) 054907.

[Pah98] E. Pahl, H. D. Meyer, L. S. Cederbaum, and F. Tarantelli. Theory of wave packet dynamics: resonant Auger spectrum of HF. *J Electron. Spectrosc. Relat. Phenom.*, **93**(1-3), (1998) 17.

[Pas96] S. Pastuszka, U. Schramm, M. Grieser, C. Broude, R. Grimm, D. Habs, J. Kenntner, H. J. Miesner *et al.* Electron cooling and recombination experiments with an adiabatically expanded electron beam. *Nucl. Instrum. Methods Phys. Res., Sect. A*, **369**(1), (1996) 11.

[Pre92] W. H. Press, S. A. Taukolsky, W. T. Vetterling, and B. P. Flannery. *Numerical Recipes in Fortran 77.* Cambridge University Press, 1992.

[Ral10] Y. Ralchenko, A. Kramida, J. Reader, and NIST ASD Team (2010). *NIST Atomic Spectra Database (ver. 4.0.0), http://physics.nist.gov/asd.* National Institute of Standards and Technology, Gaithersburg, MD, USA, 2010.

[Roo08] J. B. Roos, A. Larson, and A. E. Orel. Dissociative recombination of HF^+. *Phys. Rev. A*, **78**(2), (2008) 022508.

[Roo09] J. B. Roos, A. E. Orel, and A. Larson. Resonant ion-pair formation in electron recombination with HF^+. *Phys. Rev. A*, **79**(6), (2009) 062510.

[Rub08] M. Rubio, L. Serrano-Andres, and M. Merchan. Excited states of the water molecule: Analysis of the valence and Rydberg character. *J. Chem. Phys.*, **128**(10), (2008) 104305.

[Sch26] E. Schrödinger. Quantisierung als Eigenwertproblem. *Ann. Phys.*, **286**(18), (1926) 109.

[Sea85] T. J. Sears, P. R. Bunker, P. B. Davies, S. A. Johnson, and V. Spriko. Diode laser absorption spectroscopy of D_3O^+: Determination of the equilibrium structure and potential function of the oxonium ion. *J. Chem. Phys.*, **83**(6), (1985) 2676.

[Sha09] D. Shafir, S. Novotny, H. Buhr, S. Altevogt, A. Faure, M. Grieser, A. Harvey, O. Heber *et al.* Rotational Cooling of HD^+ Molecular Ions by Superelastic Collisions with Electrons. *Phys. Rev. Lett.*, **102**(22), (2009) 223202.

[Sho] A. Shornikov, D. A. Orlov, C. Krantz, A. S. Jaroshevich, and A. Wolf. An intense ultra low energy photocathode electron beam. *to be published.*

[Spr03] F. Sprenger. *Production of cold electron beams for collision experiments with stored ions.* Ph.D. thesis, Ruperto-Carola-University of Heidelberg, Germany (2003).

[Spr04] F. Sprenger, M. Lestinsky, D. A. Orlov, D. Schwalm, and A. Wolf. The high-resolution electron-ion collision facility at TSR. *Nucl. Instrum. Methods Phys. Res., Sect. A*, **532**(1-2), (2004) 298.

[Ste90] M. Steck, G. Bisoffi, M. Blum, A. Friedrich, C. Geyer, M. Grieser, B. Holzer, E. Jaeschke *et al.* Electron cooling of heavy ions. *Nucl. Instrum. Methods Phys. Res., Sect. A*, **287**(1-2), (1990) 324.

[Str00] D. Strasser, X. Urbain, H. B. Pedersen, N. Altstein, O. Heber, R. Wester, K. G. Bhushan, and D. Zajfman. An innovative approach to multiparticle three-dimensional imaging. *Rev. Sci. Instrum.*, **71**(8), (2000) 3092.

[Tac00] H. Tachikawa. Full dimensional ab-initio dynamics calculations of electron capture processes by the H_3O^+ ion. *Phys. Chem. Chem. Phys.*, **2**(19), (2000) 4327.

[Tho08] R. D. Thomas. When electrons meet molecular ions and what happens next: Dissociative recombination from interstellar molecular clouds to internal combustion engines. *Mass. Spectrom. Rev.*, **27**(5), (2008) 485.

[Tow55] C. H. Townes and A. L. Schawlow. *Microwave Spectroscopy*. McGraw-Hill, 1955.

[Ull97] J. Ullrich, R. Moshammer, R. Dorner, O. Jagutzki, V. Mergel, H. Schmidt-Böcking, and L. Spielberger. Recoil-ion momentum spectroscopy. *J. Phys. B: At. Mol. Opt. Phys.*, **30**(13), (1997) 2917.

[VC97] L. Vejby-Christensen, L. H. Andersen, O. Heber, D. Kella, H. B. Pedersen, H. T. Schmidt, and D. Zajfman. Complete branching ratios for the dissociative recombination of H_2O^+, H_3O^+, and CH_3^+. *Astrophys. J.*, **483**(1), (1997) 531.

[Wat80] J. K. G. Watson. The Isotope Dependence of Diatomic Dunham Coefficients. *J. Mol. Spectrosc.*, **80**(2), (1980) 411.

[Wer84] H. J. Werner, P. Rosmus, W. Schatzl, and W. Meyer. PNO-CEPA and MCSCF-SCEP calculations of transition probabilities in OH, HF^+, and HCl^+. *J. Chem. Phys.*, **80**(2), (1984) 831.

[Wil55] E. B. Wilson, J. C. Decius, and P. C. Cross. *Molecular Vibrations*. Dover Publications, inc. New York, 1955.

[Wil96] T. L. Williams, N. G. Adams, L. M. Babcock, C. R. Herd, and M. Geoghegan. Production and loss of the water-related species H_3O^+, H_2O and OH in dense interstellar clouds. *Mon. Not. R. Astron. Soc.*, **282**(2), (1996) 413.

[Wit08] O. Witasse, T. Cravens, M. Mendillo, J. Moses, A. Kliore, A. F. Nagy, and T. Breus. Solar System Ionospheres. *Space Sci. Rev.*, **139**(1-4), (2008) 235.

[Wol00] A. Wolf, G. Gwinner, J. Linkemann, A. Saghiri, M. Schmitt, D. Schwalm, M. Grieser, M. Beutelspacher *et al.* Recombination in electron coolers. *Nucl. Instrum. Methods Phys. Res., Sect. A*, **441**(1-2), (2000) 183.

[Woo86] A. Wootten, F. Boulanger, M. Bogey, F. Combes, P. J. Encrenaz, M. Gerin, and L. Ziurys. A search for interstellar H_3O^+. *Astron. Astrophys.*, **166**(1-2), (1986) L15.

[Woo91] A. Wootten, J. G. Mangum, B. E. Turner, M. Bogey, F. Boulanger, F. Combes, P. J. Encrenaz, and M. Gerin. Detection of interstellar H_3O^+: a confirming line. *Astrophys. J.*, **380**(2), (1991) L79.

[Yen95] A. J. Yencha, A. Hopkirk, J. R. Grover, B. M. Cheng, H. Lefebvrebrion, and F. Keller. Ion-pair formation in the photodissociation of HF and DF. *J. Chem. Phys.*, **103**(8), (1995) 2882.

[Yen99] A. J. Yencha, A. J. Cormack, R. J. Donovan, A. Hopkirk, and G. C. King. Threshold photoelectron spectroscopy of HF and DF in the outer valence ionization region. *J. Phys. B: At. Mol. Opt. Phys.*, **32**(11), (1999) 2539.

[Zaj03a] D. Zajfman, S. Krohn, M. Lange, H. Kreckel, L. Lammich, D. Strasser, D. Schwalm, X. Urbain, and A. Wolf. Physics with molecular ions in storage rings. *Nucl. Instrum. Methods Phys. Res., Sect. B*, **205**, (2003) 360.

[Zaj03b] D. Zajfman, D. Schwalm, and A. Wolf. Multiparticle imaging of fast molecular ion beams. In J. Ullrich and V. Shevelko (editors), *Many-Particle Quantum Dynamics in Atomic and Molecular Fragmentation*. Springer, 2003.

[Zha09a] V. Zhaunerchyk, W. D. Geppert, S. Rosén, E. Vigren, M. Hamberg, M. Kamińska, I. Kashperka, M. af Ugglas *et al.* Investigation into the vibrational yield of OH products in the OH + H + H channel arising from the dissociative recombination of H_3O^+. *J. Chem. Phys.*, **130**(21), (2009) 214302.

[Zha09b] V. Zhaunerchyk, M. Kamińska, E. Vigren, M. Hamberg, W. D. Geppert, M. Larsson, R. D. Thomas, and J. Semaniak. Sequential formation of the $CH_3 + H + H$ channel in the dissociative recombination of CH_5^+. *Phys. Rev. A*, **79**(3), (2009) 030701.

[Zon99] W. Zong, G. H. Dunn, N. Djuric, M. Larsson, C. H. Greene, A. A. Khalili, A. Neau, A. M. Derkatch *et al.* Resonant ion pair formation in electron collisions with ground state molecular ions. *Phys. Rev. Lett.*, **83**(5), (1999) 951.

Danksagung

Abschießend möchte ich mich bei all jenen bedanken, die auf vielfältige Weise zum Gelingen dieser Arbeit beigetragen haben, ein besonderer Dank gilt

Andreas Wolf für die freundliche Aufnahme in seine Arbeitsgruppe und die sehr gute Betreuung meiner Arbeit. Sein physikalischer Ideenreichtum und seine intensive Unterstützung beim Vollenden dieser Arbeit tragen großen Anteil an den hier präsentierten Ergebnissen.

Selim Jochim für manch hilfreichen Blick von außen und seine Bereitschaft, das Zweitgutachen dieser Arbeit zu übernehmen.

Dirk Schwalm für seine Ratschläge und hilfreichen Diskussionen, aus denen immer wieder interessante Ideen hervorgingen.

Henrik Buhr, Oldrich Novotný und Steffen Novotny, von denen ich viel gelernt habe und ohne die die Durchführung der Experimente mit den 'BAMBI-Detektoren' nicht denkbar gewesen wäre.

Claude Krantz für seine Unterstützung in vielerlei Hinsicht, von seinem unermüdlichen Einsatz am Elektronen-Target während der Strahlzeiten über sein stetes offenes Ohr für jegliche Art von Frage bis hin zum gründlichen Korrekturlesen dieser Arbeit.

Annemieke Petrignani für ihre Unterstützung zu jeder Zeit, die zu hilfreichen Diskussionen führte und half, nicht den Blick für das Ganze zu verlieren.

Ann Orel für die wertvolle Zusammenarbeit bei den in Abschnitt 6.4 molekültheoretischen Rechnungen und den vielen damit verbundenen fruchtbaren Diskussionen.

Manfred Grieser und Kurt Horn, ohne deren steten Einsatz keines der Experimente am TSR möglich gewesen wäre, sowie Roland Repnow, Manfred König und alle

anderen hier nicht namentlich erwähnten Operateure, die den Betrieb der Beschleunigeranlagen durch fachkundige Steuerung und Wartung rund um die Uhr sicherstellten.

Herrn Hahn und seinen Mitarbeiter für die Hilfsbereitschaft beim Anfertigen so manch ausgefallener Wünsche, insbesondere Herrn Hallatschek für die Wartung und Instandhaltung der Kryopumpen in der BAMBI. Auch Oliver Koschorreck gebührt besonderer Dank für seine Hilfe bei Elektronikproblemen am 3D imaging detector.

Gernot Vogt für die Beschaffung so manch ausgefallener Publikation.

Max Berg für die angenehme Büroatmosphäre und die hilfreichen Diskussionen insbesondere in der gemeinsamen 'heißen' Phase.

allen übrigen ehemaligen und noch aktiven Mitgliedern der Molekülphysik Gruppe Dennis Bing, Christian Domesle, Mike Froese, Florian Grussie, Jens Hoffmann, Brandon Jordan-Thaden, Michael Lestinsky, Mario Mendes, Sebastian Menk, Christian Nordhorn, Andrey Shornikov für die angenehme Arbeitsatmosphäre, den Gesprächen am Kaffeetisch und das gemeinsame Laufen im Wald.

nicht zuletzt meinen Eltern, meinen Schwestern und JP für den nötigen Rückhalt und ihre uneingeschränkte Unterstützung in den vergangenen Jahren.